Investigation of Blast–related Fluid Cavitation using a Novel Polymeric Hopkinson Bar–Confinement Chamber Apparatus

by

Michael Christian Bustamante

A thesis
presented to the University of Waterloo
in fulfillment of the
thesis requirement for the degree of
Master of Applied Science
in
Mechanical and Mechatronics Engineering

Waterloo, Ontario, Canada, 2017

Author's Declaration

I hereby declare that I am the sole author of this thesis. This is a true copy of the thesis, including any required final revisions, as accepted by my examiners.

I understand that my thesis may be made electronically available to the public.

Abstract

Mild Traumatic Brain Injury (mTBI) associated with blast exposure has become an increasing issue in military conflicts, with the most common exposure being improvised explosive devices. Exposure to blast accounted for 81% of all casualties reported for Operation Enduring Freedom and Operation Iraqi Freedom combined. It has been identified as the 'signature injury' of the military conflicts in Iraq and Afghanistan, and has been reported to be strongly associated with higher rates of Post–Traumatic Stress Disorder (PTSD), depression, and physical health problems than with other injuries [1].

An observation common to most head blast exposure studies is the negative intracranial pressure occurring at the opposite site of initial blast wave transmission. This observation resulted in the hypothesis of intracranial cavitation of cerebrospinal fluid (CSF), due to the negative pressures generated, as a potential brain injury mechanism. The purpose of this work was to develop an apparatus that generates controlled localized cavitation with similar loading encountered in head blast exposure to measure the cavitation pressure thresholds of fluids. Existing dynamic methods of generating cavitation presented limited loading capabilities, boundaries, and were not suitable for testing of biological fluids, such as CSF.

Three iterations of the apparatus were developed, and the limitations identified were, potential cavitation nuclei and leakage at the seals and pressure gauge, variability in generated loading, and generation of diffuse cavitation. Due to the nuclei from the pressure gauge implementation, a validated numerical model of the apparatus was used to predict the negative fluid pressure in the chamber.

The final proposed design for the apparatus incorporated a novel closed cavitation chamber to generate localized cavitation resulting from a reflected compression pulse, which was generated by a spherical steel striker and Polymethyl methacrylate (PMMA) incident bar. Numerical models were developed and validated to model the PMMA incident bar with and without the PMMA chamber using 24 independent tests for strain and end velocity using

varying striker geometry (cross–correlation: 0.970–0.997). Additionally, the numerical model of the apparatus including the chamber was developed and validated with 27 independent tests for strain and chamber end surface velocity (cross–correlation: 0.921).

Cavitation tests on distilled water were performed and a 50% probability of cavitation was measured at a negative pressure of 3.39 MPa ±2%, comparable to values found in the literature. Analysis of the experimental and numerical result trends demonstrated comparable chamber strain (R^2: 0.875) and chamber end surface velocity (R^2: 0.992). The predicted fluid pressures from the model were verified with a first–order approximation showing good agreement (R^2: 0.892). This novel apparatus, incorporating a closed confinement chamber integrated with a polymeric SHPB apparatus, was able to create localized fluid cavitation using a reflected compression wave, with loading comparable to blast exposure. Future studies will investigate the measurement of CSF cavitation pressure and incorporation of the results in computational head-blast models.

Acknowledgements

I would first like to express my sincerest gratitude to my friends and family, without whom this thesis would have been completed much earlier.

I would like to thank my supervisor Dr. Duane Cronin for his guidance and encouragement throughout my entire graduate experience. Dr. Cronin helped keep me on the critical path of completing my journey and showing me the positive side of research regardless of the results.

I would also like to acknowledge the help and support of all of the laboratory technician in the MME Department.

Table of Contents

List of figures

List of tables

Introduction

Blast exposure has become more common in military conflicts due to the use of Improvised Explosive Devices (IEDs), with the most recent and notable being 'roadside bombs'. IEDs are improvised bombs that incorporate conventional high–energy explosives or homemade explosives. In the recent wars Operation Enduring Freedom (OEF) in Afghanistan from 2001 to 2017 and Operation Iraqi Freedom (OIF) in Iraq from 2003 to 2017, 40% and 37% of the coalition service member fatalities were the result of IED, respectively [2]. Blast exposure accounted for 81% of all casualties for both wars combined; greater than any previous war [3]. A non–fatal injury known as mild Traumatic Brain Injury (mTBI) has become an increasingly important issue for military conflicts, and was identified as the 'signature injury' of military conflicts in Iraq and Afghanistan [4, 5]. The United States Department of Defence defines mTBI as a head injury that results in the alteration or loss of consciousness (LOC). Some reports suggest that as much as 80% of all in–theatre–related traumatic brain injury cases were from blast exposure; with 75% of those being classified as mTBI [6, 7]. An estimation of 11–23% of returning US service members screened positive for mTBI [6]. Hoge et al. reported that mTBI (not limited to blast–related injury) from US infantrymen returning from OIF, especially those associated with LOC, was strongly associated with higher rates of Post–Traumatic Stress Disorder (PTSD), depression, and physical health problems than were with other injuries [1]. Additionally, some studies reported that mTBI increased the risk of PTSD [8–10].

Currently, mTBI is diagnosed through clinical assessments of functional deficits and neurological tests [11–13] (§ Chapter 1). Service members that are exposed to blast with non–physically–impairing injuries are evaluated to determine their ability to return to duty; however, these assessments and evaluations are subjective and based on approaches used for blunt impacts, which may not translate well to blast exposure and may not detect subtle effects that could limit performance during deployment [6, 9, 11]. Furthermore, mTBI from repeated blast exposure may increase the types and severity of symptoms likened to that seen in American football athletes with histories of multiple concussions; which is a form of mTBI [7]. Sports–related concussion is associated with translational acceleration and rotational velocity of the head, whereas blast–related

mTBI is associated with overpressure propagation through the brain; however, causes of blast–related mTBI is currently unknown [14, 15]. Injuries from blast exposure can be mitigated by the use of personal protective equipment (PPE), which are items worn or carried designed to mitigate trauma that can result from blast exposure. An example of PPE are helmets for military application, which have been assessed to reduce intracranial pressure (ICP) from blast [16–23]. However, some studies have reported the potential effect of a helmet amplifying loading to the head from pressure wave reflections occurring in the open space between the helmet and head [24, 25].

Several studies of pressure wave propagation in the head from an isolated blast wave have demonstrated the potential for injury. Some studies showed that the pressure wave propagation could lead to damage or change in function at the tissue or cellular levels [16, 26–30], with interfaces between structures having differing properties (density, elasticity) being particularly vulnerable [31]. Additionally, experimental and computational studies have also demonstrated that pressure wave propagation in the head produced a pressure gradient in the brain with positive pressures occurring at the site of transmission (coup) and negative pressure at the opposite site (contre–coup) [14, 22, 24, 32–39]. With the evidence of negative pressure, it was hypothesized that cavitation of cerebrospinal fluid (CSF) from blast exposure could be a possible injury mechanism leading to mTBI. Cavitation is the transient growth and violent collapse of vapour bubbles in a fluid that results in large localized pressures (§ Chapter 2).

An issue with examining cavitation *in situ* from blast exposure is the lack of transparency in cadaver and animal surrogate models. As an alternative, studies have used semi–transparent head models that mimic the human head, which allowed for high–speed imaging of cavitation occurrence [33, 34, 36, 40–42]. However, often the main purposes of such experiments were to study blast exposure pressure and strain effects in the head and the occurrence of cavitation was simply observed and not examined. Some experimental and computational studies have examined the effects of intracranial CSF cavitation on brain simulants with respect to localized pressures and strains [31, 34, 36, 40, 43–46]; however, the generation of cavitation in these tests were either seeded with a vapour bubble nuclei or assumed to generate at a pressure of –0.1 MPa. There is no consensus to the negative pressure threshold necessary for producing cavitation in CSF and there is a gap in the knowledge linking negative ICP observed in blast exposure and the generation of

CSF cavitation. To link this gap, an apparatus is required to dynamically load fluid in a manner similar to blast exposure, and generate observable localized fluid cavitation through a repeatable process. Using this apparatus, fluid pressures at which cavitation is generated can be measured. Alternative methods developed for generating cavitation exist, but limitations with their utilization were recognized such as loading, fluid volume, and fluid confinement (§ Chapter 3).

An apparatus was developed that could generate localized fluid cavitation through high–rate dynamic loading comparable to blast exposure. In parallel, a numerical model was developed that could reproduce experimental results obtained from the apparatus and predict fluid pressures that could not be directly measured (§ Chapter 4). The apparatus produced a compressive pulse by impact of a steel sphere striker onto an acrylic incident bar. This compressive pulse was propagated into an acrylic confinement chamber containing fluid. The chamber was designed with wall thickness dimensions comparable to cranial bones mimicking the conditions inside the head during blast exposure. Upon reaching the free–surface of the chamber exposed to air, the compressive pulse reflected in tension and transmitted back into the fluid producing negative pressure. With increasing compressive pulse magnitudes, it was demonstrated that non–cavitating and cavitating conditions could be observed. The negative fluid pressures corresponding to transition between non–cavitating and cavitating conditions were then used to determine the cavitation pressure threshold. Cavitation tests were performed on distilled water at 21 °C and 37 °C resulting in cavitation negative pressure thresholds of 3.39 MPa ±2% and 3.20 MPa ±5%, respectively (§ Chapter 5).

Chapter 1. Blast Exposure Background

1.1 Overview of Blast

An explosion is the rapid release of energy as a result of physical, nuclear, or chemical means. Physical explosions are caused by a rapid release of kinetic energy without the occurrence of nuclear or chemical reactions, such as the rupture of a pressure vessel, and nuclear explosions are caused by fusion or fission reactions that obey the mass–energy equivalence law [47, 48]. Chemical explosions are caused by a rapid oxidation reaction resulting in a rapid conversion of solid explosive to high temperature and high–pressure explosive gases, which contains most of the energy released by the explosion [16]. The rapid expansion of the explosive gases displaces the volume it occupies and produces a layer of compressed air known as a shock wave. As the gases expand from the source, its pressure falls to atmospheric pressures, which eventually cools and falls slightly below atmospheric pressures because of over–expansion. This over–expansion produces a reversal of flow towards the source due to the pressure differential between the atmosphere and explosive gases [49].

The pressure of the shock wave falls with increasing propagation distance similar to the explosive gases. A shock wave is defined as a discontinuity in pressure, temperature, and density across a finite thickness (in the order of 10^{-5} mm for air) that propagates through a medium faster than the acoustic speed of the medium [16, 50]. When energy in the form of a pressure wave is deposited into a medium, such as air, faster than it is dissipated outward from the source, the air within the wave is compressed resulting in increased temperature and acoustic speed. The energy from the source travels faster in the compressed air and accumulates at the front of the wave. If the energy at the front of the wave increases faster than it is dissipated to the ambient air, a shock wave is generated [51]. Shock waves can only occur in materials or gases that exhibit an increasing bulk modulus with increasing pressure resulting in the increased temperature and local acoustic speed necessary for generating shock waves [16]. Typically, the amount of energy released from explosions are often expressed in terms of Trinitrotoluene (TNT) mass that would result in the same amount of energy released [16].

The pressure wave resulting from an explosive blast is known as the blast wave and can be idealized using the Friedlander curve (Figure 1) [49]. A typical static pressure–time profile of a simple blast wave in free air consists of the supersonic shock wave (shock front) with a peak static pressure known as the peak overpressure, a decaying pressure to atmospheric pressure, and an underpressure region caused by the over–expansion of the explosive gases.

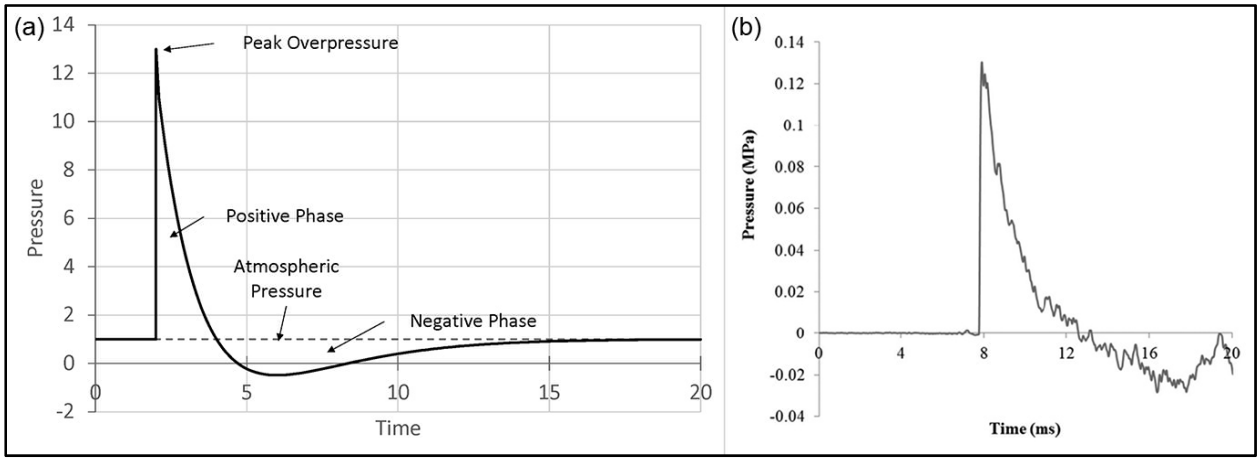

Figure 1. (a) Typical Friedlander curve used to represent a blast wave and its propagation; (b) Experimentally measured blast wave from a shock tube apparatus [35]

1.1.1 Blast Wave Interaction with Structures

Blast waves interact with structures by transporting energy from one area of the structure to another by way of pressure waves. When a blast wave in air meets a structure, a portion of the energy is transmitted into the structure and the balance of the energy is reflected (Figure 2). The reflected pressure wave constructively superimposes with the incident blast wave producing higher pressures at the air–structure interface. Superposition is when multiple waves overlay producing local amplitudes equal to the sum of the overlaid parts. Constructive superposition describes the greater local amplitude produced as a result of waves with similar senses (positive or negative), and destructive superposition describes the lesser local amplitude produced by waves with dissimilar senses [51]. The pressure wave transmitted into the structure propagates at a velocity equal to the acoustic speed of that structure. When the transmitted pressure wave propagates through a structure having different layers of density and/or acoustic speed, a reflected wave is produced at each interface. An example of blast wave interaction with the head can be observed

using a sagittal numerical model of the head developed by Singh et al. [39]. With frontal blast exposure, a pressure wave is transmitted into the head and a reflected wave is produced at the front of the face resulting in greater pressures than the incident blast wave (Figure 3). The different layers of the head (skin, flesh, bone, brain, etc.) results in the complex superposition of the propagating transmitted waves and reflections.

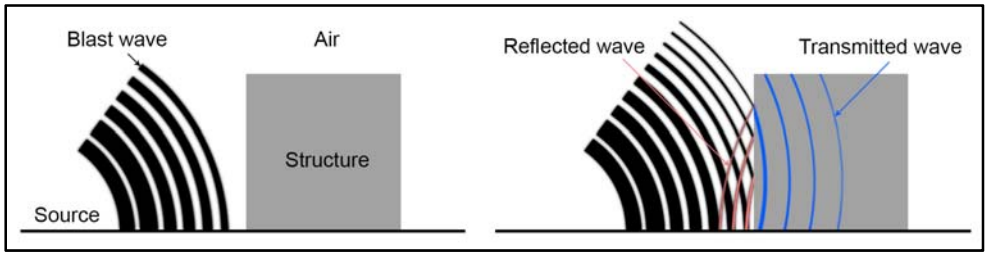

Figure 2. Reflected and transmitted waves from pressure wave structure interaction

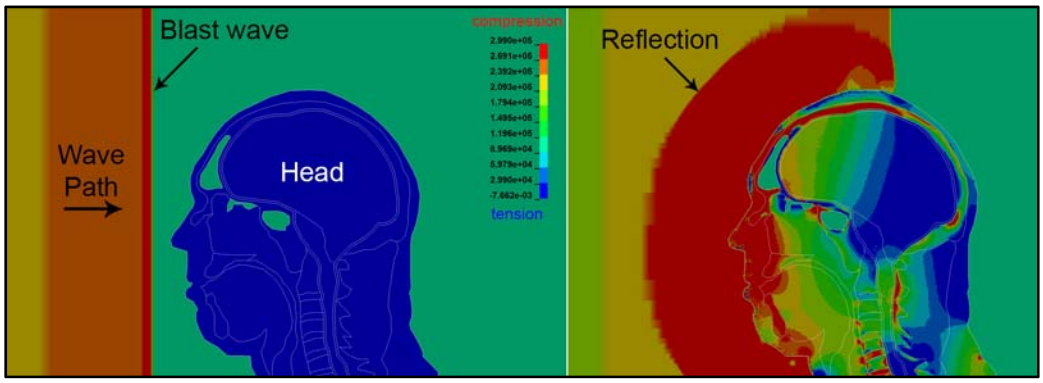

Figure 3. Blast wave interaction with the different layers of the head producing complex superposition of transmitted and reflected waves; Simulation performed using sagittal head model developed by Singh et al. [39]

1.2 Review of Cranium Anatomy

The skull is a complex structure formed by separate cranial and facial bones firmly joined by joints called sutures. The cranial bones (cranium) enclose and protect the brain, whereas the facial bones form the face and cavities for sensing organs. The cranial bones consist of dense layers of compact cortical bone known as the tables of the skull separated by a less dense layer of spongy cancellous bone known as the diploë [52]. The material properties of cranial bone in literature vary significantly such with any set biological samples (Table 1). Although two types of bone structures

(cortical and cancellous) make up the skull, in blast exposure computational studies the skull is sometimes treated as a single rigid material.

There are eight cranial bones: the frontal, paired parietal, occipital, paired temporal, sphenoid, and ethmoid bones (Figure 4). The frontal bone is shell–shaped forming the anterior cranium. The paired parietal bones are curved, and together, form a shell and most of the superior and lateral aspects of the cranium. The occipital bone forms the base and most of the posterior aspect of the cranium. The paired temporal bones form the inferolateral aspects and parts of the cranium base. The sphenoid bone is the central wedge joining all other cranial bones, helping form the base and sides of the cranium and the floors and sides of the eye sockets. Lastly, the ethmoid bone is located in front of the sphenoid bone helping form the roof and walls of the nasal cavity, and the floor of the eye sockets [52].

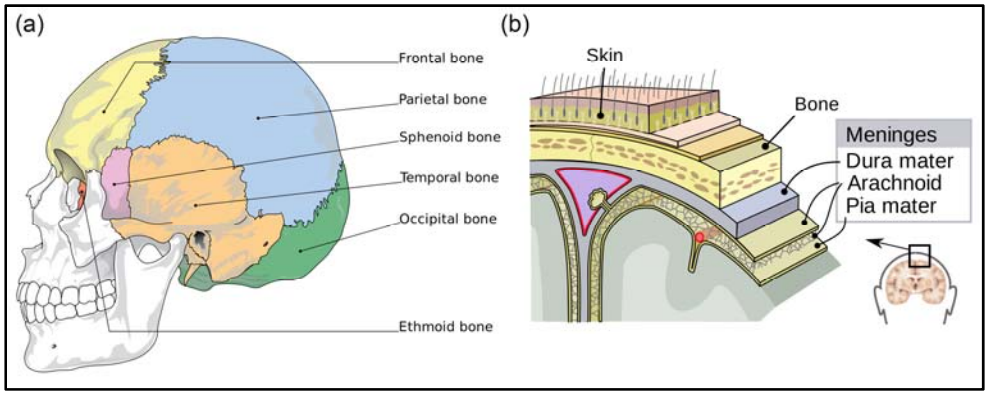

Figure 4. (a) Cranial bone anatomy and locations; (b) Meninges (connective tissues) below the cranial bone (figure adapted from [53, 54])

There are connective tissues that cover and protect the brain and spinal cord (central nervous system, CNS) called the meninges. The meninges form partitions within the cranium with the outermost called the dura mater, then the arachnoid mater, and lastly the pia mater (Figure 4). The dura mater is the strongest meninx and is made up of two layers, with the outer layer attached to the inner surface of the cranium and the second layer surrounding the arachnoid mater and CNS. The arachnoid mater forms a loose cover around the brain, whereas the pia mater forms a tight layer around the brain. The space between the arachnoid and pia mater is called the subarachnoid space and contains CSF [52].

Table 1. Summary of cranial bone material properties found in literature

Density (kg/m^3)	Poisson's Ratio	Moduli (Young's *E*/Shear *G*/Bulk *K*) (GPa)	Experimental/Numerical Notes	Ref
1410	0.19	E=5.38	Obtained from cadaver; used composite bone (tables and diploë)	[55]
–	–	E=14	Obtained from cadaver; separated outer and inner tables; tested at $\dot{\varepsilon} = 1.0\ s^{-1}$	[56]
1869 (inner), 1813 (outer)	ν_{12}=0.45, 0.42 ν_{13}=0.2, 0.21 ν_{21}=0.48, 0.47 ν_{23}=0.19, 0.19 ν_{31}=0.3, 0.34 ν_{32}=0.26, 0.27	E_1=13, 10.6 E_2=14.6, 12.8 E_3=21, 18.1 G_{12}=4.4, 3.6 G_{31}=5, 3.9 G_{23}=6.8, 5.9	Obtained from cadaver; modelled separate outer table and inner table	[57]
1561	0.379	E=7.92	Numerical model as single rigid material	[58]
1710	0.19	E=5.37		[41]
1412	0.22	E=6.5		[59]
1210	0.22	E=8		[37]
1800 (tables) 500 (diploë)	0.21 0.01	E=15 E=4.5	Numerical model of separated table and diploë layers	[60]
2100 (tables) 1300 (diploë)	0.22 0.24	E=15 E=1		[61]
–	–	E=10 (tables) E=0.6 (diploë)		[62]
2100 (tables) 1300 (diploë)	–	K=10.2 (tables) K=1.3 (diploë)		[43]

CSF is a fluid found in and around the CNS, primarily comprised of water and having a similar composition to blood plasma, but with differing ion concentrations and less proteins [52, 63]. The main constituents of CSF are sodium (Na^+), chloride (Cl^-), and bicarbonate (HCO_3^-) (Table 2) [64]. The total CSF volume in adults is approximately 150 ml. CSF nourishes and transports chemical signals to and from the brain such as hormones and protects the CNS from blunt trauma by acting as a cushion. Additionally, CSF helps regulate ICP protecting the brain from pressure changes and produces a buoyant force preventing the brain from crushing under its own weight by effectively reducing its weight by 97% [65].

Table 2. Summary of CSF properties found in literature

Properties	[66]	[67, 68]	[69]	[70]	[71]
Specific gravity	–	1.007	1.0069	–	1.006 – 1.008
Pressure (kPa)	–	–	1.47	–	0.88 – 1.77
Water (%)	99	>99	~99 with ~1.08% solids	–	–
Na^+ (mEq/L)	138	158	227.83	140	135–150
Cl^- (mEq/L)	119	138	147.61	90	116 – 127
HCO_3^- (mEq/L)	–	25	85.9	–	22.9
pH	7.33	7.35	7.48 (7.35 – 7.70) (post mortem pH of 6.38)	–	7.28 – 7.32

1.3 Overview of Blast Exposure Injury

Blast exposure leads to many types of injuries that are commonly categorized as primary, secondary, tertiary, and quaternary. Primary injuries are caused by the blast wave overpressure interacting with and propagating through the body leading to contusions, hematomas, lacerations, and herniation of internal organs [16, 37]. Primary blast injury was historically associated with injury to gas–containing organs such as the lungs and gastro–intestinal tract, but recently its relation to brain injury has become a prominent topic in blast [7]. Secondary injuries are the result of penetrating trauma caused by projectiles or fragments propelled by the expansion of gases, such as shrapnel. Tertiary injuries are caused by blunt trauma from large non–penetrating projectiles

and gross acceleration of the body onto its surroundings. Lastly, Quaternary injuries are the result of other injuries such as thermal, chemical, and nuclear effects of the explosion (Figure 5) [14, 16].

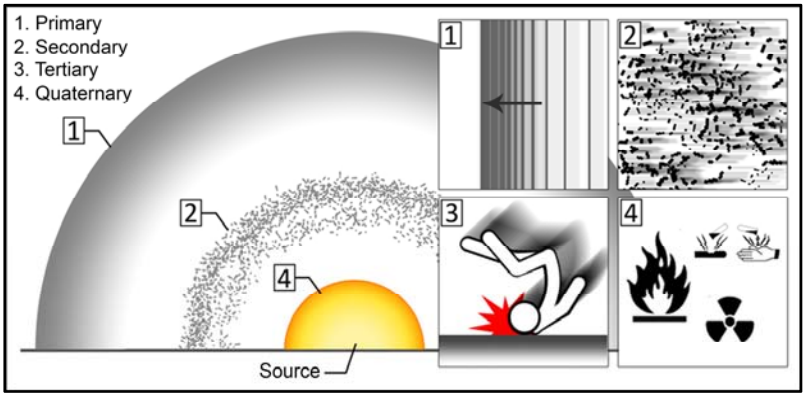

Figure 5. Blast injury mechanisms that can cause bodily harm in relation to a blast event

For the motivation of this thesis, only the blast wave interaction with the head without skull fracture will be discussed hereafter. Brain injury can be classified into two broad categories of focal and diffuse injuries. Focal brain injuries are locally well–defined lesions such as hematomas and contusions. Diffuse brain injuries form a wide range of injuries from mild concussions to diffuse white matter injuries. A crucial problem in trauma biomechanics is the lack of an assessment that correlate mechanical loading and severity of its resultant injury [16]. Such a correlation would allow for determining probabilities that describe likeliness of a specific injury from loading; however, challenges are met with the large biological variability in post–mortem surrogates (age, gender, post–mortem interval, etc.) and the unjustifiable experimentation on living subjects [16]. There are currently no assessments for head injuries that are directly related to blast exposure in terms of scales and injury criteria; however, some exist for automotive safety and triage applications that can be used for comparative benchmark.

The Abbreviated Injury Scale (AIS) is an anatomically–based standardized scale created in 1971 to assess the severity of loading and the risk of sustaining injury with respect to motor vehicle accidents [16]. The AIS correlates a function of physical parameters with the probability of a specific injury to a specific body region. A threshold value corresponding to a specific injury was obtained when it was observed in more than 50% of the crash test experiments performed

having comparable conditions. AIS is limited in that the experiments performed to obtain the threshold values used post mortem test objects as surrogates for living humans. The AIS is regularly updated by the Association for the Advancement of Automotive Medicine (AAAM) and widely implemented [12, 13, 16]. AIS for the head uses a non–linear scale from 1 (minor) to 6 (fatal) to classify specific head injuries based on medical diagnosis of the post–mortem test objects (Table 3).

Table 3. AIS scale for Head Injury

AIS Score	Description	Possible Injuries
1	Minor	–Laceration to the face –Headache, dizziness with no LOC –Fracture/dislocation of nose or teeth
2	Moderate	–Eye laceration or retinal detachment –Disfiguring lacerations –Undisplaced skull or facial fracture –Less than 15min LOC
3	Serious (non–life–threatening)	–Loss of eye or avulsion of optic nerve –Displaced facial bone fractures –More than 15min LOC –No severe neurological effects
4	Severe (life–threatening)	–Severe lacerations with dangerous haemorrhage –Definite abnormal neurological signs –Retrograde amnesia 3–12 hrs –Compound skull fracture
5	Critical	–More than 24hrs LOC –Retrograde amnesia more than 12hrs –Intracranial haemorrhage, edema –Decreasing state of consciousness
6	Fatal	–Death

The Glasgow Coma Scale (GCS) is another widely used scale that focuses on assessing the effects and severity of an injury with physiologic indicators rather than anatomy. It was devised in 1974 as a triage and prognostic indicator for CNS function [12, 13]. The GCS scale is based on first observation after the injury using verbal response, motor response, and eye opening, ranging from 3 (severe) to 15 (less severe). The GCS is the primary criterion for assessing and predicting the severity of most traumatic brain injuries in clinical trials and classifies mTBI with a score of

14–15; however, the assessment is limited in that it does not assess the cause [12, 59, 72–75]. Another notable limitation of the GCS is scoring an individual with preexisting limitations in verbal, motor, or eye response indirectly related to the injury.

A widely used head injury criterion initially proposed by Versace in 1971 and then later revised by the US National Highway Traffic Safety Administration (NHTSA) is the Head Injury Criterion (HIC). A HIC value is calculated by considering the resultant translational acceleration of the head over a specific time interval given by:

$$HIC = \max\left[\frac{1}{t_2 - t_1}\int_{t_1}^{t_2} a(t)dt\right]^{2.5}(t_2 - t_1) \qquad \textbf{Equation 1}$$

The HIC is used with the Wayne State University Cerebral Concussion Tolerance Curves (WSTC), which relates head injury with blunt impacts, and the Maximum AIS to determine the probability of head injury and severity due to translational acceleration [16, 76]. Other head injury criteria exist such as the Generalized Acceleration Model for Brain Injury Threshold (GAMBIT), the "3 ms criterion", the Brain Pressure Tolerance (BPT), and the Brain Injury Criteria (BrIC); however, HIC is the most widely used to predict the likelihood of head injury resulting from blast exposure [24, 36, 39, 77, 78].

1.3.1 Primary Blast Wave in the Head

Exposure of the head to a blast wave results in a wave reflection at the head–atmosphere interface and transmission of a compressive pressure wave into the head (primary pressure wave). The primary pressure wave transmits into the space surrounded by the cranial bones (cranial vault) and propagates through everything within (the brain, CSF, etc.). Theories of injuries as a result of the primary pressure wave propagating within the cranial vault include, soft–tissue damage from shearing [40, 79–81], distortion of brain tissue cellular structures and cell death [27, 74, 79, 82–86], and intracranial fluid cavitation [34, 39, 43, 79, 87, 88]. Due to the unjustifiable experimentation on living humans in injurious scenarios, *in vivo* measurements of brain response to blast do not exist. Studies often use surrogate models relating the results to determine the effects of the blast wave on the brain. Such models include, animal surrogates [38, 79, 81, 83–86, 89, 90],

post–mortem human surrogates [32], simplified ellipsoid head dummies coupled with numerical modelling [33, 34, 36, 40–42], and detailed head numerical models [11, 20, 22, 24, 35, 39, 43, 44, 59, 91–94].

A number of the literature showed that positive pressure occur within the head at the location of initial blast wave transmission (coup), and negative pressure at the opposite location (contre–coup) [14, 22, 24, 32–39]. For example, if the blast wave transmission occurred at the anterior of the head, negative pressures would occur at the posterior of the head. Likewise, if the blast wave transmission occurred at the left side of the head, negative pressure would occur at the right side of the head. Several experimental and computational studies such as those performed by, Sayed et al. [37], Moss et al. [24], Bir [32], and Singh et al. [39], reported that negative pressure occurred at the posterior region of the cranial vault from frontal or anterior blast exposure (Figure 6). The experimental study by Bir demonstrated that negative pressure occurred at the contre–coup regardless of head orientation using fresh un–embalmed post–mortem head surrogates for incident peak overpressures ranging from 0.093–0.154 MPa (Figure 7) [32]. The computational study by Singh demonstrated that the peak negative pressure occurred at the posterior region ranging from 0.211–0.70 MPa during frontal blast exposure for incident peak overpressures ranging from 0.170–0.326 MPa [39]. Similarly, a computational study by Zhang et al. [22] reported negative pressures ranging from 0.30–0.48 MPa as a result of a 0.35 MPa peak overpressure.

Some studies have suggested that the negative pressure occurs from the compressive primary pressure wave reflecting in tension due to the greater impedance of the skull compared to its surroundings (§ 3.2.1) [38, 92, 95], and some suggested that negative pressure is greatly exacerbated by the skull flexure resulting from blast loading [24, 33, 34, 84]. However, investigations of the latter effect have noted skull flexure occurring at later times compared with the onset of negative pressure [35]. It was also hypothesized that cavitation of CSF due to transient negative ICP is a possible injury mechanism that could lead to mTBI [34, 39, 43, 79, 87, 88]. Cavitation is the generation of voids or cavities in a fluid due to localized pressure changes and can collapse producing large forces on surrounding materials (§ Chapter 2). The limits of CSF cavitation are currently unknown and many numerical studies that have examined the effects of CSF cavitation on the brain used the estimated cavitation limit of water, which has a large range

of 0.1–120 MPa [8]. A computational study by Panzer et al. [43] modelled CSF cavitation occurring –0.1 MPa and demonstrated large localized positive pressures occurring in the brain from cavitation and the potential for injury. A study by Shively et al. [96] investigated post–mortem brain specimens from military service members with chronic blast exposures compared with non–military civilians without history of blast exposure. Shively reported prominent scarring in the brain immediately below the pia mater for the cases with chronic blast exposure, which were not observed in the cases without history of blast exposure. CSF is found in the subarachnoid space above the pia mater, and the observations reported by Shively support the hypothesis that CSF cavitation has the potential for brain tissue damage (Figure 4).

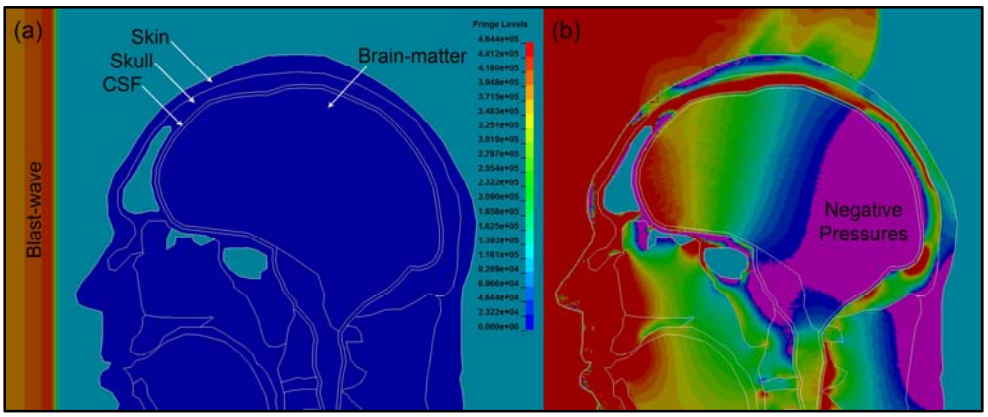

Figure 6. Negative pressures (magenta color) observed in computational study of frontal blast exposure; Simulation performed using sagittal head model developed by Singh et al. [39]

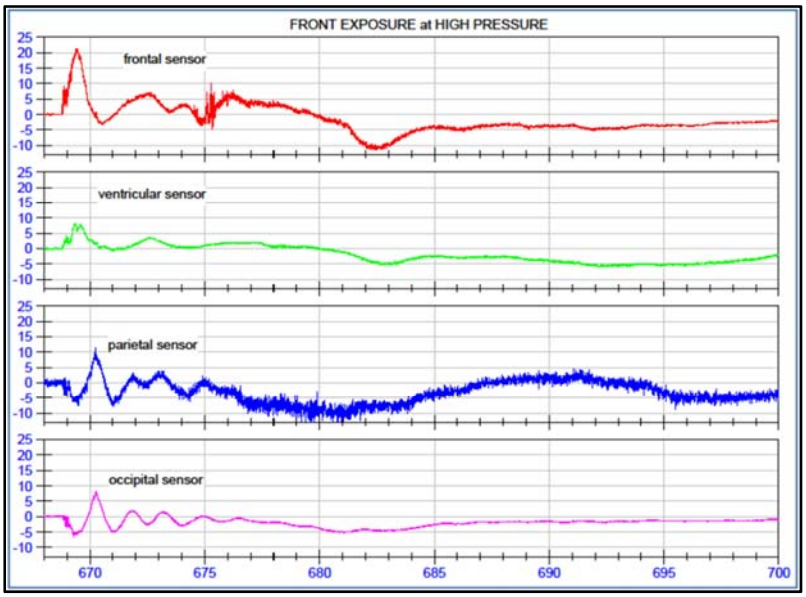

Figure 7. Experimental result of frontal blast exposure demonstrating negative pressure at the contre–coup (occipital sensor); adapted from Bir et al. [32]

1.4 Chapter Summary

In summary, blast waves are generated because of the expansion of gases from an explosion source. The pressure profile of a blast wave can be approximated by the Friedlander equation, which encompasses the propagating shock wave, or shock front, and negative phase caused by the over–expansion of the explosive gases. When a blast wave interacts with a structure, it generates a reflected wave at the interface that superimposes with the incident wave typically resulting in greater pressures. A pressure wave, the transmitted wave, is also transmitted into the structure propagating at the acoustic speed of that structure. Reflected and transmitted waves occur at every layer of differing density or acoustic speed within the structure, which can result in complex superposition of pressure waves. For the case of frontal blast exposure to the head in free air, a large pressure would be observed at the front of the face due to the reflection, and a complex pattern of pressure waves within the head due to the differing layers of material such as the skull and CSF. The skull is a complex bone structure of cranial and facial bones. The cranial bones consist of outer and inner tables of cortical bone separated by the diploë made of cancellous bone. CSF is a fluid found in and around the CNS, primarily comprised of water, protecting the CNS from blunt trauma by acting as a cushion, and regulating ICP.

Blast exposure classifies injuries as primary, secondary, tertiary, and quaternary. Primary blast injuries encompass injuries because of the blast wave generated from the explosion. It has been proposed that blast wave exposure can result in mTBI due to the number of mTBI cases reported by military service members exposed to in–theatre blast; however, the causes of blast–related mTBI is currently unknown. Assessment scales developed for automotive safety and triage exist that can correlate the effects of injury with its severity; however, such an assessment for correlating blast related loading with resultant injury severity does not exist. The HIC injury criterion for blunt impact was adopted for blast exposure as an indirect comparative benchmark. There is no consensus in the literature to the specific injury mechanisms that cause mTBI, with some suggesting CSF cavitation as a candidate. Negative pressures have been observed through experimental and computational blast exposure studies occurring at the contre–coup, which could exceed the negative pressure necessary for CSF cavitation. Cavitation would generate bubbles that violently collapse producing large localized pressures in the head. There are no *in vivo* studies of blast related CSF cavitation. Studies use models of the head and assumed CSF cavitation pressure thresholds to relate the dynamics observed to the potential of injury in living humans; however, the cavitation pressure threshold for CSF is currently unknown.

Chapter 2. Review of Cavitation

The term ‘cavitation’ appeared for the first time in England 1894 in a study investigating efficiency reduction of ship propellers with respect to rotation speed and ship forward velocity [97]. Recently, cavitation has become more relevant in other fields of study such as aeronautics, erosion control, piping, medical therapy, and blast. The traditional definition of cavitation is the generation of vapour cavities (bubbles) in a body of fluid as a result of a drop in fluid pressure at constant temperature. Alternatively, generation of bubbles in a fluid of constant pressure as a result of an increase in temperature is described as boiling [98, 99]. Although the first instance of cavitation appeared from fluid in motion, cavitation can occur in a fluid that is either in motion or at rest [100].

The occurrence of cavitation is associated with fluid tensile strength; similar to solids, fluids can fail due to rupture because of loading exceeding the fluid tensile strength. Cavitation can initiate as a result of homogenous or heterogeneous nucleation, where homogeneous nucleation results in cavitation at the fluid tensile strength due to breaking of intermolecular forces, and heterogeneous nucleation results in cavitation due to weaknesses in the system, and therefore, at much lesser magnitudes (§ 2.2). These two types of nucleation creates challenges in determining fluid tensile strength because rupture of the fluid often occurs as a result of heterogeneous cavitation well before the tensile forces exceed the fluid tensile strength limit. The vulnerability of fluid to rupture through heterogeneous cavitation prompted studies investigating homogeneous cavitation to use analytical methods coupled with measured experimental data to calculate theoretical fluid tensile strengths.

2.1 Fluid Tensile Strength

To measure the fluid tensile strength, negative pressure must be generated in which a cavity initiates within the body of the fluid. Therefore, tensile stresses high enough to overcome the cohesive forces of the fluid molecules are required to produce such a cavity. Theoretically these forces may be on the order of several thousands of atmospheres [101]. An example of a simple model for calculating the fluid tensile strength in terms of intermolecular forces is as follows [98]. Suppose two molecules are separated by a distance (x) by externally applied forces (F) and have

a potential energy (E_P) associated with their intermolecular force (F_{int}) (Figure 8). At x_0 the molecules are in equilibrium with minimum potential energy $\left(\frac{\delta E_P}{\delta x} = F = 0\right)$, and at x_1 the attractive intermolecular force is at its maximum. The ratio of $\frac{x_1}{x_0}$ is typically 1.1–1.2, corresponding to a bulk fluid fractional expansion $\left(\frac{\Delta V}{V_0}\right)$ of approximately $\frac{1}{3}$ as a result of three mutually orthogonal directions [98]. Therefore, tensile stresses resulting from the increase in F and increase in distance greater than x_1 would result in rupture of the fluid. The bulk modulus (K) of a fluid can be expressed as:

$$\Delta P = -K\left(\frac{\Delta V}{V_0}\right) \qquad \text{Equation 2}$$

and given the typical bulk modulus of 2.2 GPa for water [41, 102, 103], a theoretical tensile strength can be approximated using Equation 2 resulting in 0.733 GPa. This theoretical value is much greater than typically reported in experimental studies (§ 3.1) demonstrating the dissociation between the theoretically predicted and experimentally observed values.

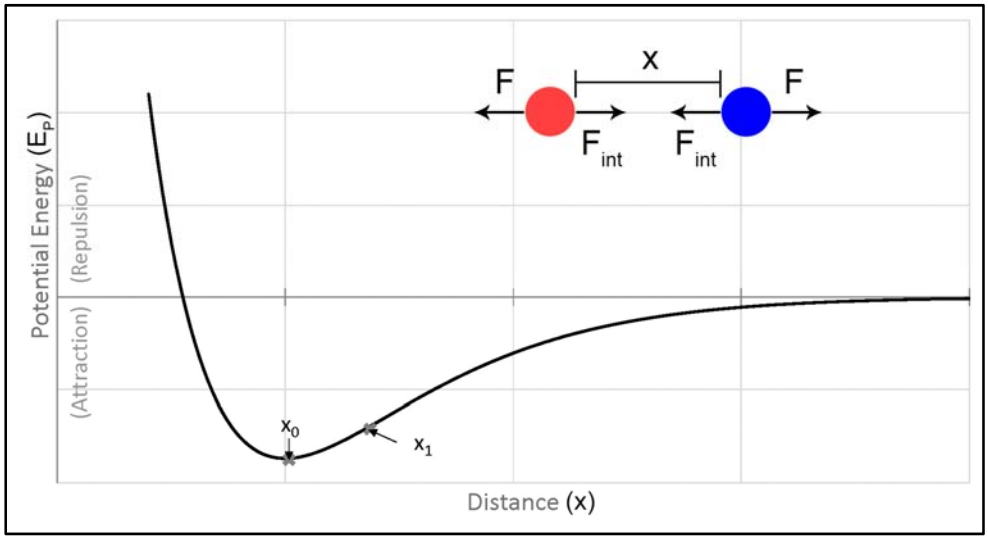

Figure 8. Potential energy (E_P) from attraction and repulsion of two molecules with respect to their distance (x)

The traditional definition of cavitation suggests that rupture at the fluid tensile strength could be achieved at the fluid vapour pressure, but there is a clear disconnect between the two

properties. Vapour pressure is the pressure of a vapour that is in thermodynamic equilibrium with its fluid at a specific temperature in a closed system [101]. Equilibrium results when the rate of fluid evaporation equals the rate of condensation, and therefore, vapour pressure is more applicable to the fluid boundaries that allow evaporation and condensation during a large time scale. Accordingly, vapour pressures are not reported as the fluid tensile strengths (§ 3.1). The theory of tensile strength of pure fluids predict that a vapor cavity will only form under extremely large tensions, and in the case of boiling only in very large superheats. Since these large tensile and superheats were not observed in experimental studies, the idea of nucleation was introduced. The idea of nucleation suggests that fluids have pre–existing vapour cavities already beyond molecular dimensions and are able to grow into macroscopic bubbles under moderate tensions resulting in rupture below the tensile pressure [97].

2.2 Homogeneous Nucleation

The occurrence of cavitation can be categorized into homogeneous and heterogeneous nucleation. Homogeneous nucleation occurs when an existing cavity, generally presumed as the result of random molecular motions, exceeds a critical nucleus radius (R_{CR}), increasing the favourability of transforming into a stable vapour phase nucleus. In general, homogeneous cavitation occurs when the fluid tensile strength is exceeded. The following presents a simplified version of the classical homogeneous nucleation theory omitting details in terms of thermodynamics and probability [98]. This approach is similar to the model used for approximating the fluid tensile strength in which rupture occurs after exceeding an intermolecular distance. Suppose a fluid at a constant pressure (P_∞) and temperature (T) has a single spherical bubble initially at equilibrium with a radius (R), containing vapour with an internal pressure (P_v) (Figure 9). Sectioning the bubble in half and performing a force balance results in:

$$\Delta P = P_v - P_\infty = \frac{2 * \gamma}{R} \qquad \text{Equation 3}$$

where γ is the coefficient of surface tension of the fluid. It is assumed that this approximation can be extended down to bubbles with radii of intermolecular distances [104]. Therefore, if P_∞ is less than $P_v - \frac{2*\gamma}{R}$, the bubble will grow and alternatively, if P_∞ is greater than $P_v - \frac{2*\gamma}{R}$, the bubble will

shrink. If the bubble grows to the critical radius ($R \rightarrow R_{CR}$) at which it ruptures, then ΔP corresponds to the fluid tensile strength (ΔP_{fts}). Using Equation 3, the typical surface tension of 0.0728 N/m for water at 20 °C [105], and a radius of 10^{-10} m comparable to intermolecular distances [98], results in a fluid tensile strength of approximately 1.456 GPa, comparable to the order of that obtained using Equation 2 (§ 2.1).

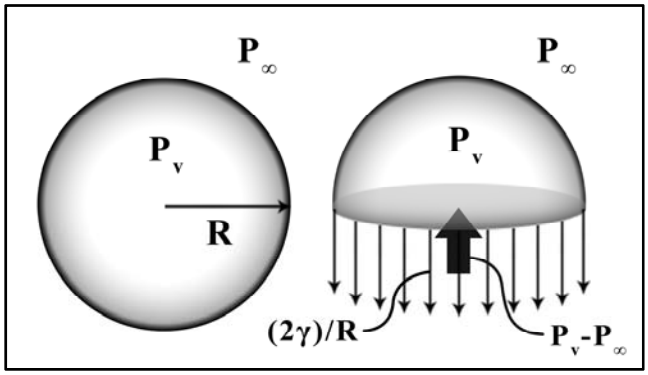

Figure 9. Simple spherical bubble model for dynamic analysis of homogeneous nucleation

A second expression that must be considered is the free energy (W) required to initiate nucleation. Assuming a nucleus is in equilibrium with its surrounding after its creation, energy must be deposited in two parts given by:

$$W_{hom} = (4\pi R^2)\gamma_S - \left(\frac{4}{3}\pi R^3\right)\Delta P \qquad \text{Equation 4}$$

where γ_S is the surface energy. The first term is the energy required for the increasing surface area of the bubble and the second term is the work done to displace the bulk fluid volume outward. At the beginning of nucleation, the energy required increases with radius as the surface term dominates. Once the nucleus reaches the critical radius ($R \rightarrow R_{CR}$ and $\Delta P \rightarrow \Delta P_{fts}$), the bulk term begins to dominate, decreasing the energy required (Figure 10). The maximum energy corresponding to the critical radius is known as the nucleation barrier (W^*_{CR}). To generate fluid rupture as a result of homogeneous nucleation, and therefore exceed the fluid tensile strength, the energy deposited into the system to activate nucleation must be equal or larger than the nucleation barrier. Simplifying Equation 4 by substituting Equation 3 to remove dependence on R, results in:

$$W_{CR}^{*} = \frac{16\pi\gamma_S^3}{3\Delta P_{fts}^2} \qquad \text{Equation 5}$$

The nucleation barrier is the critical deposition energy for classical nucleation theory first formulated by Gibbs in 1961, and accordingly, the energy is referred to as Gibbs free energy. For a greater detailed description of classical nucleation theory and the consideration of the probability of a nucleation event, the reader is referred to [98, 104, 106, 107]. Intuitively, it can be deduced that the increase of temperature would increase the kinetic energy of the fluid molecules (Newtonian kinetic energy), decrease surface energy (the Eötvös rule), increase vapour pressure (Clausius–Clapeyron relation), and therefore decrease the fluid tensile strength.

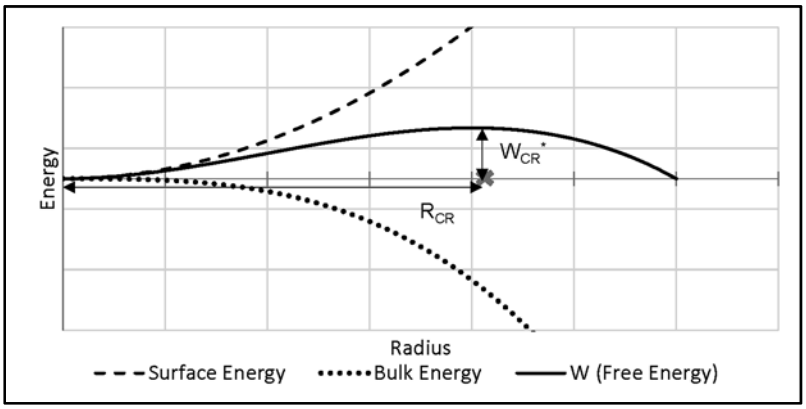

Figure 10. Free energy required overcoming surface and bulking energy for spherical homogeneous bubble nucleation

2.3 Heterogeneous Nucleation

The more common type of nucleation seen in application is heterogeneous nucleation, which occurs when bubbles nucleate from existing weaknesses in the fluid such as fluid–boundary interfaces, suspended particles, and dissolved gases [98, 99, 101, 108–110]. These weaknesses provide existing nuclei for cavitation resulting in rupture at negative pressures much lesser than those predicted for homogenous cavitation; henceforth, the term ‘cavitation pressure threshold’ will describe the fluid pressure that, when exceeded, cavitation from heterogeneous nucleation is observed.

Contaminant microscopic gas bubbles present in crevices on the surfaces of solid boundaries or suspended particles can act as nuclei for cavitation. In tap–water, the persistent contamination of microscopic air bubbles create challenges and generally require de–gassing or a settling period of several days before experimental testing [98, 102]. Dissolved gases in a fluid, such as tap–water, are troublesome to remove, and even with high pressure treatment and degassing can still exist causing heterogeneous cavitation [98]. Overton et al. [111] demonstrated an increase in the cavitation pressure threshold from 0.0871 MPa for fresh tap–water with a vapour saturated condition to 0.178 MPa for fresh tap–water with a degassed condition. An increase in cavitation pressure thresholds from degassing were also reported for deionized water and sea–water with an increase from 0.0952 MPa to 0.187 MPa and 0.0831 MPa to 0.203 MPa, respectively. Dissolved gases with vapour pressures lesser than the solvent fluid also act as heterogeneous cavitation nuclei due to their difference in partial pressure. Sedgewick et al. [112] reported that reducing dissolved gases by boiling demonstrated an increase in cavitation pressure thresholds for water and deionized water from 0.912 MPa to 1.17 MPa and 1.01 MPa to 1.47 MPa, respectively. Similarly, Overton et al. [113] reported an increase in tap–water from 0.861 MPa to 0.912 MPa after boiling.

The hydrophobic or hydrophilic property of solid boundaries are an important property when minimizing surface contaminant bubbles. Hydrophobic surfaces tend to repel polar molecules like water, and therefore, encourage large cavities at the surfaces. On the other hand, hydrophilic surfaces tends to be ‘wetted’ by water discouraging large cavities at the surfaces [98]. However, the minimum dimensions of cavities as a result of hydrophilic surface heterogeneous cavitation can be comparable to those required for homogenous cavitation, and therefore, produce comparable fluid tensile strength measurements [98]. It has also been observed that solid particles in a purified fluid can act as nuclei resulting in heterogeneous cavitation [97]. Consequently, cavitation occurring from contamination of sub–micron sized particles results in challenges with distinguishing whether nucleation occurred by homogeneous or heterogeneous conditions [98]. Couzen et al. [113] reported a lesser cavitation pressure threshold of 0.861 MPa for ordinary tap–water compared to 1.01 MPa for a purer sample of deionized water.

Similar to homogeneous cavitation, the free energy associated with heterogeneous nucleation can be determined by [114, 115]:

$$W_{het} = W_{hom} * f_{het}(\theta) \qquad \text{Equation 6}$$

where the function $f_{het}(\theta)$ reduces the homogenous cavitation free energy (W_{hom}) and given by:

$$f_{het}(\theta) = \frac{1}{4} * (2 + \cos\theta) * (1 - cos\theta)^2 \qquad \text{Equation 7}$$

The free energy for homogeneous cavitation assumes spherical nuclei, whereas in heterogeneous cavitation the nuclei are non–spherical. Equation 7 takes into account the non–spherical geometry using the contact angle that effectively lowers the energy required for growth (Figure 11). The contact angle can range from 0° to 180°, where for $f_{het}(180°) = 1$ full wetting of the surface occurs yielding homogeneous nucleation, and for $f_{het}(0°) = 0$ no wetting of the surface occurs yielding no barrier for nucleation at the surface. Given the same fluid parameters, the free energy for heterogeneous nucleation is lesser than that for homogeneous nucleation demonstrating the favourability of heterogeneous cavitation (Figure 12).

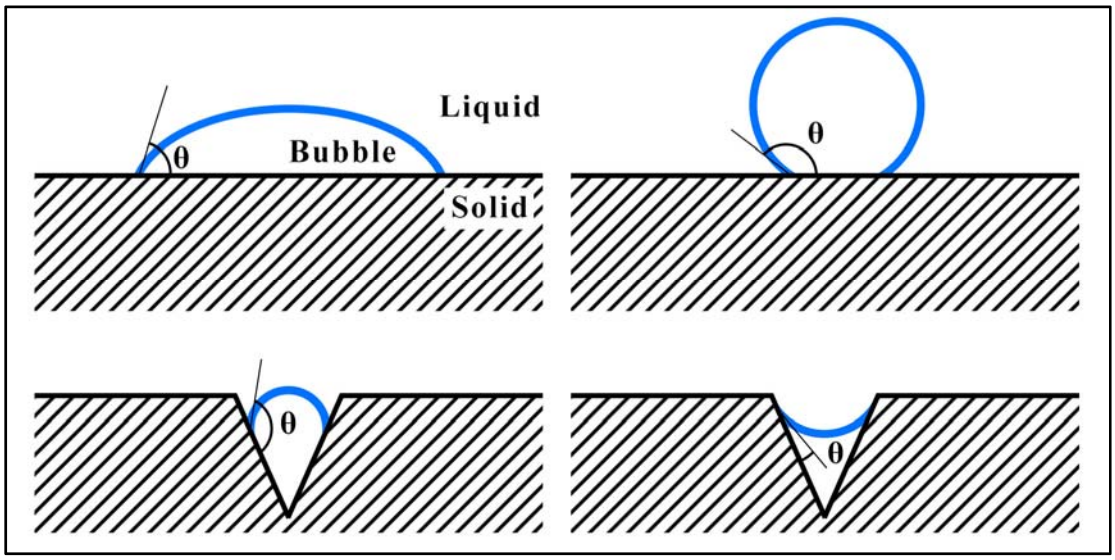

Figure 11. Examples of contact angle for a bubble between a liquid and solid

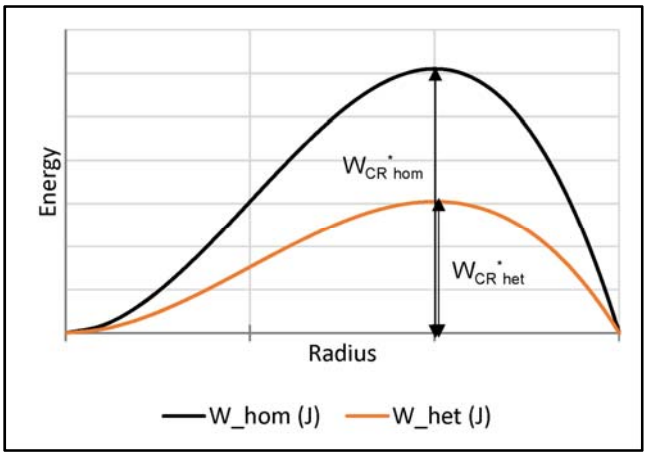

Figure 12. Free energy comparison of homogeneous cavitation versus heterogeneous cavitation

2.4 Brief Overview of Bubble Dynamics

The growth of cavitation bubbles can be categorized as either stable or transient. Stable growth occurs through a slow process of net inward diffusion of gas known as rectified diffusion. This type of growth can be observed in acoustic methods (§ 3.1.1) that show slow growth and partial collapse of the bubble due to the periodic acoustic waves. Transient growth occurs within a short duration, such as from dynamic pressure, resulting in rapid growth and violent collapse. For transient growth, the cycle of growth and collapse occurs faster than the diffusion of gases into the bubble resulting in near vacuum pressures within the bubble [116]. Bubble growth as a result of diffusion is termed degassing or gaseous cavitation, whereas when induced by dynamic pressure it is termed vaporous cavitation [100]. Since the collapse of bubbles are implosive, the severity of the implosion decreases with increasing vapour content, which acts as cushioning [100]. For the motivation of this thesis, only cavitation with transient growth induced by dynamic pressures will be discussed hereafter.

The collapse of transient bubbles can be categorized into 2 types, spherical and non–spherical collapse [101]. Spherical collapse is associated with the symmetrical compression of the bubble walls from evenly distributed pressure. Due to the complex behavior of cavitation bubbles in experiments, estimates of collapse pressures have been made ranging from low pressures due to air content providing cushioning during collapse, to large pressures in the order of 1–10 GPa. The scatter of predicted values are the result of the different analytical models used and treatment of

the vapour within the bubble. Non–spherical collapse is associated with a pressure gradient resulting in a violent asymmetrical collapse producing jets of fluid (micro–jets). Micro–jets can produce large localized pressures that can damage boundary materials (Figure 13). This type of damage is observed in erosion applications [99] and is used advantageously in biological therapy applications [87, 117–120]. The fluid surface tension is important to the dynamics of bubble collapse. An increase in surface tension tends to increase the rate of collapse, and viscous and compressibility effects tend to reduce the maximum attainable collapse pressure [101].

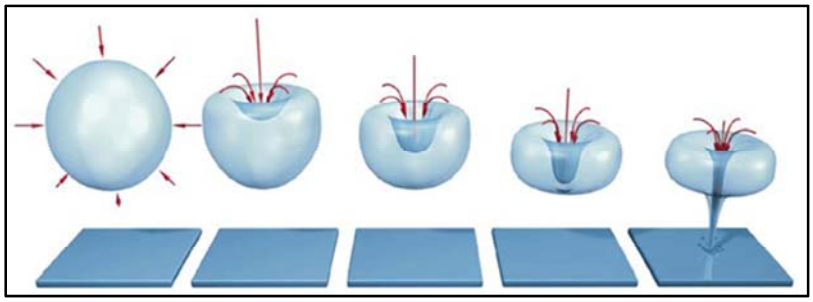

Figure 13. Demonstration of boundary damage as a result of non–spherical cavitation bubble collapse producing micro–jets (Figure adapted from [100]**)**

2.5 Chapter Summary

In summary, cavitation is the generation of stable or transient vapour bubbles as a result of a drop in fluid pressure of constant temperature, where transient cavitation is the result of dynamic changes in pressure. The initiation of cavitation can occur through homogeneous and heterogeneous nucleation. Homogeneous nucleation occurs from a cavity, presumed to result from random molecular motion, exceeding a critical nucleus radius resulting in fluid rupture. Heterogeneous nucleation occurs from existing weaknesses in the fluid such as solid boundary interfaces, suspended particles, and dissolved gases. The fluid tensile strength is obtained from homogeneous cavitation; however, weaknesses in the fluid require far less tension to generate rupture, and therefore, heterogeneous cavitation is more apparent in application. Heterogeneous cavitation creates challenges in determining fluid tensile strengths because experimental values measured are far less than theoretical values, specifically with water samples.

There is a large scatter in reported cavitation pressure thresholds for water that vary due to differences in experimental methods, rate of loading, temperature, fluid purity, and container surface roughness. There is also a scatter of predicted bubble collapse pressures that vary due to differences in analytical methods and treatment of the vapour within the bubble. It has been experimentally demonstrated that transient cavitation bubble collapse produces large localized pressures that can damage boundary materials through the creation of micro–jets.

Chapter 3. Experimental Methods to Generate Cavitation

3.1 Experimental Cavitation Test Methods

There are many methods in the literature that can generate fluid cavitation, but only dynamic methods applicable to blast exposure will be discussed. The dynamic methods for generating fluid cavitation discussed are the Tube–Arrest (T–A), Bullet–Piston (B–P), and Fluid–Hopkinson bar (F–Hb). The well–developed acoustic method will also be briefly discussed for noteworthy reasons and its limitations regarding the goal of this thesis (§ 4.1). The limitations of the dynamic methods will also be discussed at the end of this subsection.

3.1.1 Acoustic Method

While the acoustic method is not a dynamic method, it is worth briefly discussing its ability of generating fluid cavitation because many studies exist and provide relatively consistent results in the biological [87, 117–120] and erosion applications [99, 108, 121–124]. The acoustic method uses periodic high frequency acoustic waves to subject fluid through cycles of compression and tension as a result of its positive and negative phases, respectively [124]. When the amplitude of the acoustic wave is sufficiently high, cavitation bubbles are generated and grow at the negative–half of the cycle and partially collapse during the positive–half. As a result of the cycles imposed on the bubbles, they undergo asymmetric growth and collapse. That is, the rate of diffusion of dissolved gases into the bubbles is greater than the rate of diffusion of gases out of the bubbles [108, 116, 125–127]. This mechanism of rectified diffusion implies that the periodic waves encourage diffusion of gases into the bubbles and effectively reduces the observed fluid tensile strength and limiting its use; therefore, it will not be discussed in more detail because it is not relevant to the goal of this thesis.

3.1.2 Tube–Arrest Method

The T–A method of producing cavitation uses a tube semi–filled with a column of fluid, which is given an upward velocity by use of springs attached to the tube [124]. The tube is displaced an initial distance and then suddenly released resulting in the upward velocity before being arrested by a fixed stop. After impact, the fluid tends its upward motion generating a tensile

pulse that propagates downwards from its free–surface. Varying the imposed velocity on the tube affects the amplitude of the generated tensile pulse. When the pulse reaches the base of the tube, cavitation is captured by use of high–speed imaging. Methods of fluid pressure measurement varied throughout the development of the apparatus beginning with indirect measurements outside the tube to direct measurements at the base of the tube.

Chesterman [128] performed tests with this method using a 1000 mm length glass tube with an internal diameter of 11.5 mm. The tube was mounted vertically such that it could be moved a maximum vertical distance of approximately 50 mm. Rubber–tensioned supports were connected to the side of the tube such that, when the tube was pulled down and suddenly released, it would rise and become arrested by the buffer resulting in cavitation at the base of the fluid. At rest, the tube was against a fixed rubber buffer preventing its upward motion (Figure 14). The velocity of the tube at the instant of impact was varied from 2 to 6 m/s, and the initial static fluid pressure at the base was varied by changing the height of the fluid. In some experiments, Chesterman used a Perspex tube with an internal section of 15 x 15 mm to overcome optical distortion of cavitation. Chesterman did not directly measure the fluid pressure at which cavitation was generated, but instead used this method to study the effects of surface tension on the growth and collapse cycles of cavitation with varying initial static pressures. Pressure values were indirectly measured using a hydrophone in a surrounding water tank at a distance of 50 mm; however, Chesterman reported that the pressure traces measured were insignificant due to the reverberation in the tank.

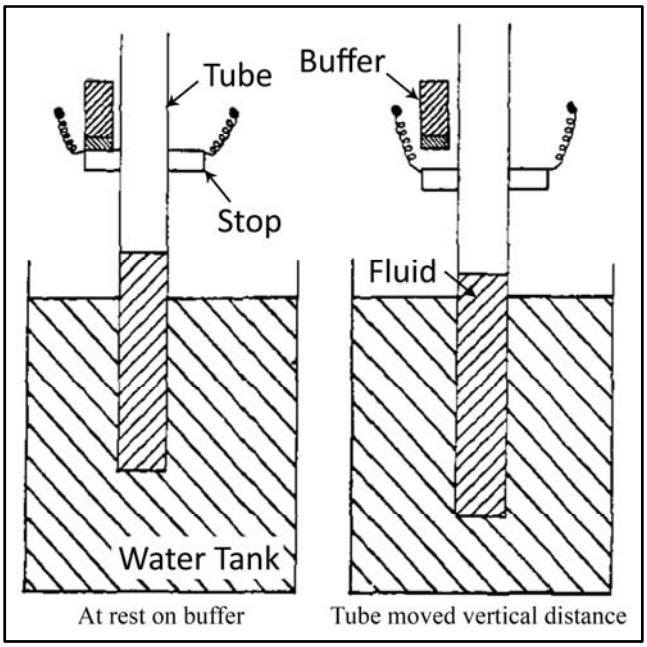

Figure 14. Tube–Arrest apparatus schematic used by Chesterman showing the tube filled with a column of fluid inside a surrounding water tank (Figure adapted from [128]**)**

Hansson et al. [129] used a similar method; however, the impact was the result of a moving mass rather than the moving tube. A flat–bottomed Plexiglass tube having an internal section of 18 x 12 mm was filled with fluid, mounted vertically, and supported by springs. Impact of a mass at the upper–end caused a downward acceleration of the tube producing a tensile pulse at the base of the fluid column. Hansson reported that for a water column of 180 mm height, a peak negative acceleration of 1.59×10^4 m/s^2 with a duration of 0.20 ms produced a cluster of cavitation bubbles at the base. Hansson calculated the fluid pressures using measurements from an accelerometer mounted at the base of the tube.

Overton et al. [111] further developed the T–A method by using a 1000 mm glass tube with an internal diameter of 24 mm and a thickness of 3 mm, containing a fluid column of 50 mm. This tube was also mounted vertically, supported by two springs, and had fixed Tufnol stops. Overton mounted a piezoelectric transducer in a cylindrical rubber block forming the base of the tube. Figure 15 shows pressure measurements reported for typical non–cavitating and cavitating conditions. Overton reported effects of stressing frequency on cavitation pressure thresholds for

carbon tetrachloride, kerosene, fuel, deionized water, glycerol solution, tap–water, engine lubricating oil, and invert emulsion.

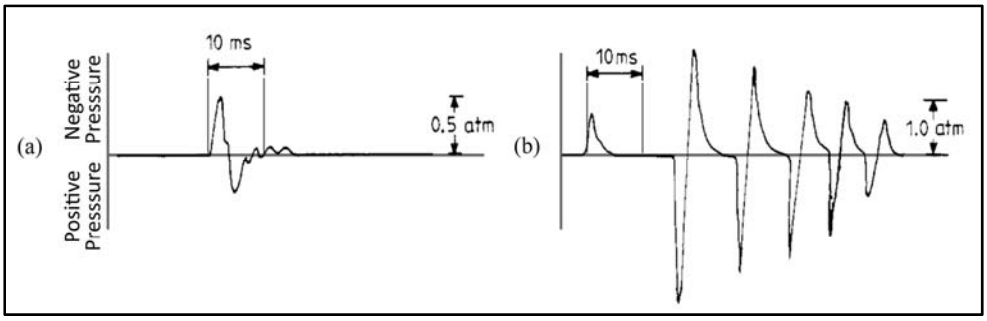

Figure 15. Typical T–A method pressure measurements for non–cavitating (a), and cavitating conditions (b) reported by Overton (Figure adapted from [111]**)**

Williams et al. [124, 130–134] further developed the reliability and repeatability of the T–A method with an improved apparatus consisting of a cylindrical polycarbonate tube with a length of 1000 mm and an internal diameter of 21 mm [131]. The tube was mounted vertically and supported by three adjustable springs. To measure fluid pressures, two pressure transducers were flush–mounted in the sidewalls of the tube and one mounted on a nylon block forming the base of the tube. The transducers measured more detail of the propagating pressure pulses because of the greater sampling rates used compared with previous works. Williams performed tests with 'nuclear–grade' deionized water from a two–stage reverse–osmosis ion–exchange purification system at 20 °C reporting agreement of the cavitation pressure threshold measured with nucleation theory [134].

Overton et al [111] reported an increase in cavitation pressure threshold with increasing sample purity and after degassing the samples (Table 4). Williams et al [134] reported thresholds two orders of magnitude greater for ultra–pure 'nuclear–grade' deionized water samples.

Table 4. Measured pressures at which cavitation was observed for differing water samples tested using the T–A method

Fresh tap–water	–0.0871 MPa (saturated) [111]	–0.178 MPa (degassed) [111]
Deionized water	–0.0952 MPa (saturated) [111]	–0.187 MPa (degassed) [111]
Sea–water	–0.0831 MPa (saturated) [111]	–0.203 MPa (degassed) [111]

'Nuclear–grade' deionized water	~ –56.6 to –70.2 MPa [134]

3.1.3 Bullet–Piston Method

The B–P method of generating fluid cavitation uses the tensile reflection of a generated compressive pressure pulse to produce negative pressure in the fluid [124]. A compressive pulse is generated at the base of a fluid column and propagated upwards toward the free–surface of the fluid open to the atmosphere. The compressive pulse reflects at the free–surface as a tensile pulse due to the lesser acoustic impedance of the air compared to the fluid (§ 3.2.1). This tensile pulse then propagates down the fluid column producing negative pressure. Multiple pressure transducers mounted at differing heights on a vertical tube containing the fluid measure the propagating pulses. As the tensile pulse increases with the increasing compressive pulse, the measured tensile peaks begin to 'plateau' due to the occurrence of cavitation at the free–surface. This plateau is the apparent cavitation pressure threshold and is reported as the maximum amount of tension the fluid can withstand at the fluid–atmosphere interface at the given tests conditions.

Couzen [135] performed experiments using the B–P method by propagating a compressive pulse upwards a vertical column of fluid and producing a tensile pulse reflection at the free–surface. The fluid was contained in a vertically mounted cylindrical stainless steel tube with its upper–end open to the atmosphere and its lower–end closed by a stainless steel piston (Figure 16a). The piston at the lower–end was machined such that it would have sliding fit without fluid leakage. The tube had an external and internal diameter of 31.5 mm and 25.4 mm, respectively, and consisted of two parts of 1200 mm and 20 mm lengths joined together by a flange joint. The compressive pulse was generated by impact of a bullet from a 0.22" caliber rifle mounted beneath the piston. The general shape of the generated pulses had a rapid rise with a rise time of approximately 50 μs and a gradual decay over a few hundred microseconds (Figure 16b). Two piezoelectric transducers mounted at different points of the tube measured the pulse propagation with an estimated recording accuracy of ±2%. The tests subjected fluids to increasing compressive pulses, and recorded the peak values of the tensile pulse reflection. As Couzen increased the input pulse, the peak values of the tensile pulse reflection also increased until reaching a constant limit

demonstrating the apparent cavitation pressure threshold (Figure 16c). Couzen performed tests on tap–water, boiled water, and boiled deionized water [113], along with silicon fluids of various viscosities; and similarly, Bull [136] performed tests on syrup, glycerol, and olive oil reporting relationship of cavitation pressure threshold with viscosity.

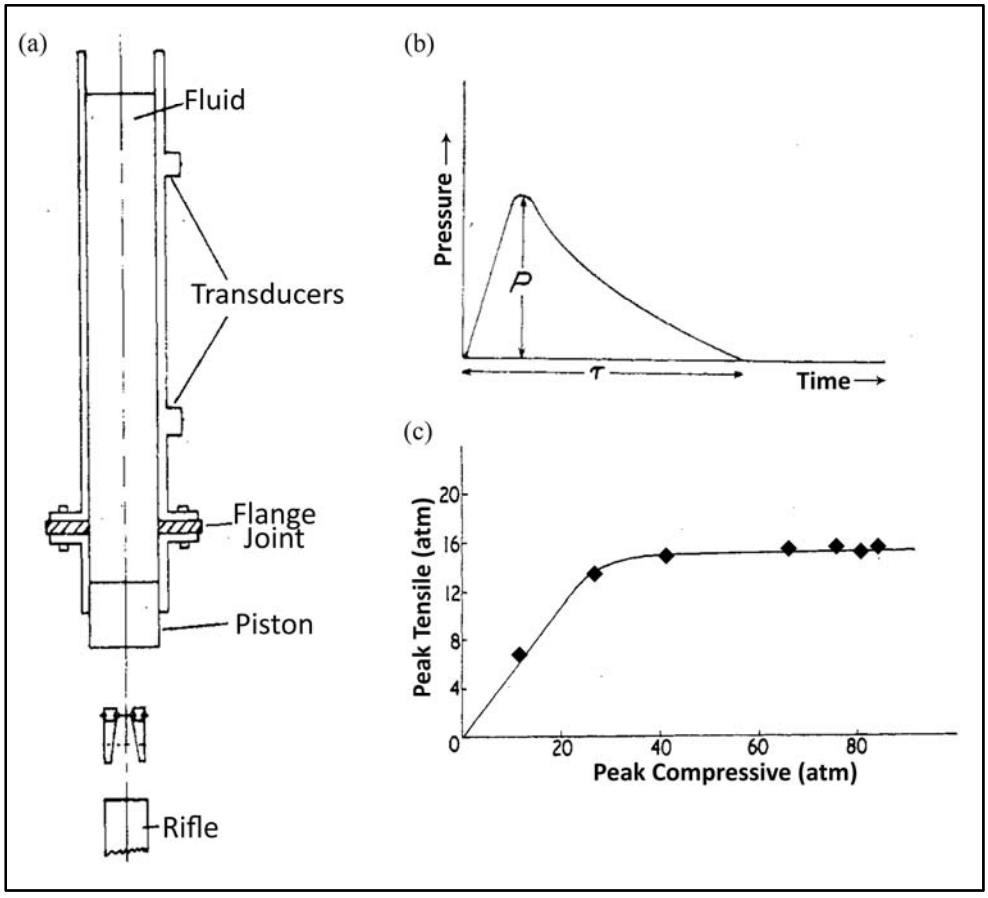

Figure 16. (a) B–P apparatus schematic; (b) Typical compressive pulse generated; (c) Constant tensile pulse (*T*) measured with increasing compressive pulse (*P*) representing the fluid cavitation pressure threshold (Figure adapted from [135]**)**

Sedgewick et al. [112] performed studies using this method with 1400 mm long tube of internal and external diameters of 25.4 mm and 32.0 mm, respectively. The studies showed that deionizing and boiling tap–water increased its cavitation pressure threshold. The effect of temperature was also studied showing that the cavitation pressure threshold peaked at approximately 4 °C, corresponding to the temperature at which the density of water is at its

greatest. Another study performed by Sedgewick et al. [137] tested water with polyacrylamide additives and reported decreasing cavitation pressure threshold with increasing viscosity, opposite of that reported by Couzen [135] and Bull [136].

Overton et al. [138] performed a study of the B–P method focusing on the characteristic of the generated compressive pressure pulse in the loading piston. Overton found that upon reaching the fluid, a portion of the compressive pulse was transmitted upward through the fluid while the balance was reflected downward as a tensile pulse in the piston. Upon reaching the base of the piston, the tensile pulse was reflected upward towards the fluid as a compressive pulse, completing a cycle. This produced a number of successive compressive pulses with decreasing amplitude in the fluid, which generated the compressive pulse shape (Figure 16b) as a result of superposition. It was concluded that the compressive pulse duration increases with increasing piston length. Overton et al. [139] also performed a study focusing on the bullet and its effect on the stress–rate showing that stress–rate and the cavitation pressure threshold increases with increasing bullet momentum. Additionally, Overton studied the attenuation of the pulses concluding that attenuation effects were less pronounced at greater bullet momentums.

Williams et al. [140, 141], performed studies on resolving issues of anomalously low cavitation pressure thresholds measured using the B–P method versus other methods. Williams used an improved B–P apparatus with a vertically mounted stainless steel tube having a length of 1400 mm, an internal diameter of 24.3 mm, and a steel piston inserted at the lower–end. A 0.25" caliber bolt stun–gun replaced the rifle of the previous B–P apparatus providing impact from a bolt rather than a bullet. Tests were performed on 'nuclear–grade' deionized water at 20 °C using transducers with shorter rise–times of 1 μm and greater sampling rate (10 MHz) compared to previous works (~10 kHz). Williams concluded that the discrepancies between the low cavitation pressure thresholds reported by previous studies using the B–P method and those reported from other non–dynamic methods were the result of deficiencies in the techniques of recording dynamic tensions. Using this improved apparatus Williams performed tests on degassed and deionized water, and silicone oils of various viscosities [109, 140, 141].

Similar to the trends observed with the T–A method, studies using the B–P method demonstrated that the cavitation pressure threshold increases with increasing sample purity (Table 5).

Table 5. Measured pressures at which cavitation was observed for differing water samples tested using the B–P method

Ordinary tap–water	–0.861 MPa [113]	–0.912 MPa [112]
Deionized water	–1.01 MPa [112]	
Boiled water	–0.912 MPa [113]	–1.17 MPa [112]
Boiled deionized water	–1.52 MPa [113]	–1.47 MPa [112]
'Nuclear–grade' deionized water	~ –4.5 to –13.0 MPa [140]	

3.1.4 Fluid–Hopkinson Bar Method

The Fluid–Hopkinson bar (F–Hb) method of producing fluid cavitation uses a tensile pulse reflection of a generated compressive pulse resulting from a projectile impact; similar to the B–P method. The generated compressive pulse travels upwards a piston called the loading rod and through a fluid column confined in a tube. Upon reaching the free–surface of the fluid, the compressive pulse reflects in tension, and generates cavitation following the same plateauing principle described for the B–P method.

Kenner [142] developed this method using an apparatus consisting of a stainless steel tube with a length of 910 mm and an internal and external diameter of 25.4 mm and 38.1 mm, respectively (Figure 17). A loading rod with a length and diameter of 610 mm and 25.4 mm, respectively, was inserted at the base of the tube with a rubber o–ring to provide a leak–free seal. The tube was filled with fluid with the top exposed to the atmosphere. The tube and loading rod were mounted vertically using rubber clamps, and an air gun, mounted below the loading rod, propelled a steel sphere at the base of the rod to generate the compressive pressure pulse. Strain gauges were mounted onto the loading rod to measure the propagating pulses and two piezoelectric pressure transducers were flush–mounted to the inner surface of the tube. Kenner was able to generate compressive pulses with a duration ranging from 70–560 μs using an acrylic rod, and durations as short as 30 μs using an aluminum rod. Kenner measured the cavitation pressure

thresholds of water [142], ethyl alcohol, glycerin [103], and fresh human blood [102]. To reduce the variability of the apparatus, Kenner sealed the upper–end of the tube and used a vacuum pump to expedite the dissipation of air bubbles in the fluids before testing [102]. Kenner reported negative cavitation pressure thresholds of 2.96 MPa [142] and 3.09 MPa [102] for degassed water.

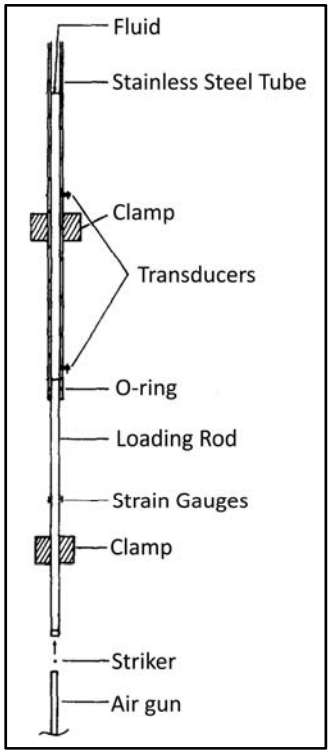

Figure 17. F–Hb apparatus schematic used by Kenner (Figure adapted from [142]**)**

3.1.5 Limitations of Dynamic Methods

There is a large scatter in reported cavitation pressure thresholds for water that vary due to differences in experimental methods, rate of loading, temperature, purity, and surface roughness of the container [122]. Studies from the literature demonstrated that the T–A method is effective in studying the dynamics of cavitation cluster growth and collapse of fluids, whereas both the B–P and F–Hb methods are effective in determining the maximum tension a fluid can withstand for their given systems. The limitations of the methods discussed above with respect to the goal of this thesis are as follows: (1) the lack of loading adjustment, (2) the large fluid volume requirements, and (3) the lack of a greater impedance boundary fully surrounding the fluid.

A considerable disadvantage recognized from the T–A and B–P methods is the process of varying the shape and duration of the incident pulses generated. Considering the T–A method, the impact velocities were generally reported as the driving parameters rather than stress or pressure. Different materials and geometry of tubes were used between studies; therefore, tensile pulses generated by the reported impact velocities are unique between the different apparatuses. The T–A method does not provide a solution for varying the incident wave duration and a great deal of the apparatus would require modification to solve this issue. Considering the B–P method, varying the incident compressive pulse would require different combinations of piston rod lengths and bullet masses increasing the workload during testing [138]. Additionally, varying the pulse duration would create multi–dimensional challenges in wave analysis due to the short piston rod lengths. The piston rod lengths reported by Overton [138, 139] varied from 2 to 11 cm in length. To achieve uniform pressure and displacement across the cross section of a bar, requires that the bar length be 4 times greater than its diameter (§ 3.2). Therefore, producing short duration pulses would require shorter piston lengths resulting in non–uniform pulses and increasing the complexity of wave analysis. It should be noted that Williams [109] reported a different process of varying the input of the B–P method by increasing static pressure above the fluid column; however, this process relates to the third limitation of the methods, which is the lack of a greater impedance boundary enclosing the fluid and will be discussed further below. Alternatively, the F–Hb method provides a simple solution of varying loading by use of differing striker types and geometry [143–148]. Due to the great length of the incident bar, the F–Hb method generates the incident pulse entirely within the bar before propagating into the fluid, whereas the B–P method generates the pulse in the fluid from successive pulses. Generating the pulse entirely within the bar provides time for the pulse to become uniform across the cross section of the bar effectively producing one–dimensional wave propagation.

Another disadvantage with the methods presented is the large fluid volume required for each test. The B–P and F–Hb methods used columns of fluid with a typical diameter of 25.4 mm and reported heights of at least 400 mm. The large height of the fluid column was used to ensure that the reflected wave produced at the free–surface would not overlap with the compressive pulse at the transducer locations [112, 138, 141]. The T–A method had the shortest fluid column height

reported of 200 mm with a diameter of 21 mm resulting in ~70 ml of fluid required, which for some fluids such as CSF would be challenging to obtain [131].

Lastly, the motivation for studying cavitation resulting from head blast exposure requires that similar boundary conditions be satisfied; specifically at the contre–coup where negative pressure is observed and cavitation may occur. Therefore, it is necessary to consider a boundary with greater acoustic impedance than the fluid (like cranial bones in relation with CSF) when measuring the cavitation pressure threshold from blast loading. Both the B–P and F–Hb methods have been developed such that a tensile pressure pulse is produced at an open fluid–atmosphere interface at the top of the fluid column (contre–coup). Additionally, if a solid boundary was added, the vertical orientation of the system would create challenges in ensuring that no entrapment of air occurs at the interface during filling. On the other hand, the T–A method provides a high impedance boundary at the base of the tube (contre–coup) by way of a rubber cylinder; however, the seal could harbor nucleation sites (§ 2.3) or result in air leakage during high magnitude insults, which would effectively reduce the measured cavitation pressure threshold.

Of the dynamic methods presented, the F–Hb was recognized as the least limited method as it provides a solution for the significant loading limitation recognized for both the T–A and B–P methods. The following section discusses a preliminary investigation into resolving the remaining two limitations of the F–Hb method: (1) requiring a large fluid volume, and (2) lacking a high impedance boundary enclosing the fluid.

3.1.6 Preliminary Investigation of Novel Dynamic Method

A preliminary investigation was performed by Singh et al. [95] to resolve the two remaining limitations recognized for the F–Hb method by use of a traditional Split Hopkinson Pressure Bar (SHPB) apparatus (§ 3.2) with a cylindrical confinement chamber. The apparatus consisted of cylindrical aluminum incident and transmitter bars, and a hollow striker tube replacing the traditional striker bar (Figure 18). Both the incident and transmitter bars were of 2438 mm in length and 24.5 mm in diameter, and the striker tube had a length of 37 mm and an external and internal diameter of 38.1 mm and 25.4 mm, respectively. The fluid was held inside an acrylic (Polymethyl methacrylate, PMMA) chamber tube placed around the incident and transmitter bar–

ends using rubber o–rings. The chamber had a length of 109 mm and an internal and external diameter of 26 mm and 88.9 mm, respectively; reducing the fluid volume required and resolved the first remaining limitation of the F–Hb method.

The striker tube was concentric with the incident bar and accelerated toward an aluminum anvil, affixed to the incident bar, by the use of bungee cords. Impact of the striker tube and anvil generated a tensile pulse (incident wave, $\sigma_{I(1)}$) that propagated down the incident bar, through the fluid in the chamber ($\sigma_{I(2)}$), and into the transmitter bar (σ_T) (Figure 19). Strain gauges mounted onto the midpoints of the incident and transmitter bars were used to measure the propagating pulses. The principle of constructive superposition was utilized in this apparatus by using the high impedance of the transmitter bar to produce a tensile reflection (reflected wave, σ_R) that, when superimposed with the trailing–end of the incident wave at the fluid–transmitter bar interface, generated cavitation (§ 3.2.1). Using the greater impedance of the transmitter bar compared with the water as a boundary resolved the last remaining limitation of the F–Hb method. Measurements of the fluid pressure changes were not taken directly; however, the upper bound negative pressure produced from the constructive superposition was calculated using SHPB theory equations (Equation 18 and Equation 19) (§ 3.2) using measured incident strain.

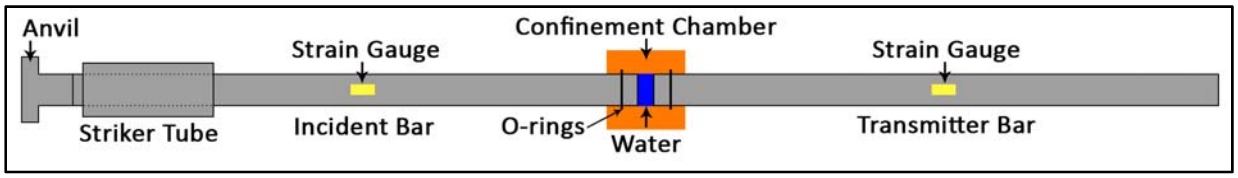

Figure 18. Traditional SHPB apparatus modified to generate tensile incident waves and confine fluid samples

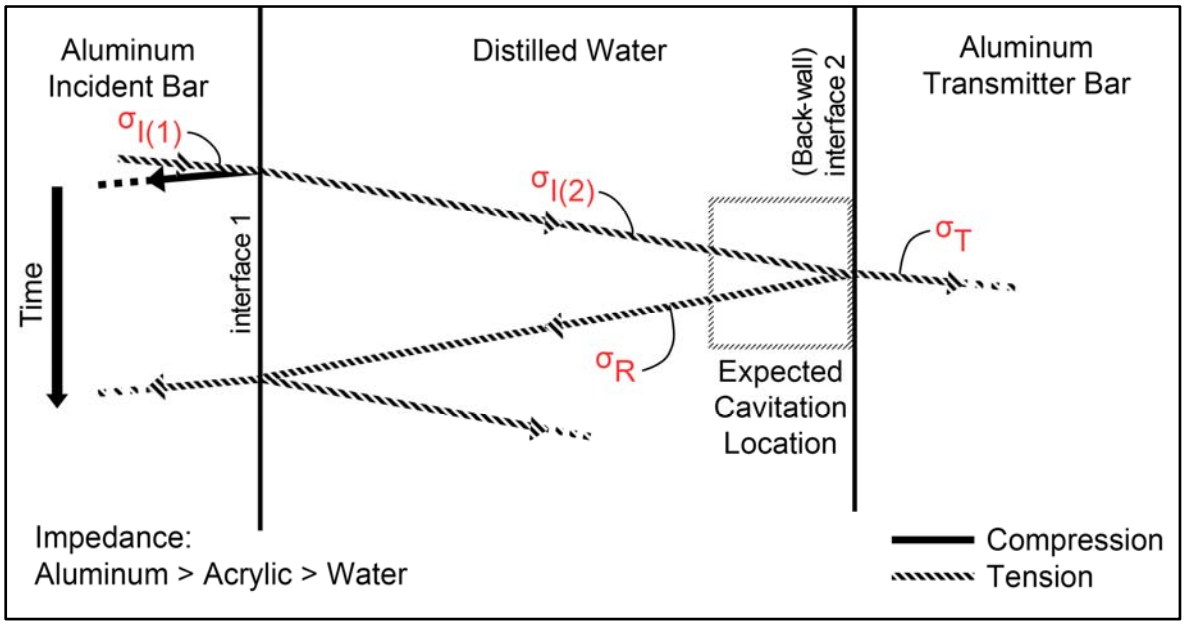

Figure 19. Wave propagation between the incident bar, transmitter bar, and confinement chamber containing distilled water

Singh performed a test with distilled water, and generated cavitation with a calculated upper bound negative pressure of 1.02 MPa using a tensile incident wave of 3.4 MPa (Figure 20). Although resolving the limitations of the F–Hb method, new limitations for this apparatus were recognized. (1) Cavitation was unavoidable; the bungee cords used to propel the striker required a minimum tension and was limited in that cavitation was generated for the minimum impact velocity. (2) The chamber seal was too compliant; the compliance of the o–rings used to hold the chamber onto the bars allowed air to leak into the chamber during tests yielding results indistinguishable between cavitating and non–cavitating events. (3) The lack of direct measurement and fluid pressure validation; the reported negative fluid pressure were calculated using SHPB theory equations that did not incorporate cavitating dynamics. For this reason, the calculated negative fluid pressure was considered as the upper bound of the experimental conditions; however, it was assumed that the water in the experiments due to the observed cavitation did not sustain such negative pressure. With the presented limitations, a cavitation pressure threshold could not be measured for distilled water using this apparatus. However, Singh demonstrated the efficacy of generating fluid cavitation using a traditional SHPB with the addition of a confinement chamber. The apparatus used in this preliminary investigation was considered as

the Tensile Split Hopkinson Pressure Bar (T–SHPB–1) and was the first iteration of the final apparatus presented in this thesis. Prior to presenting the design and development of the final apparatus, some background information will be discussed relating to the traditional SHPB apparatus (§ 3.2) and the experimental diagnostics used in the development of the final apparatus (§ 3.3).

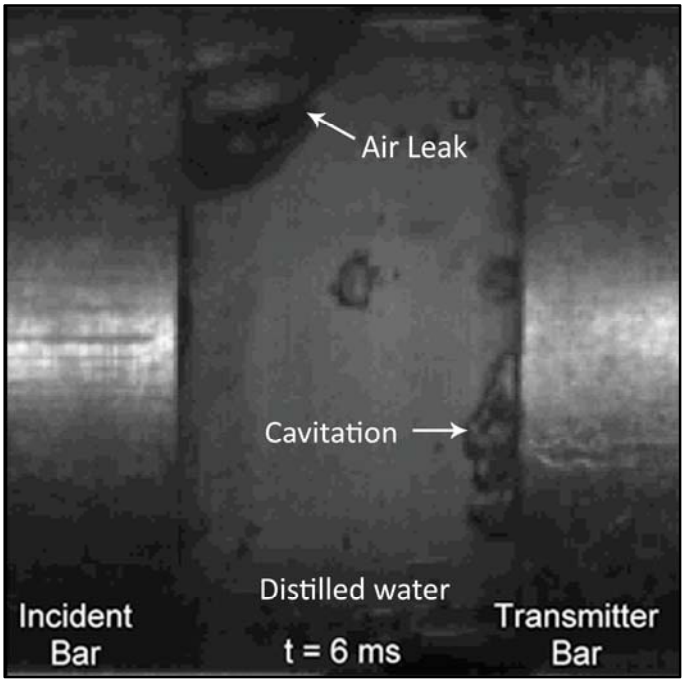

Figure 20. Cavitation generated in distilled water using the traditional SHPB apparatus

3.2 Review of Traditional SHPB Theory

The SHPB apparatus is a prominent technique for testing materials that require high strain–rate and high deformations such as in the field of blast exposure. A two bar system having the same diameter and material with a cylindrical sample between the two bars (Figure 21) was initially developed by Kolsky in 1948 and is commonly known as the SHPB but also known as the Kolsky Bar [149, 150]. In Kolsky's setup, a cylindrical condenser microphone was used on the incident bar, instead of strain gauges, to determine the amplitude of the pressure pulses propagating in the incident bar. A condenser microphone was also used on the end of the transmitter bar to determine the displacement of its free–end, which was used to calculate the pressures occurring in the sample. A detonation was used to produce a pressure pulse in the incident bar, which would

later be replaced with a striker bar of the same material and diameter as the incident and transmitter bars. An anvil bar made of a harder material than the incident bar was placed between the detonation and incident bar in order to protect the incident bar from damage.

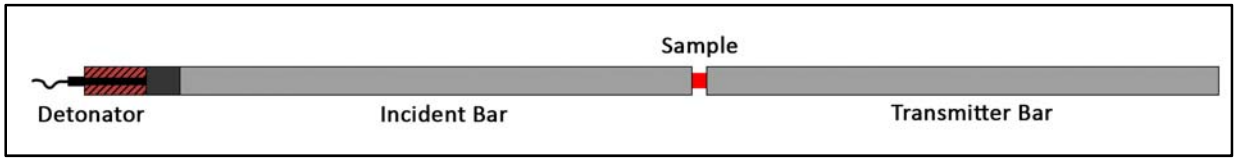

Figure 21. Kolsky bar apparatus schematic

The SHPB works on the basic principle of wave propagation. The traditional SHPB consists of metallic bars impacted by a striker bar to generate an elastic pressure pulse. After impact of the striker on the incident bar, an elastic pulse propagates down the incident bar, through the sample, and into the transmitter bar. The elastic pulse propagation velocity is dependent on the material properties of the bars whereas the pulse amplitude also depends on the striker impact velocity. The pulse travels at a specific velocity known as the wave speed (C_o). In an elastic SHPB the elastic wave speed is dependent on the bar material density (ρ_{bar}) and elastic modulus (E_{bar}), and can be calculated by [150, 151]:

$$C_o = \sqrt{\frac{E_{bar}}{\rho_{bar}}} \qquad \text{Equation 8}$$

The pulse produced in the incident bar is known as the incident wave and has a period or duration (T) that is twice the time required for one transit of the striker bar length (L), calculated by:

$$T = \frac{2L}{C_o} \qquad \text{Equation 9}$$

The duration of the incident wave corresponds to the compressive pulse, produced at the impact interface, propagating to the free–end of the striker bar, and back towards the impact interface as a tensile pulse. Upon reaching the interface, the bars separate and force is no longer applied to the incident bar. The stress amplitude of the incident wave (σ_I) can be related to the striker impact velocity (V_s) by:

$$\sigma_I = \frac{1}{2}\rho_{bar} C_o V_s \qquad \text{Equation 10}$$

When the incident wave (ε_I) reaches the sample, a portion of the wave is reflected back towards the striker–end (reflected wave, ε_R), and the balance of the wave is transmitted through the sample and into the transmitter bar (transmitted wave, ε_T). Therefore, ideally, the sum of the transmitted and reflected wave magnitudes is equal to the incident wave given by:

$$\varepsilon_I = \varepsilon_T - \varepsilon_R \qquad \text{Equation 11}$$

where the negative sign addresses the opposite sense of the reflected wave (§ 3.2.1). The strain of the test sample is calculated using velocities of the incident and transmitter bar interfaces in contact with the sample. The interface velocities of the incident (V_I) and transmitter (V_T) bars can be calculated using their respective strains measured at the strain gauge stations:

$$V_I = C_o(\varepsilon_I - \varepsilon_R) \qquad \text{Equation 12}$$

$$V_T = C_o \varepsilon_T \qquad \text{Equation 13}$$

Combining the equations above, and using the definition of strain–rate as the difference in interface velocities over the original sample length (L_{so}), results in a sample with the strain–rate ($\dot{\varepsilon}_s$) and strain (ε_s) given by:

$$\dot{\varepsilon}_s(t) = \frac{C_o}{L_{so}}(\varepsilon_I - \varepsilon_T - \varepsilon_R) \qquad \text{Equation 14}$$

$$\varepsilon_s = -\frac{2C_o}{L_{so}} \int_0^t \varepsilon_R dt \qquad \text{Equation 15}$$

The stress occurring in the sample can be obtained knowing the elastic property of the bars and the dimensions of the sample. The stress occurring in the sample (σ_s) is the sum of the stresses applied as a result of the two bars (Equation 16); where σ_T is the stress amplitude of the transmitted wave. It can be expanded by relating the stresses with the strains due to the elastic property of the bars, and using the cross sectional area of the bars (A_{bar}) and sample (A_s):

$$\sigma_s = \sigma_I + \sigma_T \quad \text{Equation 16}$$

$$\sigma_s = \frac{A_{bar}E_{bar}}{2A_s}(\varepsilon_I + \varepsilon_T + \varepsilon_R) \quad \text{Equation 17}$$

The analysis presented above are intended for an elastic SHPB apparatus and make the four assumptions described by Davies [152]: (1) the bars must remain elastic through the entire test; (2) no attenuation or dispersion of the waves should occur; (3) the waves are uniform throughout the cross section of the bar; and (4) the sample must remain in equilibrium throughout the test. Assumption 1 requires that elastic bars are used and their yield strengths are not exceeded. Assumption 2 requires that the measured data collected at the bar mid–points (typical location of strain gauges) are also valid at their interfaces after propagation. Assumption 3 requires that the pressure and displacement across the cross section of the bars are uniform such that, the one–dimensional wave equations used in the analysis are valid. Davies suggests the incident wave wavelength be longer than the bar lengths to avoid distortion, and the bar lengths be at least 4 times greater than its diameter to produce a uniformly distributed wave [152]. The first 3 assumptions can be easily satisfied using long metallic bars. Assumption 4 requires that the forces at the incident bar–sample and transmitter bar–sample interfaces are equal over time. Davies suggest that 3–5 wave reflections occur within the sample over the rise time of the incident wave to produce equilibrium in the sample [152].

3.2.1 Wave reflection and Impedance

Waves travelling throughout the bars of the SHPB apparatus are the result of acoustic flow of pressure generated by the impact of the striker with the incident bar. The pressure travels throughout the bars perpendicular to the source as a result of displaced atoms displacing their neighboring atoms (Figure 22). The pressure wave travels at the acoustic wave speed of the bar material, and in elastic waves, travels at an acoustic wave speed that can be calculated using Equation 8.

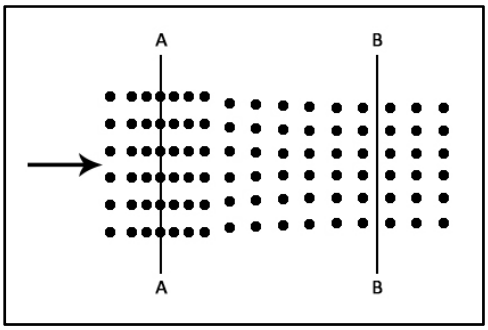

Figure 22. Compressive pressure wave propagation from A to B resulting in atomic displacement

An important principle in adjusting and predicting wave propagation characteristics is acoustic impedance. The acoustic impedance of a material is the resistance of that material with respect to acoustic pressure flow and can be calculated by multiplying its density (ρ) and acoustic wave speed (C_o). Modifying the bar impedances in the SHPB allows the user to adjust the amplitudes and senses of the propagating waves. For an ideal one–dimensional wave propagation in cylindrical bars, where the interface between material 1 and material 2 are perpendicular to the incident wave path, an incident wave from material 1 entering material 2 produces reflected and transmitted waves that can be calculated using:

$$\frac{\sigma_{reflected}}{\sigma_{incident}} = \frac{(\rho * C_o)_{material2} - (\rho * C_o)_{material1}}{(\rho * C_o)_{material1} + (\rho * C_o)_{material2}} \qquad \text{Equation 18}$$

$$\frac{\sigma_{transmitted}}{\sigma_{incident}} = \frac{2 * (\rho * C_o)_{material2}}{(\rho * C_o)_{material1} + (\rho * C_o)_{material2}} \qquad \text{Equation 19}$$

Equation 18 demonstrates how the sense of the reflected wave can be changed through the principles of impedance differences. An incident wave entering a lower impedance material from a higher impedance material reflects as the opposite sense, and an incident wave entering a higher impedance material from a lower impedance material reflects in the same sense (Figure 23). This is evident when a compressive pulse is applied to one end of an aluminum bar with its surfaces exposed to the atmosphere. The compressive pulse propagates towards the opposite bar–end, displacing the bar–end forward, and reflecting as a tensile pulse as a result of the lesser impedance of the air compared to the aluminum. This tensile pulse then travels towards the impacted end, displacing it forward, and reflecting back as a compressive pulse as a result of the same impedance

difference with the air. The sequence of reflections at both ends of the bar drives the bar forward at a speed limited by the acoustic velocity of aluminum and length of the bar. The opposite would be seen if the non–impacted end of the bar was in contact with a steel bar of the same diameter. The compressive pulse would reflect at the contact interface in the same sense, due to the lesser impedance of the aluminum compared with the steel and effectively cause the aluminum bar to rebound away from the steel bar.

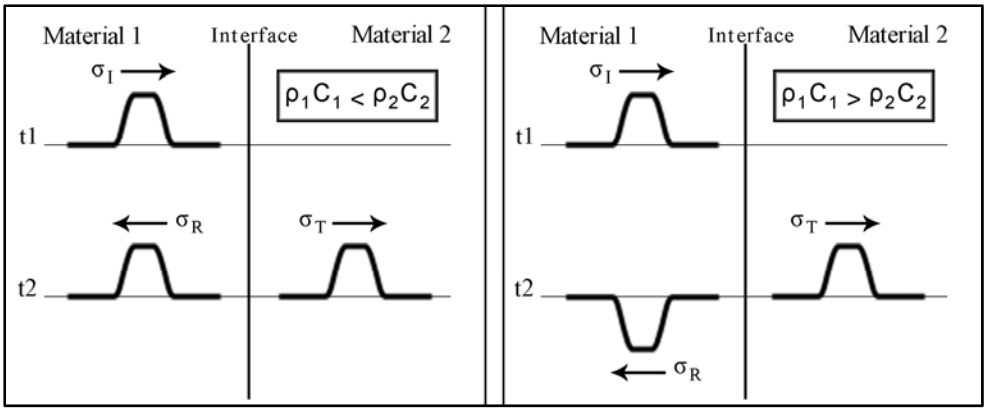

Figure 23. Effect of impedances difference between two materials on the reflected and transmitted waves

3.2.2 Wave Attenuation and Dispersion

A traditional SHPB apparatus used for material testing often utilizes metallic bars that are elastic throughout the impact to simplify analysis and interpretation of the data. As previously discussed, Davies suggested that uniform one–dimensional elastic waves with negligible dispersion or attenuation should be generated. Dispersion and attenuation relates to the duration increase and amplitude decrease of a wave as it propagates through a material, respectively (Figure 24). Generally, dispersion and attenuation occur together and are the result of material and geometric properties. Dispersion and attenuation can be observed in polymeric SHPB systems that use viscoelastic polymeric bars. Polymeric SHPB apparatuses are often used for testing softer materials such as foams and biomaterials due to better impedance matching and longer rise times compared to metallic bars.

Examples of recorded incident bar strains for elastic and viscoelastic bars with free–end conditions are compared to demonstrate the effects of the attenuation and dispersion (Figure 25).

In the viscoelastic bar, the reflected wave decreases in magnitude and changes in shape, whereas in the elastic bar the changes of the rectangular waves are negligible. The presence of attenuation and dispersion make analysis of the loading more challenging as the waves measured from the strain gauges must be attenuated to the bar–sample interfaces before Equation 12 and Equation 13 can be valid. Analysis of wave propagation in a polymeric SHPB apparatus requires deconstruction of the wave into its components. In a non–dispersive system, such as in an elastic material, each component of the wave travels at the same velocity and their peaks remain at the same distance relative from one another during propagation, resulting in an unchanged overall elastic wave shape. In a dispersive system, such as in a viscoelastic material, each component has different velocities and changing phase shift. Therefore, the relative distances of the peaks also change, resulting in a change in overall viscoelastic wave shape.

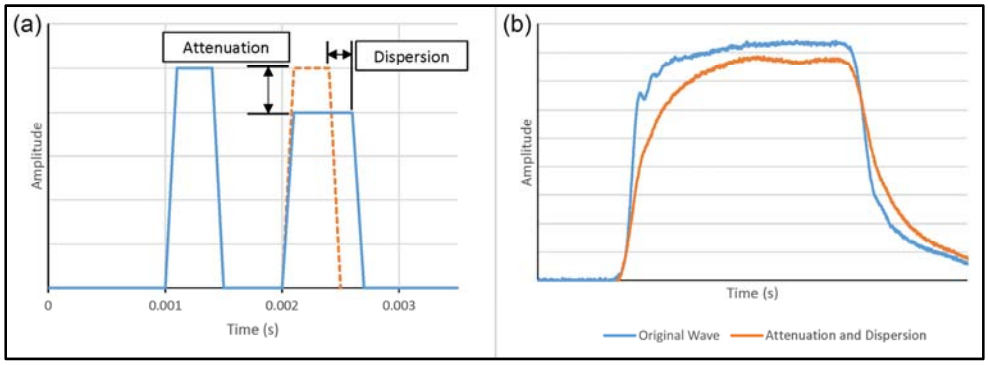

Figure 24. (a) Effect of attenuation and dispersion on amplitude and duration, respectively; (b) Attenuation and dispersion on measured data

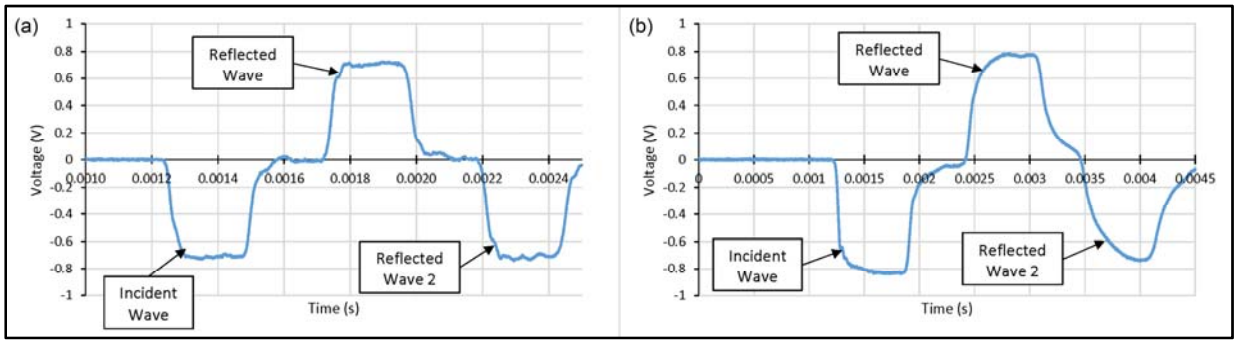

Figure 25. (a) Elastic aluminum incident bar signal with free–end conditions; (b) Viscoelastic acrylic incident bar signal with free–end conditions

The key to analyzing dispersion and attenuation is to separate the wave of interest into its components. A Fourier series can be used to represent a complex periodic wave through the sum of simple sinusoidal functions of harmonically related frequencies [153]:

$$f(t) = a_0 + \sum_{k=1}^{\infty} (a_k \cos(k\omega_0 t) + b_k \sin(k\omega_0 t)) \qquad \text{Equation 20}$$

where $\omega_0 = \frac{2\pi}{T}$ is called the fundamental frequency, and a_0, a_k, and b_k are coefficients related to amplitude. A periodic rectangular wave can be constructed through the summation of cosine waves such that accuracy of replication increases with increased cosine terms, where the individual cosine waves are identified as the components of the rectangular wave (Figure 26a–c). The amplitude and phase angle of each component of the wave in both the time and frequency domain are important for wave characterization (Figure 26d–e). For aperiodic waves, such as those measured from a SHPB test, a Fourier transform pair exists in which the signal in the time domain can be transformed into the frequency domain and back. The Fourier transform for transforming an aperiodic function in the time domain ($f(t)$) into the frequency domain ($F(i\omega_0)$) is given by:

$$F(i\omega_0) = \int_{-\infty}^{\infty} f(t) e^{-i\omega_0 t}\, dt \qquad \text{Equation 21}$$

whereas the inverse Fourier transform for transoforming the function in the frequency domain into the time domain is given by:

$$f(t) = \frac{1}{2\pi} \int_{-\infty}^{\infty} F(i\omega_0) e^{i\omega_0 t}\, d\omega_0 \qquad \text{Equation 22}$$

The infinite limits represent the infinite period of an aperiodic signal in that it never repeats. However, the wave function $f(t)$ is often unknown, and instead, a discretized signal is measured. For such a case, the Discrete Fourier Transform (DFT) pair exists in which a signal in the time domain divided into *N* equally spaced samples (f_n) can be transform into the frequency domain using (F_k):

$$F_k = \sum_{n=0}^{N-1} f_n e^{-ik\omega_0 n} \quad for\ k = 0\ to\ N-1 \qquad \text{Equation 23}$$

and back into the time domain using the inverse DFT:

$$f_n = \frac{1}{N} \sum_{k=0}^{N-1} F_k e^{ik\omega_0 n} \quad for\ n = 0\ to\ N-1 \qquad \text{Equation 24}$$

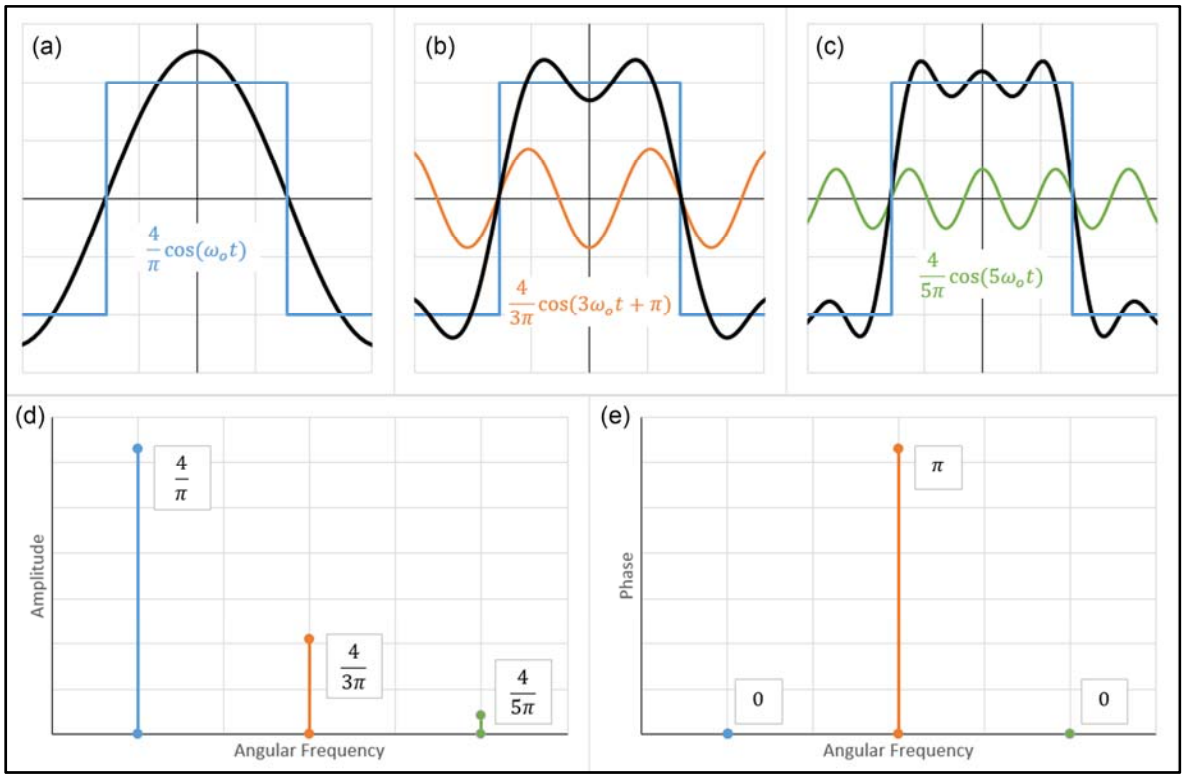

Figure 26. (a–c) Addition of cosine terms to previous approximations (black) resulting in a better approximation of the rectangular wave; (d–e) Amplitude and phase angle versus angular frequency waves for the cosine terms in (a–c)

The calculation of DFT requires N^2 operations and can become computationally intensive in large sample signals. A Fast Fourier Transform (FFT) algorithm was developed to compute DFT in fewer operations by exploiting the periodicity and symmetry of trigonometric functions resulting in approximately $Nlog_2N$ operations. Many different FFT algorithms exist each having similar approaches of decomposing the DFT into successively smaller DFTs. For example,

Equation 23 with *N* samples (points) can be divided into two (*N/2*)–points such that two DFTs are performed, resulting in the reduction of operations to $2*(N/2)^2$. If each half were halved again, and continues such that *N/2* two–point DFTs were performed, the operations for the entire computation is reduced to approximately $Nlog_2N$.

To determine the dispersion and attenuation of a propagating linearly viscoelastic wave, the general solution for the one–dimensional wave equation must first be written in the frequency domain starting with the stress and strain relationship:

$$\frac{\partial^2}{\partial x^2}\tilde{\sigma}(x,\omega) = -\rho_{bar}\omega^2\tilde{\varepsilon}(x,\omega) \qquad \text{Equation 25}$$

where the stress and strain for a linearly viscoelastic material are related by:

$$\tilde{\sigma}(x,\omega) = E^*(\omega)\tilde{\varepsilon}(x,\omega) \qquad \text{Equation 26}$$

where E^* is the complex modulus and can be related to the propagation coefficient function (γ) by:

$$\gamma^2 = -\frac{\rho_{bar}\omega^2}{E^*} \qquad \text{Equation 27}$$

Combining Equation 25, Equation 26, and Equation 27 in terms of strain results in:

$$\frac{\partial^2\tilde{\varepsilon}(x,\omega)}{\partial x^2} - \gamma^2\tilde{\varepsilon}(x,\omega) = 0 \qquad \text{Equation 28}$$

with a general solution of:

$$\tilde{\varepsilon}(x,\omega) = \tilde{P}(\omega)e^{-\gamma x} + \tilde{N}(\omega)e^{\gamma x} \qquad \text{Equation 29}$$

which is similar to that of the general solution for the one–dimensional wave equation but in the frequency domain. $\tilde{P}(\omega)$ and $\tilde{N}(\omega)$ are the Fourier transforms of the strains at *x=0* as the result of waves travelling in increasing and decreasing *x* direction, respectively. The propagation coefficient function is related to the attenuation coefficient (α) and phase velocity (c) by:

$$\gamma(\omega) = \alpha(\omega) + i\frac{\omega}{c(\omega)} \qquad \text{Equation 30}$$

Therefore the one–dimensional strain wave measured in a system in the time domain can be propagated a distance by transforming it into the frequency domain and correcting for attenuation and dispersion using the propagation coefficient of that system.

The propagation coefficient of a viscoelastic bar in a polymeric SHPB system can be obtained by performing a test with the non–impacted end of the bar having a free–end condition and mounting a strain gage at a known distance (*d*) from the free–end large enough to ensure that overlap of the incident and reflected waves does not occur. The normal force ($\tilde{F}$) in the frequency domain at any given point on the bar is then given by:

$$\tilde{F}(x,\omega) = -\frac{\rho_{bar}A_{bar}\omega^2}{\gamma^2}\left[\tilde{P}(\omega)e^{-\gamma x} + \tilde{N}(\omega)e^{\gamma x}\right] \qquad \text{Equation 31}$$

At the free–end, the force must be become zero resulting in the above equation reducing to:

$$\tilde{P}e^{-\gamma x} + \tilde{N}e^{\gamma x} = 0 \qquad \text{Equation 32}$$

where the incident and reflected strains are related by:

$$\tilde{\varepsilon}_I = \tilde{P} \text{ and } \tilde{\varepsilon}_R = \tilde{N}$$

The one–dimensional wave displacement in the time domain can be transformed into the frequency domain by:

$$u(x,t) \rightarrow \tilde{u}(x,\omega) = \sum F_n G(k_{mn}x)e^{i\omega_n t} \qquad \text{Equation 33}$$

where F_n is the amplitude spectra and G is the transfer function that determines the amount of phase shift and attenuation with respect to the space domain [154]. The transfer function can be obtained at the free–end by:

$$G(\omega) = -\frac{\tilde{\varepsilon}_R(\omega)}{\tilde{\varepsilon}_I(\omega)} e^{-\gamma 2d} \quad \text{Equation 34}$$

where the negative is used to compensate for the sense of the reflected wave. The transfer function can be turned into its rectangular form at a given frequency to show the relationship between the amplitudes (r_I, r_R) and phase shift (θ_I, θ_R) of the incident and reflected waves with a propagation distance of *2d* resulting in:

$$G = \frac{r_R}{r_I} e^{i(\theta_R - \theta_I)} = e^{-\gamma 2d} = e^{-(\alpha + ki)2d} \quad \text{Equation 35}$$

By equating the real and imaginary parts of the transfer function, the attenuation coefficient (α) and phase velocity (k) can be obtained for a given frequency by:

$$\alpha = -\frac{\ln\left(\frac{r_R}{r_I}\right)}{2d} \quad \text{Equation 36}$$

$$k = \frac{\omega}{c} = -\frac{(\theta_R - \theta_I)}{2d} \quad \text{Equation 37}$$

This process is repeated for each frequency of a specified range to obtain the propagation coefficient function for that range. Therefore measured a strain wave obtained from a polymeric SHPB apparatus can be transformed into the frequency domain, propagated a distance using the propagation coefficient, and then transformed back into the time domain, resulting in a propagated strain wave corrected for dispersion and attenuation. A program was developed by Salisbury [155–159] that uses the principles of spectral analysis described above to propagate measured strain data from a polymer SHPB system (§3.3.5). The software was validated and used in published works, and was used for data processing of the strain signals measured in the final apparatus presented in this thesis.

3.3 Review of Experimental Diagnostics for Dynamic Cavitation Testing

This section discusses background information relating to the principal diagnostic equipment used in the design and development of the final apparatus presented in this thesis. Such

diagnostics used for experimental measurements were strain gauges used for measuring strain wave propagation (§ 3.3.1), and a frame–by–frame tracking program (§ 3.3.2) and Photon Doppler Velocimeter (§ 3.3.4) used for measuring velocities. Additional diagnostics used were a spectral analysis program for processing strain measurements (§ 3.3.5), a cross–correlation analysis program for validating measurements (§ 3.3.6), and finite element modelling software for verifying dynamics (§3.3.7).

3.3.1 Strain Gauges

Strain gauges are sensors that are mounted onto objects and used to detect and measure force–related parameters of that object. There are two common types of strain gauges made from either foil or semiconductor material. The main advantages of foil gauges over semiconductor gauges are that they are less expensive and have backing that allows for easier application onto materials. Due to their lack of backing, special care is required when adhering semiconductor gauges onto materials that conduct electricity. For a uniaxial foil strain gauge, strain is measured in a single direction by the metallic foil arranged in a grid pattern (Figure 27a). The length of the active grid increases the amount of foil subjected to strain increasing its change in resistance and output signal [160]. Care must be taken in choosing the active grid length since increasing the active grid length also increases the averaging of the strain measured (Figure 28) [155, 161]. The active strain gauge length must be shorter than the shortest duration of the pulse of interest to reduce averaging error. More complex multi–directional strain gauges can also be used for materials that require detection of forces acting in multiple directions (Figure 27b).

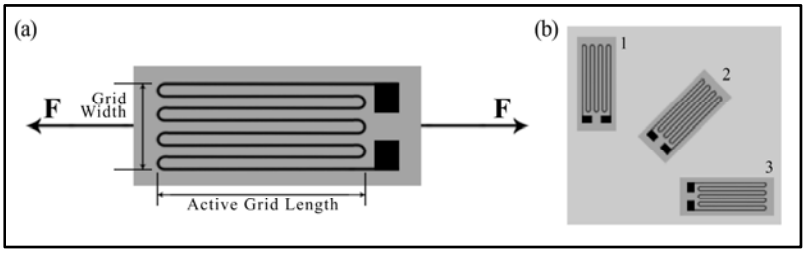

Figure 27. (a) Uniaxial foil strain gauge; (b) Multiaxial foil strain gauge

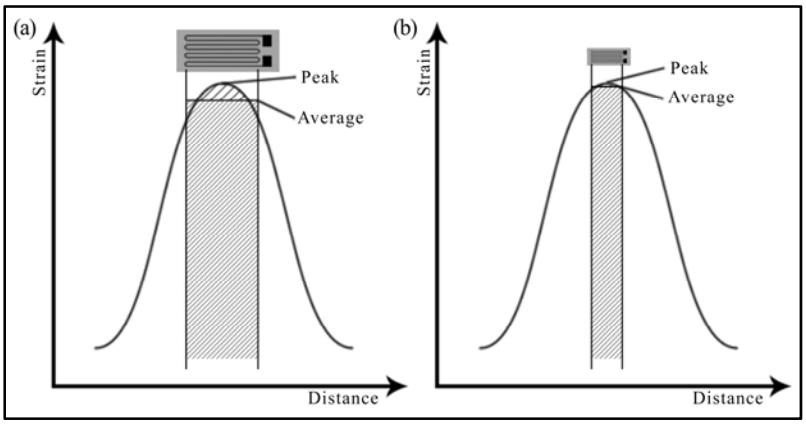

Figure 28. Averaging effect on peak strain measurement as a result of strain gauge size

The relationship between the strain of the gauge (ε), its original resistance (R), and its change in resistance (ΔR) is known as the gauge factor (GF):

$$\frac{\Delta R}{R} = (GF) * \varepsilon \qquad \text{Equation 38}$$

The gauge factor is the sensitivity of the gauge that relates the change in resistance to the change in strain. For metallic foil strain gauges, the gauge factor is typically around 2.0 and is normally calibrated and supplied by the manufacturer along with the gauges [160]. A disadvantage of foil gauges is their low gauge factor and requirement of voltage output amplification, whereas semiconductor gauges have a gauge factor of approximately 150 allowing for greater resolution and a greater signal–to–noise ratio. Care must be taken during the mounting process of a gauge to ensure that the strain in the material is accurately transferred to the gauge. The mounting process can affect the ability of the gauge to strain producing an effective gauge factor different from the calibrated gauge factor. To circumvent the effects of the mounting process, the system should be calibrated after mounting to determine the effective strain gauge factor.

3.3.1.1 Wheatstone bridge

A common circuit to measure the change in resistance of a uniaxial strain gauge is the Wheatstone bridge (Figure 29a). The Wheatstone bridge has a configuration of four resistor arms (R_1, R_2, R_3, R_4) with an excitation voltage (V_{ex}) applied across the opposite corners of the configuration, and the resultant voltage output (V) is measured across the other opposite corners.

Applying Kirchoff's Voltage Law and Ohm's Law to the Wheatstone bridge results in the voltage output:

$$V = V_{DB} = V_{BA} - V_{AD} = \left(\frac{R_1R_3 - R_4R_2}{(R_1 + R_2)(R_3 + R_4)}\right)V_{ex} \qquad \text{Equation 39}$$

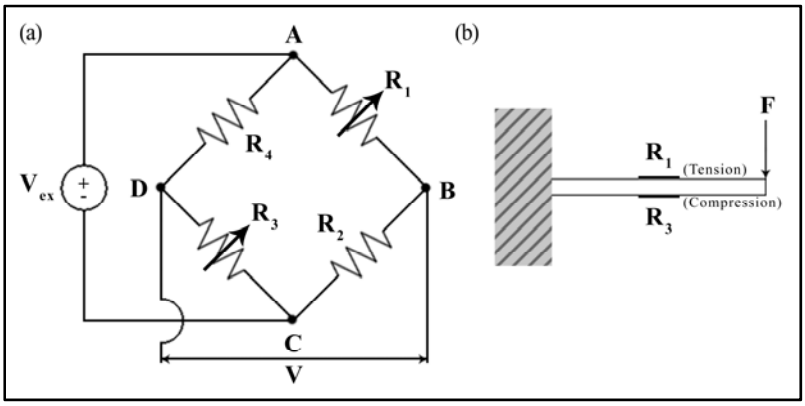

Figure 29. (a) Wheatstone half–bridge configuration; (b) Strain gauge placement to eliminate bending with Wheatstone half–bridge

It can be seen that if $\frac{R_1}{R_2} = \frac{R_4}{R_3}$, the bridge is balanced, and the voltage output will be zero regardless whether $R_1 = R_4$ or $R_2 = R_3$. For simplicity, and in the case for the bars in a SHPB apparatus, two resistors opposite from each other (R_1, R_3) are replaced with uniaxial strain gauges with equal resistances, and the other two resistors (R_2, R_4), considered as 'dummy' resistors, are chosen to match the unstrained strain gauge resistances $(R_1 = R_3 = R_2 = R_4)$. This configuration is called a Wheatstone half–bridge and is advantageous because it reduces strain as a result of bending when the strain gauges are mounted at opposite sides of the bar diameter (Figure 29b). Substituting Equation 38 into Equation 39 for this bridge type results in the voltage output for pure uniaxial and pure bending stresses, respectively:

$$V = V_{DB} = \left(\frac{GF\varepsilon}{2 + GF\varepsilon}\right)V_{ex} \qquad \text{Equation 40}$$

$$V_{bending} = \left(\frac{-\left(GF\varepsilon_{bending}\right)^2}{\left(4 - GF\varepsilon_{bending}\right)^2} \right) V_{ex} \qquad \text{Equation 41}$$

where Equation 40 and Equation 41 are a simplified equations neglecting the changes in strain of the gauges as a result of temperature, and changes in resistance of the lead wires used for the bridge. The elimination of bending is demonstrated with Equation 41 for a pure bending scenario where the dominating term is $\varepsilon_{bending}^2$ in the numerator resulting in a very small voltage output ($V_{bending}$). Therefore the bending voltage output becomes negligible compared to the uniaxial voltage output (V), especially when the expected strain from bending is also very small.

In application, the temperature of the gauges and the lead wires used in the bridge can also affect the resultant voltage output. The increase of temperature in the gauge can cause thermal expansion resulting in a thermal voltage output measurement unrelated to the test, and the use of long lead wires for the gauges can introduce non–negligible resistances to the bridge. Incorporating both the temperature ($\Delta R_{T1}, \Delta R_{T2}$) and lead wire ($RI_1, RI_3$) effects (Figure 30) with the assumptions that the effects of temperature and the lead wires on the gauges are equal, respectively ($\Delta R_{T1} = \Delta R_{T3} = \Delta R_T$ and $RI_1 = RI_3 = RI$), results in the resultant uniaxial strain voltage output:

$$V = \left(\frac{GF\varepsilon + \frac{\Delta R_T + RI}{R}}{2 + GF\varepsilon + \frac{\Delta R_T + RI}{R}} \right) V_{ex} \qquad \text{Equation 42}$$

It can be seen that if the effects of temperature and the lead wires are neglected, Equation 42 equals Equation 40. If bending is not expected during the experimental tests, a Wheatstone quarter–bridge can be used where only one resistor is replaced with a uniaxial strain gauge, and the other 3 are replaced with matching resistance ‘dummy’ resistors. This configuration results in the uniaxial voltage outputs neglecting, and incorporating, temperature and lead wire effects given by:

$$V = \left(\frac{GF\varepsilon}{2(2 + GF\varepsilon)} \right) V_{ex} \qquad \text{Equation 43}$$

$$V = \left(\frac{GF\varepsilon + \frac{\Delta R_T + RI}{R}}{2\left(2 + GF\varepsilon + \frac{\Delta R_T + 2RI}{R}\right)} \right) V_{ex} \qquad \text{Equation 44}$$

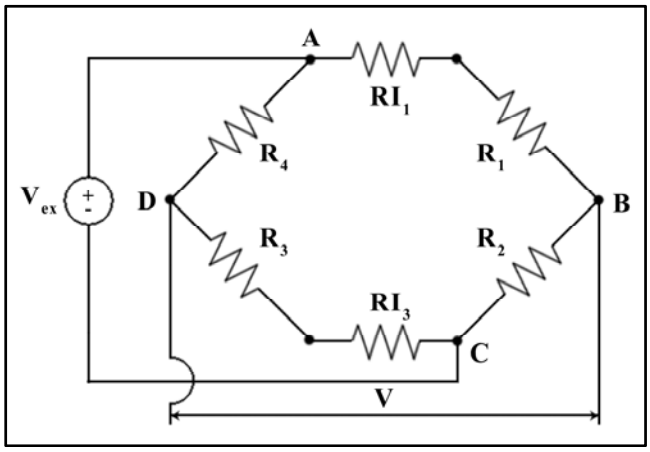

Figure 30. Wheatstone bridge with lead wires

3.3.2 Pressure Transducers

Pressure is a distributed force (*F*) applied perpendicular to a surface (*A*) and can be calculated by:

$$P = \frac{F}{A} \qquad \text{Equation 45}$$

Pressure can be measured in static or dynamic conditions. In the case of a static condition, such as a gas–filled balloon, the gas pressure is in equilibrium throughout the surface of the balloon with negligible change in pressure with respect to time. On the other hand, in a dynamic condition such as a water hose, measurement of pressure is dependent on the surface used due to the bulk motion of the fluid. For a fluid in motion, the pressure can be measured in two perpendicular directions resulting in the dynamic and static pressures. The dynamic and static fluid pressures are measured perpendicular and parallel to the fluid motion, respectively, and the sum of both pressures is known as the stagnation pressure (Figure 31). Dynamic pressure is also observed in fluids without bulk motion experiencing dynamic pressure changes through pressure wave propagation. With wave propagation, the dynamic and static pressures are measured perpendicular and parallel to the wave path, respectively. Care must be taken when measuring pressure of a motionless fluid in the

perpendicular direction of a propagating pressure wave because the signal measured is the superposition of the incident wave and reflected wave generated at the transducer diaphragm (§ 1.1.1).

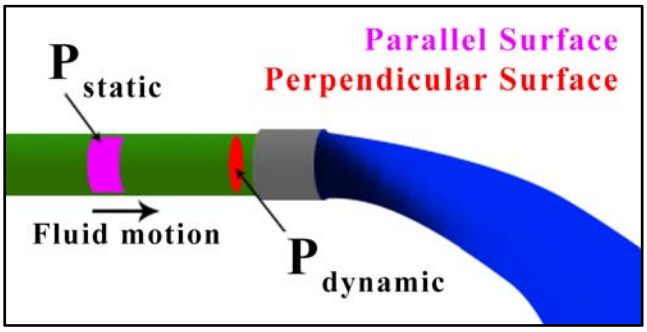

Figure 31. Parallel and perpendicular surfaces used to measure static and dynamic pressure, respectively, of a fluid in motion

Two common types of fluid pressure sensors for high–performance dynamic applications are the piezoelectric and piezoresistive strain gauge pressure sensors. Piezoelectric sensors convert stress into electric potential and *vice versa*, therefore they can measure pressure waves and generate pressure waves. They consist of metallized quartz or ceramic materials that accumulate electric charge (internal polarization) in response to mechanical stress. However, charge leakage occurs during stressing of the elements resulting in a decreasing signal when measuring static non–dynamic pressures. Piezoresistive strain gauge sensors commonly consist of silicon films and have the same principle as strain gauges in that their resistance changes in response to mechanical stress. Similar to foil strain gauges (§ 3.3.1), a Wheatstone bridge can be used to increase the sensitivity of the measurement. Consequently, piezoresistive sensors require an external excitation voltage whereas piezoelectric sensors do not. With both sensors, a diaphragm is used to transfer forces and separate the sensor from the fluid. An advantage of piezoelectric sensors over piezoresistive sensors is that they are more robust. Piezoelectric sensors are stable at higher temperatures, have a higher natural frequency, and are linear over a wider amplitude range. In general, implementation of transducers using piezoresistive sensors have the advantages of being less expensive and having smaller dimension capabilities allowing for reduced interference as a result of its implementation in fluid systems.

3.3.3 Frame–by–frame Tracking Program

A video analysis program (Tracker, Douglas Brown, http://physlets.org/tracker/) tracks the position of a feature of interest (FOI) in high–speed imaging to determine changes in position, velocity, and acceleration [162]. The program includes an Autotracker feature that can automatically track an FOI without the need to check each frame manually. Autotracking starts by selecting a template image of the FOI in the initial frame and a specified search boundary in which the program should search. Choosing a boundary reduces the computational burden by limiting the number of pixels the program must process. For each frame, an area the same size as the template is selected from within the boundary and compared to the template. A match score between each pixel of the selected area and template are calculated, which is inversely proportional to the sum of the squares of the RGB differences (Red, Green, and Blue color model values). In general, a low RGB difference results in a high match score. This is repeated until all pixels within the boundary are scored. The area with the greatest score within the boundary yields a pixel–position (PP), which is then further compared with adjacent area scores. A sub–pixel–position (SPP) is obtained by interpolating the PP with adjacent positions having the greatest scores.

The SPP score is then compared to an automark–value before automatically marking the FOI position in the frame. An automark–value set by the user is used as a benchmark to automatically accept SPP scores and maintain automation. When the SPP score is equal or greater than the set automark–value, a marker is placed at the SPP in the frame. In the event that the SPP score is lesser than the automark–value, the program prompts manual confirmation to place the marker at the SPP or the user to manually mark the frame. In general, the automark–value controls the automation by accepting or rejecting the SPP scores.

The template for the next frame is then generated using an evolution rate percentage set by the user that adapts the shape and color of the template over time to compensate for visual changes in the video during filming. The new template, for the next frame, is generated by overlaying the marked SPP image overtop of the current template with an opacity percentage equal to the evolution rate. For the greatest accuracy in autotracking, a still–framed and high–contrast video without excessive visual distortion is required, and the lowest setting for the evolution rate (0%) and greatest automark–value (10) should be used. Lastly, the boundary is moved towards the

marked SPP for the next frame, and the process repeats until all frames are marked or the user interrupts the automation. Figure 32 shows a general flowchart of the process of autotracking.

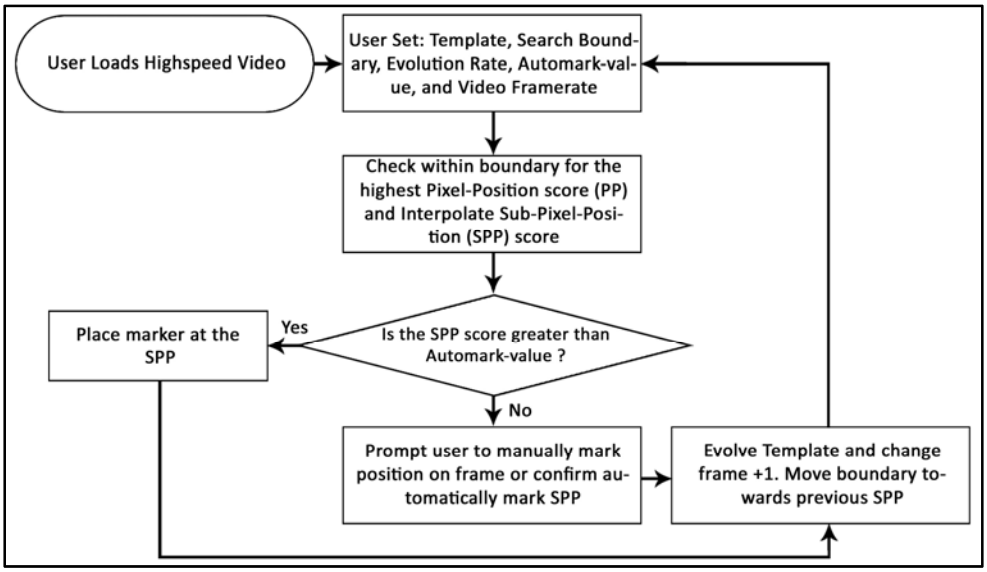

Figure 32. Flow chart of autotracking process of FOIs in high–speed imaging

3.3.4 Photon Doppler Velocimeter

The Photon Doppler Velocimeter (PDV) was introduced by Strand et al. [163, 164] as a diagnostic for measuring velocity data in high–speed experimental applications. The main principle of PDV analysis is determining the velocity of a moving surface using the frequency difference of mixed laser light signals called the beat frequency. Optical fibers are used to direct laser light through a probe onto a moving surface of interest, and at the same time, the probe collects light reflected from the moving surface and sends it back to a detector. The collected light becomes Doppler–shifted as a result of the moving surface, and its combination with un–shifted light produces a beat signal at the detector (Figure 33). The un–shifted light is provided by the fiber–end–face inside the probe that generates a nearly equal intensity for the un–shifted and Doppler–shifted lights producing the best beat amplitudes. The beat frequency is given by:

$$f_b(t) = |f_d(t) - f_o(t)| = 2\left(\frac{v(t)}{c}\right) f_o(t) \qquad \text{Equation 46}$$

where f_b is the beat frequency, f_d is the Doppler–shifted frequency, f_o is the un–shifted frequency, $v(t)$ is the surface velocity, and c is the speed of light. Since the speed of light can be related to its wavelength (λ) and frequency by $c = \lambda f$, the velocity of the surface can be calculated with:

$$v(t) = \left(\frac{\lambda_o}{2}\right) f_b(t) \qquad \text{Equation 47}$$

where λ_o is the wavelength of the un–shifted light.

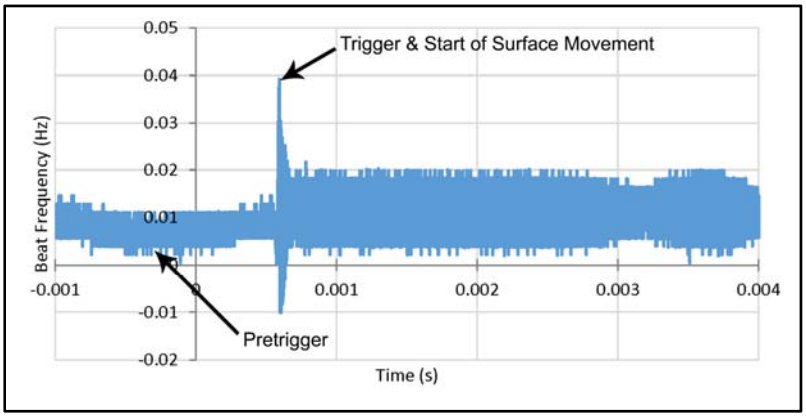

Figure 33. Measured beat frequency signal from PDV, where negative time is from pre–triggering

In the PDV system used, an un–shifted laser light of wavelength 1550 nm was used that corresponds to a frequency of 193,414 GHz, and produces a beat frequency of 1.29 GHz when used on a 1000 m/s velocity surface. Since the system was used with the surface always moving towards the probe, the Doppler–shifted frequency was always greater than the un–shifted frequency. The disadvantage of using a 1550 nm wavelength light is that it cannot be seen by the unaided eye, but is advantageous because it produces lower beat frequencies for a given velocity compared to visible light.

The beat frequency signal collected from an example test using a polymeric SHPB apparatus was digitized and a spectrogram of frequency versus time was generated (Figure 34). The spectrogram output was processed using a sliding Fourier transform method of analysis performed using MatLab (MatLab R2015a, MathWorks) (Appendix A). The first part of the MatLab code performs the spectrogram function on measured data with the following arguments:

256 points per window, an overlap of 256/2, 1024 frequency bins, and a sampling frequency of 25.0 MHz (equal to the PDV measurement sampling rate). The window argument is the amount of sample points per window of the spectrogram affecting the resolution in time, where shorter windows resulted in greater time responses but generally noisier data, and longer windows resulted in a lesser time response but cleaner–looking data. The overlap argument is the number of samples overlapped for each window during the transform, and was used to improve visibility of events occurring faster than the specified window by increasing the time resolution without decreasing the window size. The argument for the frequency bins is the DFT length that affected the resolution in frequency. Lastly, the sampling rate argument is equal to the input data sampling rate and was used to scale the frequency axis.

The second part of the code extracts the significant frequencies by finding the maximum values in the Power spectrum matrix output within a specified expected power range and obtaining their corresponding frequencies. This array of frequencies is then used with Equation 47 to obtain the velocity versus time trace (Figure 35). Generally, the velocity time plots required further processing as a result of unavoidable lab noise. It can be seen in Figure 34 that a line of approximately 6 MHz existed on top of the expected velocity profile. This line explains the velocity of approximately 5 mm/ms seen in Figure 35 between t = 0 and 1.3 ms. The artifacts due to lab noise generally occurred well before and after the rise and peak of the velocity trace resulting in simple corrections.

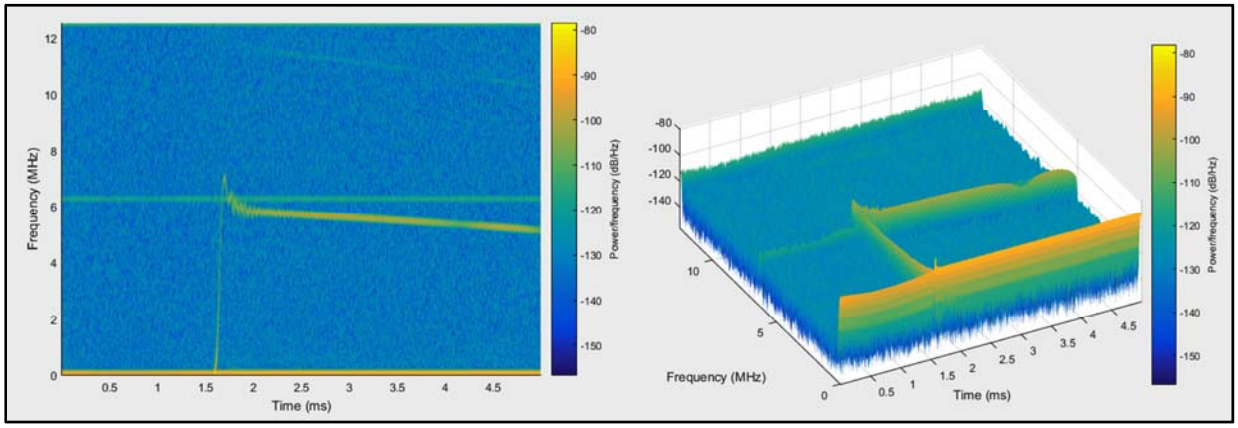

Figure 34. Spectrogram function from MatLab performed on beat frequency signal shown in Figure 33

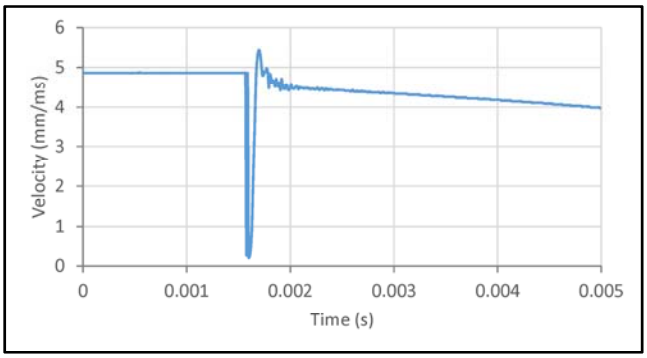

Figure 35. Surface velocity versus time trace of spectrogram output shown in Figure 34

3.3.5 Spectral Analysis Program

A spectral analysis program [155–159] is often used with a polymeric SHPB as a way of processing strain gauge measurements. The program uses SHPB theory (§ 3.2) to determine the propagation coefficient function of a polymer bar for analysis of the propagating waves, which are affected by dispersion and attenuation (§ 3.2.2). The program requires bar geometry, strain gauge location, and calibration data (strain versus voltage relationship) of the bar within a single calibration file. To determine the propagation coefficient function of a single bar, a single voltage–versus–time signal is required. The signal must be from the bar having free–end boundary conditions such that the full incident and reflected waves are measured without transmission or superposition. The measured voltage signal with free–end conditions is inputted into the program and are separated into the incident and reflected waves. With the calibration file and separated wave signals, the program can generate values of the propagation coefficient function in accordance with that previously discussed (§ 3.2.2) as a function of frequencies starting from 0 Hz to the maximum frequency determined by the sample rate of the inputted signals. Appending the propagation coefficient function values to the end of the file then completes the calibration file.

The program can then be used with the completed bar calibration file on any measured voltage data from consequent tests to calculate strain at specific locations of the bar, and calculate bar–end velocity. For a material testing with a traditional SHPB apparatus having polymer incident and transmitter bars, the program can also be used to calculate stress–strain curves for samples

with known geometry [156, 157]. In the case of the using an incident and transmitter bar, two complete calibration files are required.

3.3.6 Cross–correlation Analysis Program

A cross–correlation analysis program (CORA, Partnership for Dummy Technology and Biomechanics, Ingolstadt Germany) is used to calculate the level of correlation between time histories from different tests [165, 166]. The level of correlation is described as the rating and ranges between 0 and 1, with 0 indicating a poor match and 1 indicating a perfect match. The rating is calculated using 2 separate time history signals with the first curve known as the reference signal and the second known as the comparison signal. The reference signal is the result of experimental data whereas the comparison signal is the result of numerical data. The program can perform correlations using both a corridor method and a cross–correlation method. In the case of the ratings presented in this thesis, only the cross–correlation method of analysis was performed, and therefore the corridor method will not be reviewed.

The program performs rating calculations using the structure shown in Figure 36. The cross–correlation (CORA) rating (*C*) is the sum of the weighted load case ratings (C_{LC_i}) given by:

$$C = \sum (w_{LC_i} * C_{LC_i}) \qquad \text{Equation 48}$$

where w_{LC_i} is the weighting of each load case such that $\sum w_{LC_i} = 1$. Each load case rating is the sum of the weighted sub–load case ratings (C_{SLC_i}) given by:

$$C_{LC_i} = \sum (w_{SLC_i} * C_{SLC_i}) \qquad \text{Equation 49}$$

where w_{SLC_i} is the weighting of each sub–load case such that $\sum w_{SLC_i} = 1$. The total sub–load case rating is calculated as the sum of weighted ratings of the corridor and cross–correlation method. If the corridor method is not performed, the cross–correlation method is weighted as 1, resulting in a sub–load case rating given by:

$$C_{SLC_i} = C_{cc}$$ Equation 50

where C_{cc} is the rating of the cross–correlation method performed on the reference and comparison signals.

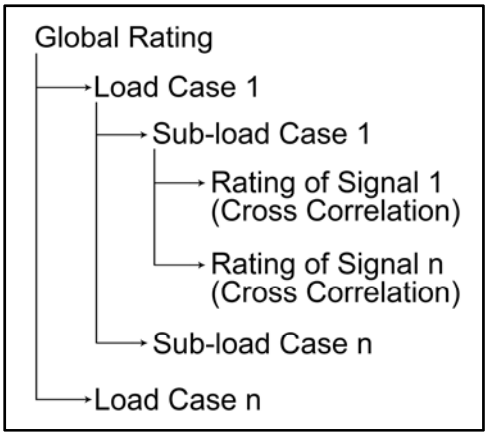

Figure 36. Case structure of cross–correlation rating software

The cross–correlation method of analysis performs comparisons of the reference and comparison signals using three quantification ratings of progression (*V*), phase shift (*P*), and size (*G*). The weighted sum of these three ratings is the total cross–correlation rating given by:

$$C_{CC} = \frac{V + P + G}{3}$$ Equation 51

where the division by 3 indicates equal weighting of each rating type. The program requires the input signals to have the same amount of samples (n) and both within a time range of t_{min} and t_{max} with a constant time interval (Δt). The cross–correlation method begins by shifting the reference signal by multiples of Δt (Figure 37) and calculating a rating using:

$$K_{xy}(m) = \frac{\sum_{i=0}^{n-1}\left(x(t_{min} + (m+i)\Delta t) * y(t_{min} + i\Delta t)\right)}{\sqrt{\sum_{i=0}^{n-1}\left(x^2(t_{min} + (m+i)\Delta t) * y^2(t_{min} + i\Delta t)\right)}}$$ Equation 52

where *x(t)* is the reference signal, *y(t)* is the comparison signal, and *m* is the multiple of Δt with $m = 0, 1, -1, 2, -2, \ldots$. The maximum cross–correlation rating value (K) and its corresponding time shift given by:

$$\delta = m_{\max(K_{xy})}\Delta t \qquad \text{Equation 53}$$

are then used to calculate the progression, phase shift, and size ratings. The amount of phase shifting is constrained within a range of *m* such that the algorithm avoids confusion of comparing signals with repeating waveforms.

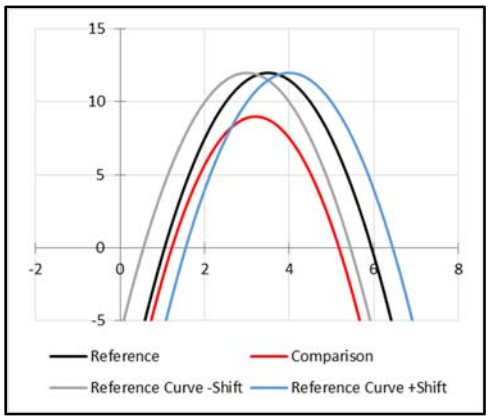

Figure 37. Example of reference signal (curve) shifting in CORA software

The progression rating describes the difference in shape of the reference signal compared to the comparison signal and is calculated by using the maximum cross–correlation rating directly, given by:

$$V = \frac{1}{2}(K + 1) \qquad \text{Equation 54}$$

where $0 \leq V \leq 1$, and the transition between ratings from 0 to 1 is linear.

The phase shift rating describes the amount of time shifting required for the reference signal to obtain the maximum cross–correlation rating, with the minimum and maximum time shift defined by:

$$\delta_{min} = 0.01(t_{max} - t_{min}) \quad \text{Equation 55}$$

$$\delta_{max} = 0.1(t_{max} - t_{min}) \quad \text{Equation 56}$$

indicating the minimum and maximum amount of shifting allowed, respectively. The phase shift rating is then calculated using:

$$P = \begin{cases} 1 & if\ |\delta| < \delta_{min} \\ \dfrac{\left|\delta_{max} - |\delta|\right|}{\delta_{max} - \delta_{min}} & \\ 0 & if\ |\delta| > \delta_{max} \end{cases} \quad \text{Equation 57}$$

where $0 \leq P \leq 1$, and the transition between ratings from 0 to 1 is linear.

The size rating describes the difference in area between the reference and comparison signals by comparing the square of the areas using:

$$G = \begin{cases} \dfrac{F_x}{F_y} = \dfrac{\sum_{i=1}^{n}\left(x^2(t_{min} + i\Delta t)\right)}{\sum_{i=1}^{n}\left(y^2(t_{min} + \delta + i\Delta t)\right)} & if\ F_y > F_x \\ \dfrac{F_y}{F_x} = \dfrac{\sum_{i=1}^{n}\left(y^2(t_{min} + \delta + i\Delta t)\right)}{\sum_{i=1}^{n}\left(x^2(t_{min} + i\Delta t)\right)} & if\ F_y < F_x \end{cases} \quad \text{Equation 58}$$

where $0 \leq G \leq 1$, and the transition between ratings from 0 to 1 is linear. Figure 38 illustrates good and poor examples for each rating described above.

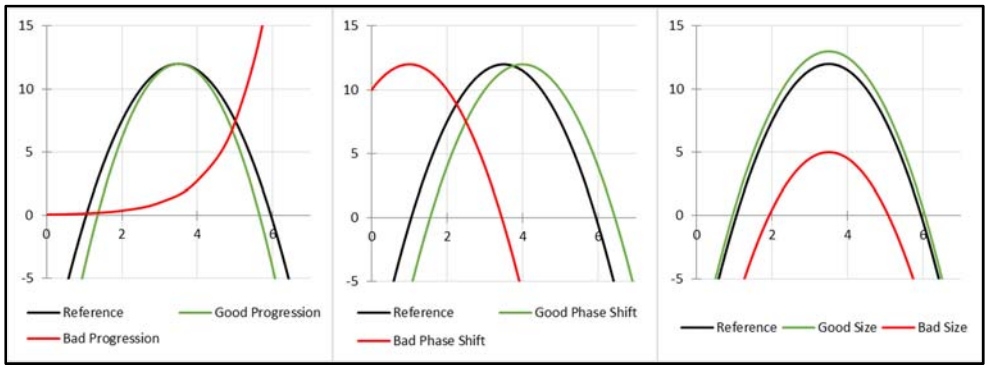

Figure 38. Examples of good and bad progression, phase shift, and size in CORA software

A CORA rating can be calculated for a system by using multiple response metrics as different load and sub–load cases. For example, a single CORA rating can be determined for a SHPB system that produces strain and bar–end velocity traces for differing impact velocities. In this example, the sub–load cases would generate ratings for each metric (strain and bar–end velocity) and each load case would correspond to the differing impact velocity cases. A commonly used baseline for evaluating model fit in biomechanics is the following scale defined by ISO/TR 9790 based on biofidelity of anthropomorphic test dummies [167]:

Excellent	0.86 – 1.0
Good	0.65 – 0.86
Fair	0.44 – 0.65
Marginal	0.26 – 0.44
Unacceptable	0.0 – 0.26

It should be noted that the program requires user–defined parameters, which introduces biasing such that the ratings can be tuned to desired values by changing of parameters. Therefore global parameters must be chosen such that bias is avoided and should remain common and consistent throughout analysis (Appendix B).

3.3.7 Finite Element Modeling

A comprehensive review of finite element modeling will not be presented in this thesis; however, it is useful to give a brief overview on implicit and explicit finite element formulations, verification and validation, and modelling a SHPB apparatus.

Finite element analysis (FEA) is a numerical technique for solving complex problems computationally by approximating solutions to differential equations with initial boundary values. The technique subdivides complex systems, often a set of partial differential equations (PDEs), into smaller parts called finite elements and simpler equations, often a set of ordinary differential equations (ODEs) that govern the element responses. The smaller parts are then systematically recombined to determine the approximate response of the larger system. Both explicit and implicit formulation methods can be used to approximate solutions of time–dependent ODEs and PDEs. In explicit methods, solutions for time–dependent differential equations are numerically approximated at each state (time–step), whereas for implicit methods the equations are solved for

the current and later states simultaneously. Generally, explicit methods are used for dynamic loading where small time–steps are required, such as wave propagation problems. On the other hand, implicit methods are generally used for quasi–static loading where large time–steps can be used, such as structural analysis problems, but require greater computational resources than explicit methods.

Verification and validation are important aspects of developing a numerical model that can produce good approximations of a physical problem. Verification is the act of determining whether the numerical model is behaving correctly and acting as expected. Results are checked according to defined parameters (material models, element formulations, element size, time–step, etc.) and boundary conditions (initial velocities, contact boundaries, etc.) to ensure that they are suitable for the physical problem. Validation is the comparison of simulated results from the numerical model to experimental or theoretical results. Validation is an important stage in numerical modeling because it proves that the numerical model accurately predicts the physical problem and gives confidence in the simulated results.

Finite element modelling of material testing using a traditional SHPB apparatus can be advantageous for visualization of the wave propagation and verification of the measurements. Since the bars are often physically long, any effort in reducing the complexity of the numerical model will reduce computational burden, which reduces the computation time. The sample and bars are often modelled in two–dimension using axisymmetric elements [168, 169] due to the cylindrical geometry of the apparatus and the assumptions made for the propagating waves (§ 3.2). Using two–dimensional axisymmetric elements reduces the amount of calculations performed during simulation and reduces computation time. When three–dimensional effects are expected to occur within the sample, the apparatus can also be modelled in three–dimension using hexahedral elements [170]. The SHPB modelled by Prabhu et al. [170] was modelled with a quadrant setup due to the cylindrical geometry of the bars and sample. By using a quadrant set up, three–dimensional effects within the sample quadrant was observed, while at the same time reducing the computation time. An important aspect of modelling a SHPB apparatus is the size of the finite elements (mesh size) used to discretize the bars and sample. Often the bars a discretized with a coarse mesh [168, 170] due to the simple one–dimensional wave propagation occurring within the

bars. On the other hand, the samples are often discretized with a finer mesh in order to capture stress and strain gradients that occur in the sample. In general, finite element modelling of a SHPB apparatus is advantageous for understanding the dynamics of the tests performed. The SHPB model allows visualizing the propagation of strain in the bars and sample to verify measured data, and explore potential issues that may arise in prospective experiments.

3.3.7.1 Mesh Refinement Study

A mesh refinement study is very important in finite element analysis as it provides verification of result accuracy. The size of the finite elements (mesh size) used in a numerical model can affect the results of the simulation. If the mesh is too coarse (large elements), then the model may not accurately predict the stress and strain gradients. On the other hand, if the mesh is too fine (small elements), then the model will require greater computational resources and time to complete a simulation. Additionally, round–off errors can occur with very fine meshes resulting in an over–convergence. Over–convergence occurs when predicted results from a fine mesh is outside the expected domain of convergence due to round–off errors. The required size of the mesh is unique to the problem analyzed and can be assessed through a mesh refinement study. In general, a mesh refinement study determines if a specific metric (simulation response), or metrics, converges as the mesh size is reduced. A refinement study begins with a simulation using a coarse mesh and the recorded results of the desired metrics. The mesh is refined, typically halved in size, and another simulation is performed with the desired metrics again recorded. The process of refining the mesh and recording the results continues until the results converge to a value within an acceptable error or difference.

A mathematical method used in mesh refinement studies is the Richardson Extrapolation technique. It is used to extrapolate a theoretical value of the metric if the mesh size of the model approaches zero. The Richard Extrapolation value for a given metric (f_0) can be calculated using:

$$f_0 \cong f_1 + \frac{f_1 - f_2}{r^p - 1} \qquad \text{Equation 59}$$

where the rate of convergence (p) is calculated for each metric using:

$$p = \frac{\ln\left(\frac{f_3 - f_2}{f_2 - f_1}\right)}{\ln(r)} \quad \text{Equation 60}$$

The f_3, f_2, and f_1, are the metric values for the coarse, medium, and fine mesh sizes, respectively, and r is the grid ratio. Without calculating the f_0, the error of the fine mesh value (f_1) with respect to f_0 can be estimated using:

$$E_1 = \frac{\left(\frac{f_2 - f_1}{f_1}\right)}{r^p - 1} \quad \text{Equation 61}$$

whereas the actual error can be calculated with the f_0 value using:

$$A_1 = \frac{f_1 - f_0}{f_0} \quad \text{Equation 62}$$

An additional check for convergence available is to determine if the metric value is within the asymptotic zone of the convergence by using:

$$GCI_{23} - r^p GCI_{12} = 0 \quad \text{Equation 63}$$

where the Grid Convergence Index (*GCI*) is given by:

$$GCI = SF * E \quad \text{Equation 64}$$

A safety factor (*SF*) of 1.5 is used as recommended by Roache [171], when the refinement study involves three meshes, whereas a safety factor of 3 is be recommended as a conservative value when using only two meshes in the refinement study. Therefore if Equation 63 is satisfied or is approximately equal to zero, then the metric values are within the asymptotic zone, and the meshes can be assumed as converged.

3.4 Chapter Summary

In summary the alternative cavitation generating methodologies using dynamic loading are the Tube–Arrest (T–A), Bullet–Piston (B–P), and Fluid–Hopkinson bar (F–Hb) methods. The

acoustic method was also briefly discussed, in particular, its limitation of rectified diffusion that results in the reduction of the apparent fluid tensile strengths; therefore it is irrelevant to the motivation and goal of this thesis. The first dynamic method discussed was the T–A method for generating cavitation, which relied on the acceleration of the confinement tube and its impact to generate direct tensile loading. In cavitating conditions, cavitation was observed at the base of the tube, furthest from the impact site, where a pressure transducer was mounted to measure fluid pressure changes. The second and third methods discussed were similar in that they both relied on projectile impacts to generate compressive pulses. The B–P method used bullet impacts on a piston rod that would load the fluid with successive cycles of compression pulses as a result of the wave reflections occurring in the piston rod. The F–Hb method used spherical striker impacts on a loading rod long enough that the compressive pulse was fully generated within the rod before loading of the fluid. In both B–P and F–Hb methods, the compressive pulse would propagate upwards to the free–surface of the confined fluid and reflect at that interface as a tensile pulse due to the lesser impedance of the air compared to the fluid. In non–cavitating conditions the compressive pulse would fully reflect, whereas in cavitating conditions only a portion of the pulse would reflect, and cavitation would be observed at the free–surface.

For the dynamic methods considered, the major limitations recognized and discussed were: (1) the lack of adjustment for loading, (2) the large fluid volumes required, and (3) the lack of a greater impedance boundary enclosing the fluid. A preliminary SHPB apparatus, the T–SHPB–1, that resolved the limitation recognized with the other dynamic methods was developed by Singh et al. [95] and used to investigate fluid cavitation in distilled water. The apparatus successfully generated fluid cavitation using a direct dynamic tensile pulse but presented its own set of limitations. Review of traditional SHPB theory was presented providing further context for the dynamics of the T–SHPB–1 apparatus. The traditional SHPB is a prominent technique in material testing and can be used for blast exposure studies due to its capability of generating high strain–rate and high deformation in material samples. The sample material properties can be obtained through analysis of the incident, reflected, and transmitted strain wave propagation measured from the bars. When polymer bars are used for the SHPB apparatus, the dispersion and attenuation of the propagating strain waves must be accounted for using DFT analysis.

Additionally, a review of experimental diagnostics was presented to provide background information on varying methods to measure system response metrics and process the results for analysis, in association with the development and design of the final apparatus presented in this thesis. In summary, strain gauges can be used to measure strain wave propagation in the bars of an SHPB system, and analysis of the strain signals can be performed using a spectral analysis program developed for processing dispersion and attenuation of waves in a polymer SHPB system; pressure transducers can be used to measure dynamic fluid pressure changes as a result of propagating pressure waves; high–speed video tracking software and a PDV system can be used to determine velocities of surfaces, respectively; and cross–correlation analysis software can compare time history signals for progression, phase shift, and size, to generate a single rating of agreement. Alongside, a brief overview of finite element analysis using an explicit formulation method, and the importance of verification, validation, and mesh refinement studies for numerical modelling were also discussed.

Chapter 4. Development of Novel Cavitation Apparatus

4.1 Motivation and Goals

The motivation of this thesis is the negative ICPs reported occurring at the contre–coup during head blast exposure in computational and experimental studies (§ 1.3.1). The reported occurrences of negative pressure has led to the hypothesis that intracranial cavitation may occur and could be an injury mechanism that can lead to mTBI [34, 39, 43, 79, 87, 88]; however, before this hypothesis can be investigated, an apparatus must first be developed that could dynamically load fluid comparable to the loading observed in head blast exposure and generate localized fluid cavitation with a repeatable process.

The goal of this thesis is to contribute to the knowledge of intracranial cavitation by presenting the development of an apparatus that can produce localized fluid cavitation through high–rate dynamic loading comparable to head blast exposure. This apparatus allows for studies that link the knowledge gap between observed negative ICP during head blast exposure with observable fluid cavitation having repeatable and controlled conditions. The development of a numerical model to further explain the dynamics and measured results obtained from the apparatus is also presented.

4.1.1 Requirements

To achieve the goal of this thesis, the general requirements for the apparatus are as follows: (1) generating negative pressures similar to the ICPs observed in the posterior region of the head during frontal blast exposure; (2) generating loading similar to the ICP observed in the anterior of the head during frontal blast exposure, (3) supporting small fluid sample volumes, (4) having similar material impedance boundaries as the head, and (5) generating localized fluid cavitation.

The first requirement comes from the motivation of this thesis. To link the knowledge gap between negative ICP and observable fluid cavitation, similar negative pressures must be achievable with the apparatus. Similarly, the second requirement comes from mimicking the propagation of the primary pressure wave in the head. It can be generally observed that the response of biological materials exhibit time–dependent behaviour [172]. Since the head is made

up of materials that exhibit time–dependence, it was necessary that the rate of loading generated by the apparatus be comparable to head blast exposure conditions (§ 1.3.1). The consideration of testing biological samples resulted the third requirement for the apparatus supporting small fluid sample volumes. Investigating biological fluids like CSF and their potential for cavitating would be difficult if large volumes were required.

The fourth requirement relates to the first and second requirements. Since material impedance greatly affects wave propagation, the apparatus having comparable impedance boundary conditions on the fluid sample as CSF in the head would be advantageous in supporting the first and second requirements. The impedance boundary conditions were initially simplified as brain–matter surrounded by layers of CSF, bone, and skin exposed to the atmosphere (Figure 39). A simulation of frontal blast exposure was performed using the sagittal blast model developed by Singh et al. [173] (Figure 40). The pressure contours were visualized with colors ranging from red to blue indicating maximum pressure to zero pressure, respectively, and a magenta color was used to indicate negative pressures. Negative pressures were observed in the simplified spherical model with the bone layer displaying a major role in sustaining negative pressure at the posterior region (Figure 40b–e). It was also observed that the brain–matter and CSF shared similar negative pressures, which was expected since they have similar material properties. Therefore it was concluded that the enclosure of the fluid be a high impedance boundary analogous to the bone layer, and the skin layer be neglected due to its comparable pressures to the atmosphere and negligible effects compared with the bone layer.

Lastly, the fifth requirement of generating localized cavitation was to produce repeatable and predictable results, avoiding the uncertainty of cavitation occurring as a result of suspended particles or existing microscopic entrapped air bubbles (§ 2.3).

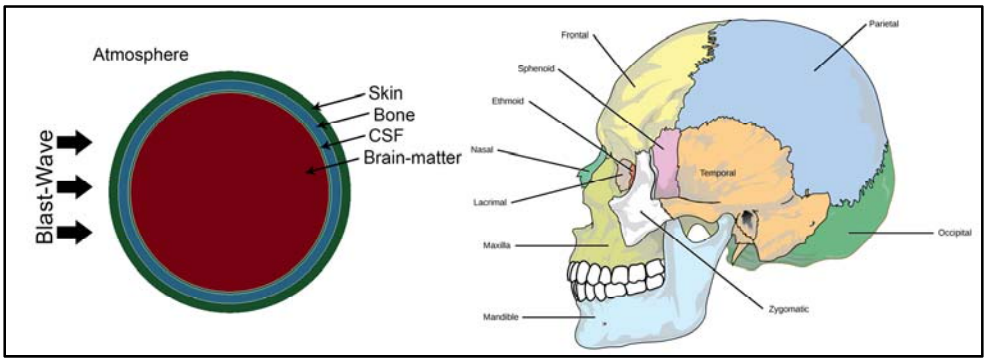

Figure 39. Simplified head model with brain–matter surrounded by bone exposed to the atmosphere compared to the head (Figure adapted from [174]**)**

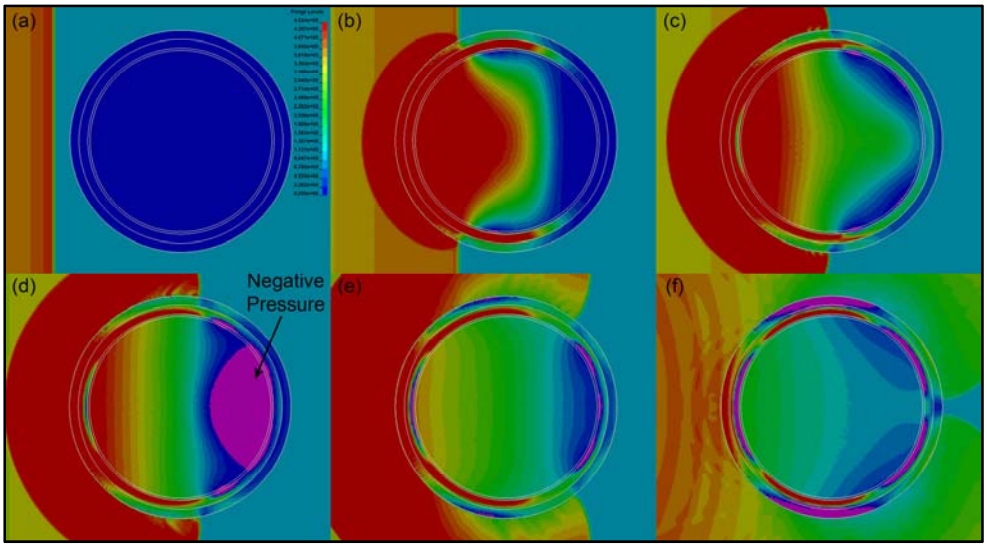

Figure 40. Frontal head blast exposure using a simplified head model with increasing time; Simulation performed using blast model developed by Singh et al. [39]

4.2 Polymeric Hopkinson Bar System Development (T–SHPB–1)

The initial apparatus used to perform a preliminary investigation on generating fluid cavitation (§ 3.1.6) was considered the first iteration of the final apparatus presented in this thesis [95, 175]. The first iteration was classified as the Tensile Split Hopkinson Bar (T–SHPB–1) and the following limitations were recognized during its use: (1) cavitation occurred regardless of the incident wave severity so that a cavitation pressure threshold could not be determined; (2) the apparatus was too compliant allowing air leaks at the o–rings increasing difficulty in distinguishing

between cavitating and non–cavitating events; and (3) the lack of direct fluid pressure measurement to validate the predicted pressures. The following section discusses the development and redesign of the T–SHPB–1 with the aim to resolve the limitations noted along with satisfying the requirements presented in the previous section by performing cavitation tests on distilled water.

4.2.1 Second Iteration Tensile Cavitation Hopkinson Bar (T–MCHB–2)

The second iteration of the apparatus was classified as the Tensile Modified Cavitation Hopkinson Bar (T–MCHB–2). This apparatus used the same aluminum anvil, concentric striker tube, and incident bar configuration used with the T–SHPB–1 to produce a tensile incident wave and dynamically load water confined in a new acrylic (PMMA) confinement chamber. The new chamber was designed with a single–entry point for the incident bar–end, and a piezoelectric probe–style pressure transducer (PCB Piezotronics Model 113B21, sampling rate of 2 MHz) was mounted at its wall to measure water pressure changes (Figure 41). Rubber o–rings were used to contain the water providing a seal for the interface between the incident bar and chamber. The chamber had an outer and internal diameter of 89 mm and 25.4 mm, respectively, and a length of 114 mm. The single–entry bored had a depth of 79 mm, and during cavitation tests the incident bar was placed 44 mm into the chamber resulting in a water volume of ~18 ml.

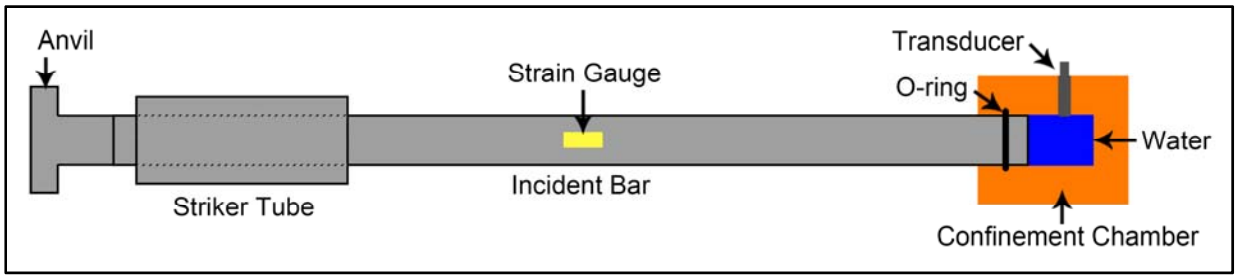

Figure 41. T–MCHB–2 apparatus schematic

A simplified example of the wave propagation occurring in the chamber was as follows (Figure 42). A tensile pulse (incident wave, $\sigma_{I(1)}$) was generated in the incident bar by impact of the striker onto the anvil. The incident wave was propagated and transmitted into the water contained in the chamber ($\sigma_{I(2)}$). Upon reaching the water–acrylic interface (back–wall), a portion of the tensile pulse ($\sigma_{I(2)}$) was transmitted into the chamber (σ_T) and its balance was reflected back into the water as a tensile pulse (σ_R). By generating $\sigma_{I(2)}$ and σ_R with individual magnitudes lesser

than the cavitation pressure threshold of distilled water, it was expected that localized cavitation would occur at the back–wall as a result of the superposition of the $\sigma_{I(2)}$ and σ_R exceeding the threshold. SHPB theory equations (Equation 18 and Equation 19) could no longer be used to approximate the peak negative water pressure for this apparatus because the transmitted tensile pulse (σ_T) reflected back into the fluid due to the chamber acrylic–air interface (chamber–end) affecting the pressure.

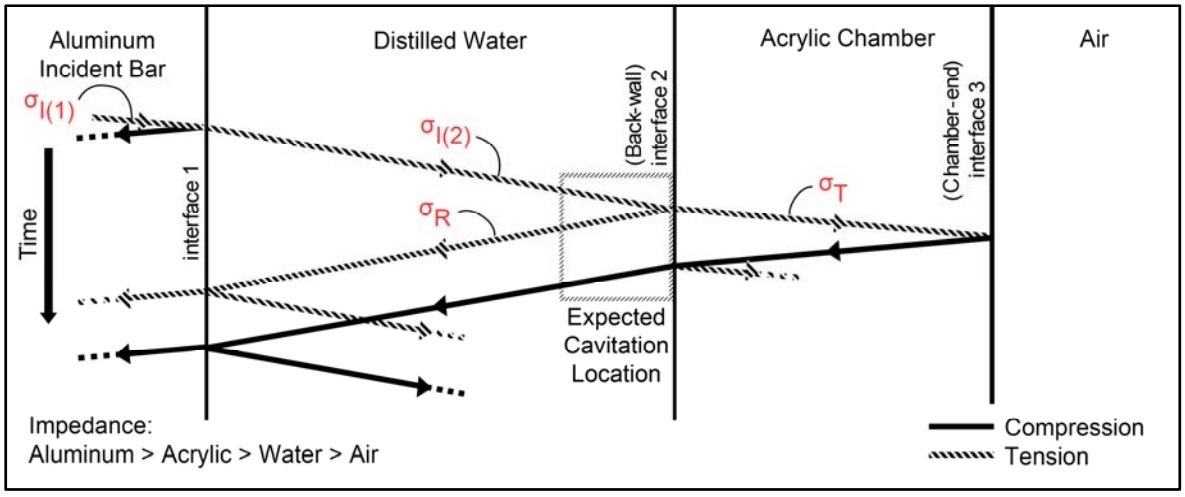

Figure 42. Wave propagation between the incident bar and chamber containing distilled water for the T–MCHB–2

The back–wall had a continuous water–acrylic boundary to ensure that air could not be drawn into the chamber from the atmosphere and be mistaken for cavitation resolving the issue of air leaks recognized with the T–SHPB–1. The pressure transducer mounted to the chamber–wall measured water pressure changes resolving the lack of validation recognized with the T–SHPB–1. The generation of negative pressure for this iteration was the same principle of constructive superposition used in the T–SHPB–1 (Figure 42). Cavitation was expected at the back–wall due to the higher impedance of the acrylic relative to the water, resulting in a reflected wave with the same sense as the incident wave; however, since acrylic has lesser impedance than aluminum, the magnitude of the reflected wave generated in this apparatus was lesser than that generated in the T–SHPB–1. Therefore lesser magnitude negative pressures could be achieved for non–cavitating conditions addressing a limitation of unavoidable cavitation for the T–SHPB–1.

Tests on distilled water were performed and cavitation was successfully produced (Figure 43). As expected, the cavitation observed in the tests were different from those observed with T–SHPB–1 tests since air could no longer leak into the back–wall. Diffuse cavitation was observed indicated by the presence of distinct bubbles throughout the volume of water. A measured incident wave with a peak tensile value of 3.1 MPa produced cavitation in the water corresponding to a measured peak negative pressure of 0.080 MPa. This result was comparable to the peak negative pressure of 0.083 MPa, reported by Hong et al. [176], for diffuse cavitation generated using a similar tensile SHPB system. The peak negative pressure of 0.080 MPa measured on distilled water is lesser by an order of magnitude compared with those reported using the dynamic methods (§ 3.1); however, it is worth noting that the pressure transducers used by both Hong [176] and this apparatus were designed for operation in the compressive pressure ranges, and interpolation of the measured signal to the negative pressure ranges were performed resulting in the possibility of inaccurate measurements.

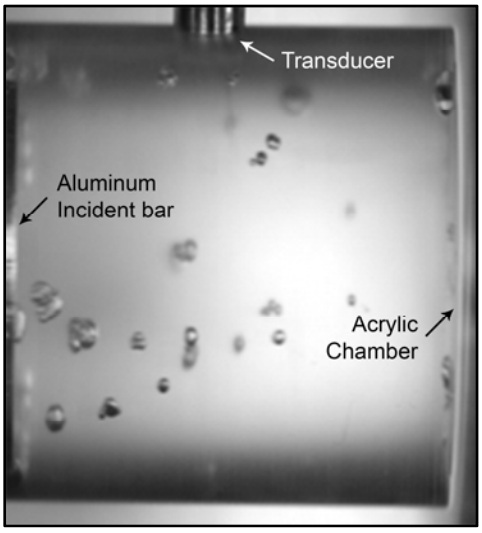

Figure 43. High–speed imaging of diffuse cavitation generated in distilled water using the T–MCHB–2

The limitations recognized for the T–MCHB–2 are as follows: (1) diffuse cavitation was unavoidable within the capable range of striker impact velocities; (2) the low repeatability of the generated tensile incident waves; and (3) the low negative pressures measured resulting in the presumption of inaccurate measurements by the transducer. The lower bound striker impact velocities were constrained by the minimum tensions required for the bungee cords used to propel

the striker tube. Therefore it was suspected that the diffuse cavitation might have been the result of the tensile incident wave exceeding the cavitation pressure threshold resulting in diffuse cavitation before its reflection. Repeatability issues were recognized near the lower and upper range of impact velocities. At the lower range, consistency of the incident wave was affected by the friction between the incident bar and striker, whereas at the upper range consistency was affected by the anvil slipping for a short duration at the instance of impact. Lastly, the peak negative pressure measured by the transducer is orders of magnitude lesser than expected suggesting that the interpolation of the measured signal to the negative ranges may result in inaccurate measurements.

4.2.2 Third Iteration Compressive Modified Cavitation Hopkinson Bar (C–MCHB–3)

The third iteration of the final apparatus was classified as the Compressive Modified Cavitation Hopkinson Bar (C–MCHB–3). This apparatus produced a compressive incident wave by way of an aluminum cylindrical striker and incident bar to load water confined in a chamber. The same aluminum incident bar and acrylic confinement chamber from the T–MCHB–2 were used in this iteration. The anvil and striker tube configuration at the end of the incident bar of the T–MCHB–2 was replaced with a striker bar similar to the configuration of a traditional SHPB apparatus (Figure 44). The striker bar used was 712 mm in length with a diameter of 25.4 mm (long striker) and was launched towards the incident bar by use of a pneumatic system (gas–gun).

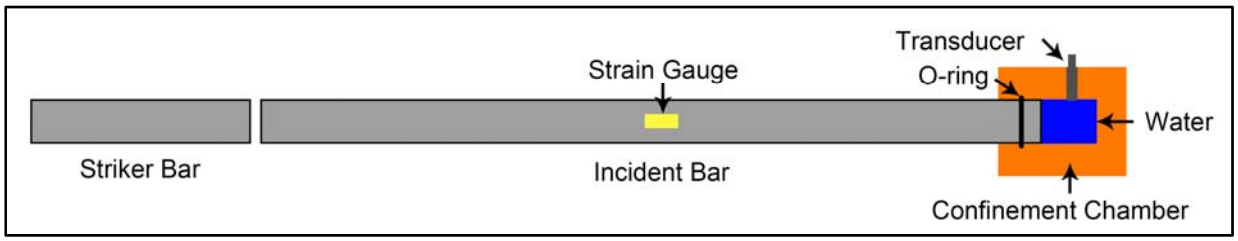

Figure 44. C–MCHB–3 apparatus schematic

Preliminary tests using the C–MCHB–3 showed efficacy in generating repeatable compressive incident waves resolving the issue of incident wave repeatability recognized in the T–MCHB–2. A compressive incident wave further satisfies the first requirement (§ 4.1.1) since the primary pressure wave observed in the head was compressive. It was also presumed that a

compressive incident wave would produce positive water pressures that could be used for validation of the pressure transducer measurements. The generation of negative pressures for this iteration of the apparatus changes from the previous iterations because of the compressive incident wave. The negative pressure required were generated by a tensile reflected wave produced at the chamber–end as a result of the greater impedance of acrylic compared with air (Figure 45), and similar to the previous iteration, cavitation was expected at the back–wall of the chamber.

A simplified example of the wave propagation occurring in the chamber was as follows (Figure 45). A compressive pulse (incident wave, $\sigma_{I(1)}$) was generated in the incident bar as a result of the striker impact. The incident wave was transmitted through the water ($\sigma_{I(2)}$) and transmitted into the chamber end wall (σ_T). Upon reaching the chamber–end, a tensile pulse (reflected wave, σ_R) was produced, which transmitted back into the water superimposing with the trailing–end of $\sigma_{I(2)}$, producing negative water pressures at the back–wall. Maximum negative pressure was expected at the back–wall because the magnitude of the tensile pulse decreases during propagation in the water as a result of attenuation (§ 3.2.2).

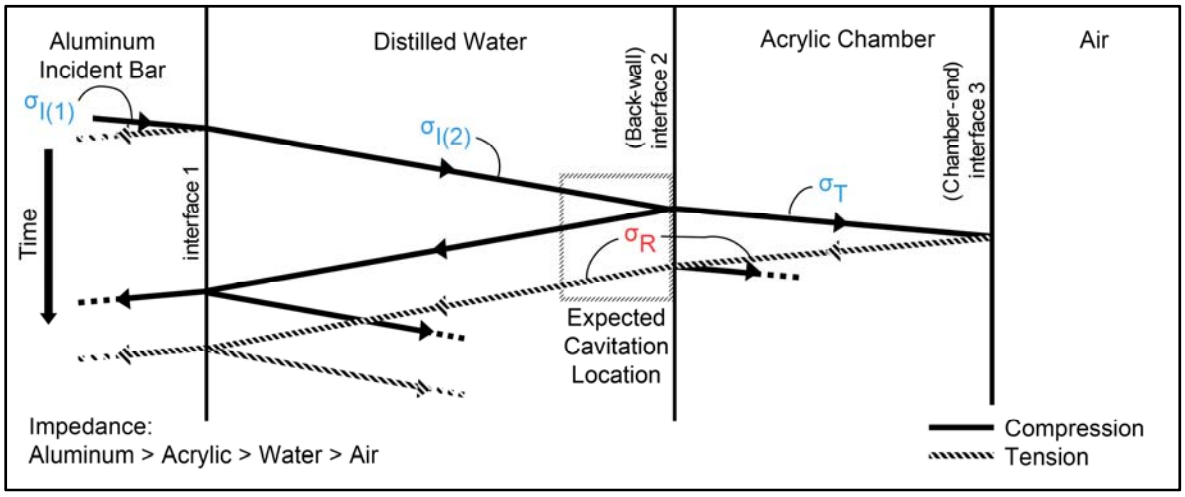

Figure 45. Wave propagation between the incident bar, chamber containing distilled water, and atmosphere for the C–MCHB–3

An axisymmetric model of the C–MCHB–3 was created using an explicit multi–physics finite element program (LS– DYNA, Version 971 Revision 6.1.1) (Figure 46). The apparatus was modelled and discretized with a total of 50,669 axisymmetric elements allowing for a very refined

and computationally efficient model. The aluminum bars were modelled as an elastic material with a density of 2700 kg/m^3, Young's modulus of 68.9 GPa and Poisson's ratio of 0.35. The acrylic (PMMA) chamber was also modelled as an elastic material with a density of 1178 kg/m^3, Young's modulus of 3.47 GPa and Poisson's ratio of 0.35 [155]. The distilled water was modelled as a fluid–elastic material with a density of 1000 kg/m^3 [102, 103, 133] and bulk modulus of 2.19 GPa [41, 102, 103]. The interfaces between the incident bar, water, and chamber were modelled having incorporated shared nodes since the surfaces were not expected to separate during the simulation time considered.

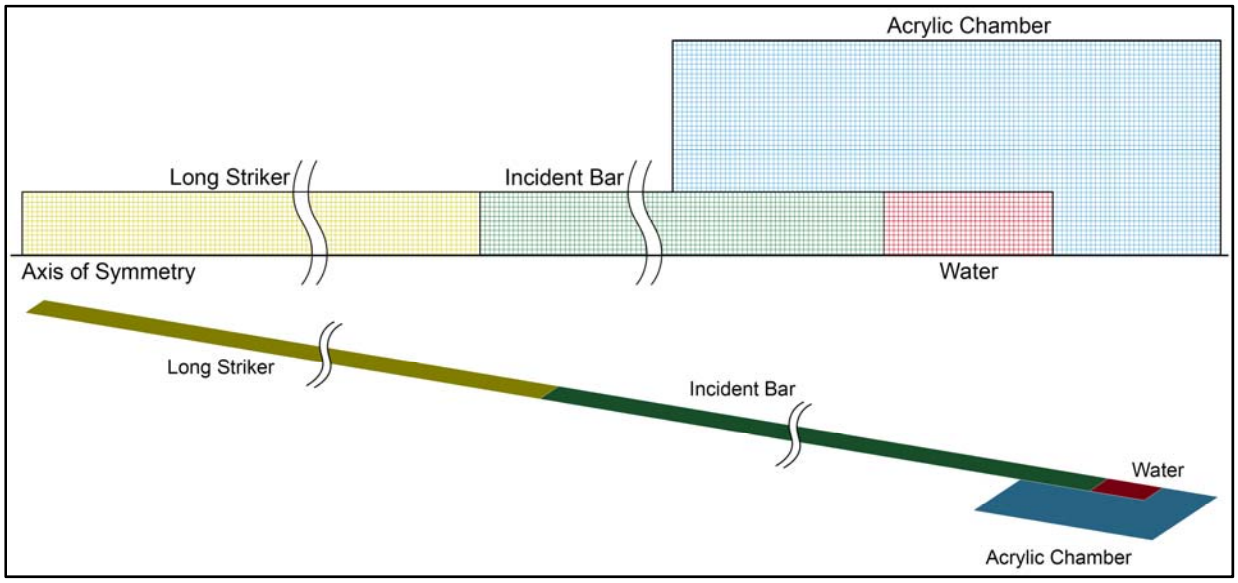

Figure 46. Axisymmetric finite element model of C–MCHB–3 indicating axis of symmetry and discretization of geometry

Eight experimental tests were performed on distilled water and diffuse cavitation was observed for all tests performed similar to that observed with the T–MCHB–2 (Figure 47). Simulations were performed with the numerical model using the striker velocities calculated (Equation 10) with the measured peak incident waves (Table 6).

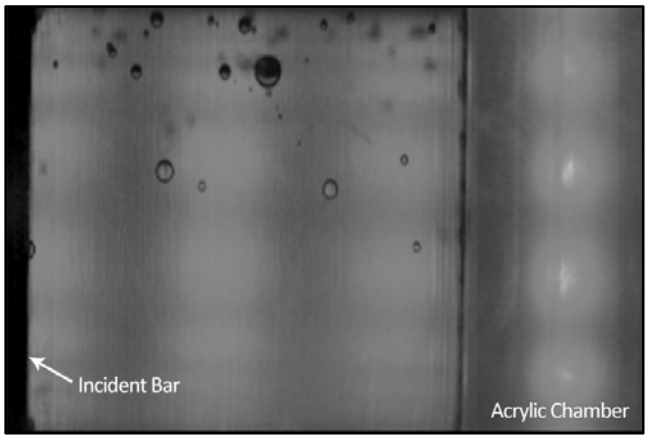

Figure 47. High–speed imaging of diffuse cavitation generated in distilled water using the C–MCHB–3

Table 6. Experimental and numerical results of peak incident wave, water pressure, and negative water pressure using calculated striker velocity

Calculated Striker Velocity (m/s)	Incident Wave (MPa)		Peak Water Pressure (MPa)		Peak Negative Water Pressure (MPa)
	Measured	Simulated	Measured	Simulated	Simulated
0.27	1.85	1.86	1.16	1.27	1.32
0.40	2.75	2.67	1.57	1.88	1.97
0.42	2.88	2.89	1.51	1.88	2.07
0.46	3.12	3.13	2.15	2.13	2.24
0.52	3.58	3.59	2.17	2.44	2.57
0.57	3.90	3.92	2.38	2.67	2.8
1.05	7.17	7.19	4.11	4.92	5.16
1.15	7.85	7.88	4.69	5.38	5.64

There was good agreement between the experimental and simulated results in terms of the timing, rise, and peak values (Figure 48). The incident waves and leading half of the reflected waves were in excellent agreement with their leading and trailing edges on top of one another. The slight difference in the latter half of the reflected wave could be attributed to losses in the system like the rubber o–rings that decreased the stiffness of the apparatus compared to its numerical model. The second incident wave occurring after ~900 ms was the result of the reflected wave reflecting at the striker–end of the incident bar and was considered irrelevant to the study; and similarly, the second reflected wave occurring after ~1400 ms was considered irrelevant to the study.

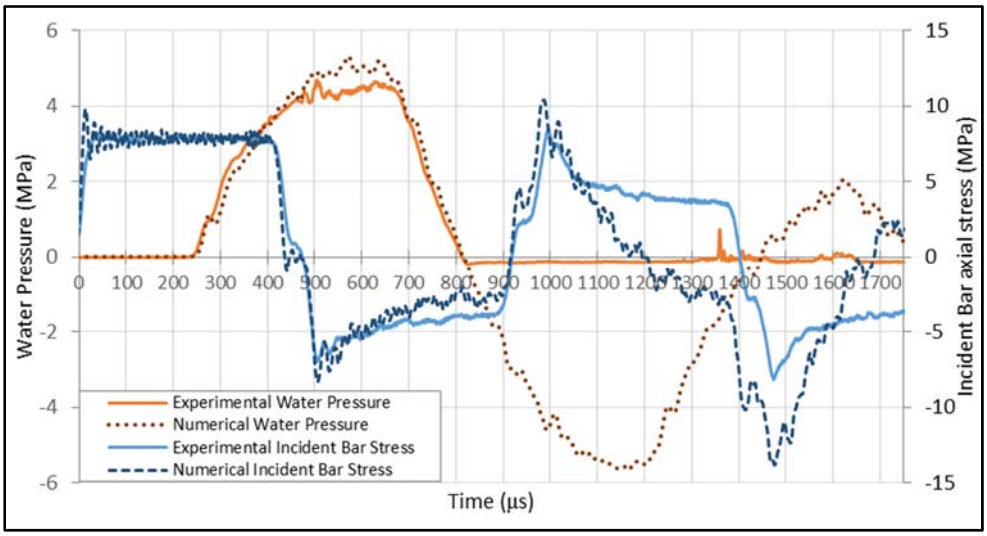

Figure 48. Incident bar axial stress and water pressure history traces for 1.15 m/s striker velocity using the C–MCHB–3

The positive phase of the water pressure was in good agreement at the leading and trailing edge with the numerical model predicting the 'step–like' increase and decrease, respectively. The constant negative pressure (~0.140 MPa) measured by the transducer (PCB Piezotronics Model 113B21, sampling rate of 2 MHz) confirms the presumption that it inaccurately measured negative pressures. The second positive pressure phase occurring after ~1450 ms in the simulation was not measured suggesting that the diaphragm decoupled from the sensing element during the negative pressure phase. Additionally, one would expect that if the constant value measured was related to the occurrence of cavitation then transient compressive pulses, similar to that seen at ~1400 ms (but greater magnitude), would be seen throughout the timeframe of ~900 – 1450 ms (simulation negative phase) corresponding to the collapse of bubbles similar to that measured by the transducers using the T–A method [131, 132]. Overall, the good agreement of the incident bar stresses and initial positive pressure phase gives confidence in the negative pressures predicted by the simulations. The upper bound negative pressure that could have been achieved in the experimental tests can be assumed to be approximately that of the peak negative pressure simulated since cavitation of the water was not defined in the numerical model; therefore the predicted negative pressure in the model could be greater than that achieved in its corresponding experimental test.

The ‘step–like’ increases observed at the leading edge of the water pressure (Figure 48) were the result of the superposition of the compressive pulse transmitted by the incident wave reflecting back–and–forth within the chamber. The initial ‘step’ in the pressure traces occurring at ~250 – 300 ms was the initial water pressure wave (IWPW) transmitted into the water before it reflected at the back–wall and superimposed on itself; therefore its peak could be calculated with Equation 19. The IWPW was calculated for each test and trends were generated for its analytical, numerical, and experimental values with respect to peak incident wave stress (Figure 49). As expected, the analytical values were the upper bound because they assumed one–dimensional wave propagation, unlike the numerical (2–D axisymmetric) and experimental (3–D) approaches. Likewise, the experimental values had the lowest values because of the losses in the system that was not included in the numerical model such as, the rubber o–rings, transducer port seal, and fixture friction.

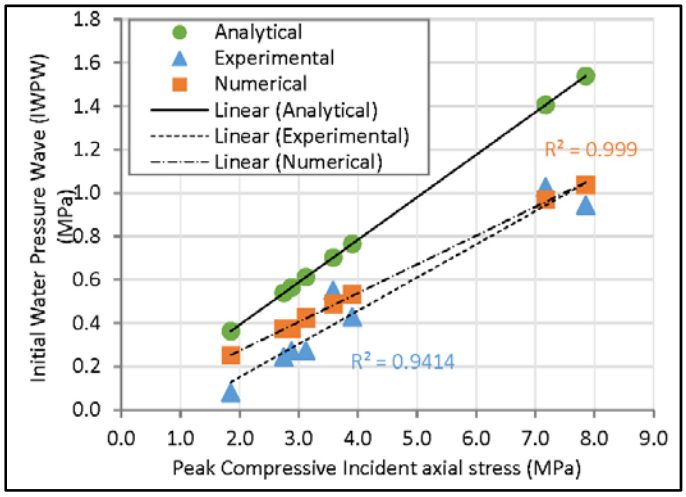

Figure 49. Peak Initial Water Pressure Wave (IWPW) transmitted into the water trends for analytical, experimental, and numerical tests using the C–MCHB–3

Trends of the peak positive water pressure with respect to peak incident wave stress for the numerical and experimental cases were generated, and as expected the simulated values were greater than the experimental values (Figure 50). There was better agreement at the lesser incident stresses compared with the greater stresses, which could be attributed to the compliance of the o–rings since leaks were more prominent at greater water pressures.

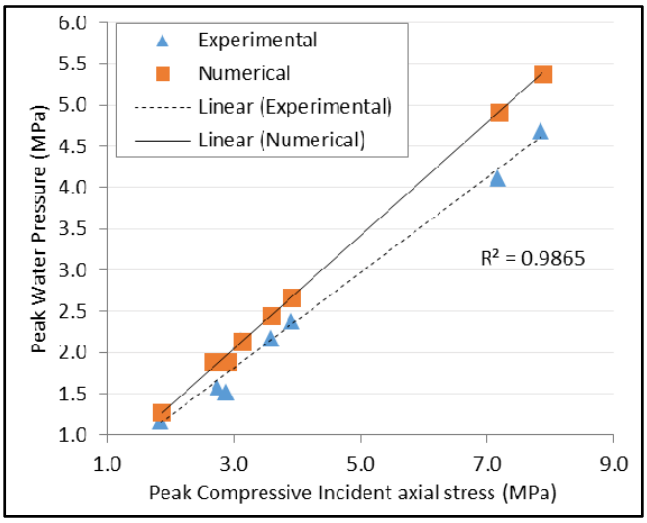

Figure 50. Peak water pressure trends for experimental and numerical tests using the C–MCHB–3

This iteration of the apparatus demonstrated better reproduction of blast exposure conditions compared with the previous iterations. The compressive incident wave is analogous to the compressive primary pressure wave observed in the head; the low impedance water is analogous to brain–matter and CSF; and the high impedance chamber and its exposure to the atmosphere is analogous to the cranial bones surrounded by lesser impedance materials (skin and air). The difference in agreement of the experimental and simulated results at low and high incident stresses demonstrated the significance and efficacy of developing a numerical model to predict the apparatus dynamics. The difference in agreement highlighted the issue of using o–rings as a seal, which could otherwise have been overlooked. Additionally, the numerical model confirmed the presumption that the negative pressures could not be accurately measured due to limitations of the transducer.

The set of limitations recognized for the C–MCHB–3 are as follows: (1) diffuse cavitation was unavoidable within the capable range of impact velocities; (2) the presence of the transducer reduced the cavitation pressure by creating nucleation sites; (3) the inability of the transducer to measure negative pressures; and (4) the high intensity rectangular incident wave exhibited excessive overlap within the chamber. The first limitation of unavoidable diffuse cavitation could be attributed to 2 causes. The first and most simple to resolve was the possibility of microscopic air pockets providing nuclei for cavitation at the chamber–cavity walls as a result of its roughness.

The second cause was observed through analysis of high–speed imaging showing inertial–induced motion of the chamber with respect to the incident bar as a result of the propagating waves (Figure 45). This motion caused an increase in volume of the chamber cavity $\left(\frac{dV}{V_o}\right)$ containing a constant mass of water, resulting in a global drop in pressure that can be approximated by Equation 2.

The second and third limitations relating to the pressure transducer were also observed from the high–speed imaging. The roughness of the transducer diaphragm provided nuclei for cavitation similar to the cavity walls noted above, and entrapped air within the threading of the transducer port were also drawn into the water during tests at high striker impact velocities. These issues provided challenges in distinguishing cavitation as a result of unwanted seeding or the negative pressures exceeding the cavitation pressure threshold. Lastly, the loading of the apparatus was limited in that it generated rectangular incident waves with short durations (~0.45 ms) as a result of the elastic bars; while a shape and duration similar to the primary pressure wave observed in the frontal region of the brain (Figure 7) was desired. The intensity of the incident waves generated were far too great even at the slowest impact velocity achievable by the gas–gun (0.27 m/s) suggesting a lesser impedance incident bar material should be used. A lesser impedance material would be preferred over further reduction in the striker velocity because vibrational and frictional effects become more significant at lower velocities and repeatability may decline.

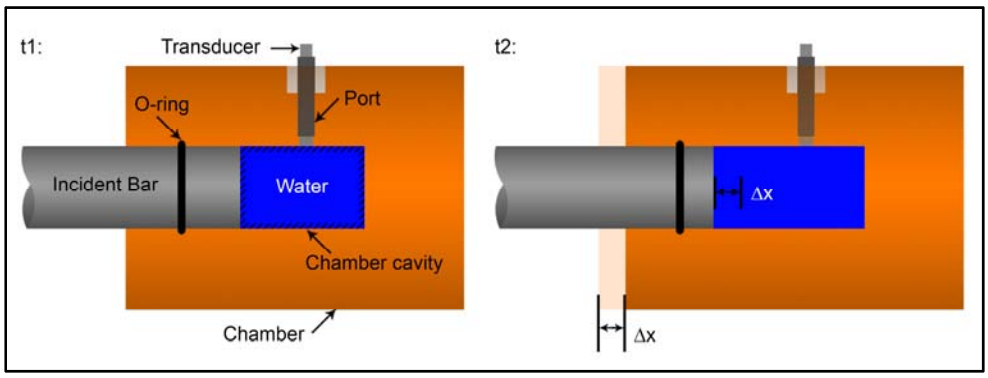

Figure 51. Illustration of bulk separation between the chamber and incident bar at time t2 > t1 resulting in a chamber cavity volume increase

4.3 Fourth Iteration Closed–Chamber and Modified Cavitation Hopkinson Bar (C^3HB)

The important findings from the first three iterations of the apparatus included (1) the relatively straightforward ability to generate cavitation, albeit diffuse cavitation; (2) the limitations of existing pressure transducers in terms of measuring negative pressures and creating cavitation initiation sites (§ 4.3.3); (3) the importance of achieving consistent fluid conditions, challenges with o–ring type seals resulting in leaked or entrapped air, and cavitation nucleation sites (§ 4.3.2); and (4) the benefit of using a numerical model to predict dynamics and fluid pressures in place of an intrusive pressure transducer (§ 4.5.3).

This section presents and discusses the final design of the apparatus classified as the Closed–Chamber Cavitation Hopkinson Bar (C^3HB) apparatus. For this final iteration, an acrylic (PMMA) incident bar was used with a steel (low–carbon steel) spherical striker. The benefit of the spherical striker was to generate compressive pulses comparable in shape to the primary pressure wave observed in the head. The incident bar was 2438 mm in length with a 25.4 mm diameter, and the steel sphere striker was 25.4 mm in diameter. A gas–gun was used to propel the sphere striker towards the incident bar striker–end, and strain gauges were mounted at the midpoints of both the incident bar and chamber to measure changes in strain (§ 4.3.1). The acrylic (PMMA) chamber was redesigned as a separate closed–piece mounted flush at the end of the incident bar (§ 4.3.2). A PDV probe was also pointed at the chamber–end to measure its changes in velocity (§ 4.3.3).

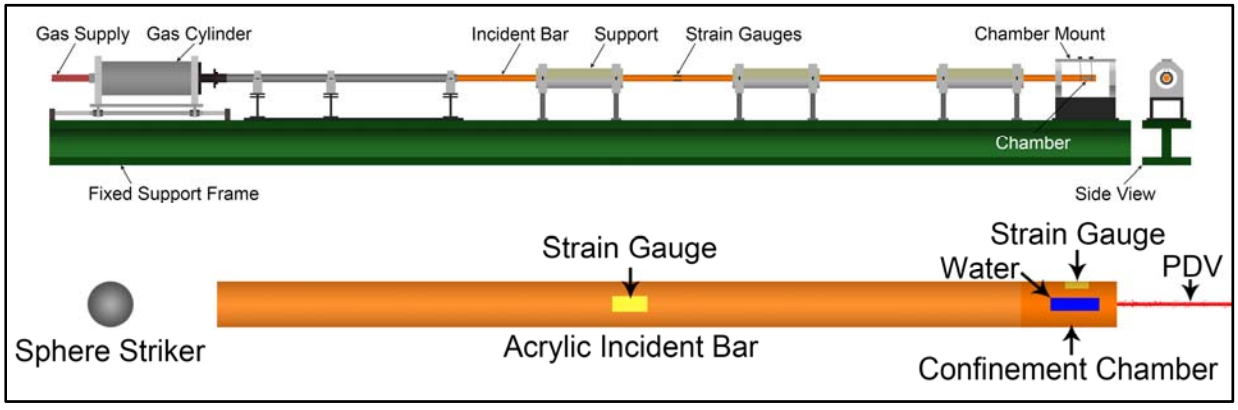

Figure 52. C^3HB apparatus schematic

4.3.1 Loading

In all previous iterations of the experimental apparatus, cavitation was observed for all tests performed. In other words, it was generally not possible to test the non–cavitating condition and therefore determine the cavitation pressure threshold. It was recognized that the magnitude of the incident waves generated were far too great, and the aluminum bars should be replaced with a lesser impedance material, such as acrylic. The aluminum incident and striker bars of the C–MCHB–3 were replaced with an acrylic incident bar and steel sphere striker, respectively. The acrylic incident bar in different setups has shown its efficacy in generating repeatable compressive incident waves in past studies [149, 150, 156, 157]. The combination of the incident bar and sphere striker was able to generate a compressive incident pressure wave that was comparable in general shape and rate to the primary pressure wave observed in the head from frontal blast exposure (Figure 52) fulfilling the second requirement of the apparatus development.

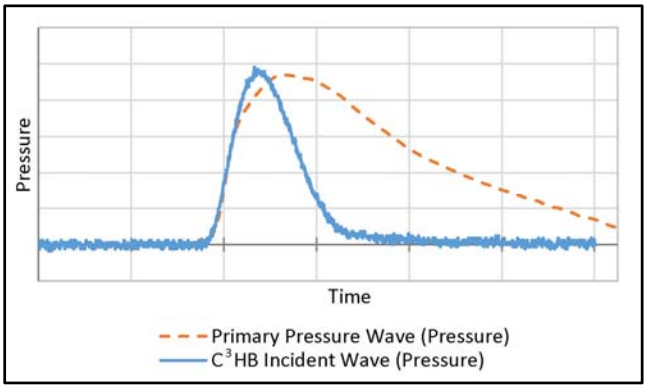

Figure 53. Primary pressure wave from sagittal head model developed by Singh [39, 173] **compared to the incident wave pressure trace at the chamber from the C^{3}HB**

The generation of negative pressure in the C^{3}HB was similar to that of the C–MCHB–3 in that cavitation was expected at the chamber back–wall as a result of a tensile reflection. An advantage of having a short versus long duration incident wave was that the tensile reflection that produces negative pressures also has a short duration and achieves a greater magnitude because the peak of the tensile pulse superimposes with the trailing–end of the compressive pulse sooner. This is illustrated with a simplified example of a short (10 s) and long duration (15 s) incident wave having equal rise times (5 s) and magnitudes (20 Pa) superimposing with their respective

reflected waves (Figure 54). The negative pressure generated by the short and long duration are 12 Pa in magnitude with ~6 s duration and 6 Pa in magnitude with ~10 s duration, respectively.

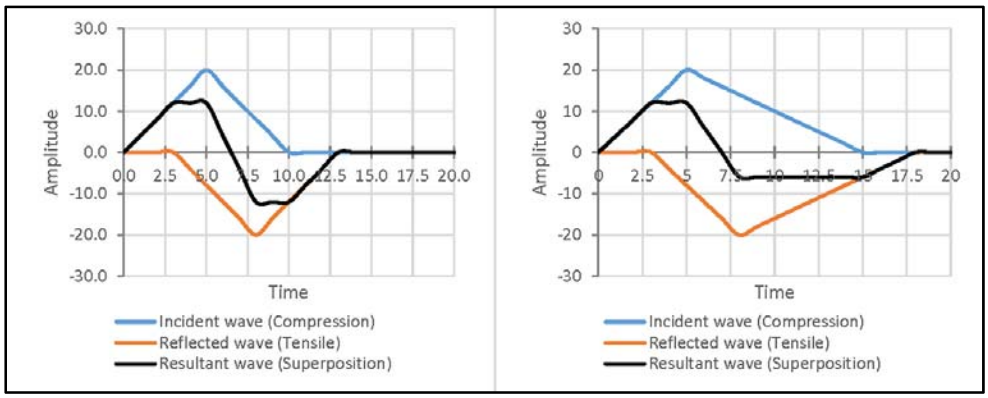

Figure 54. Simplified comparison of a short and long duration incident wave superimposing with their tensile reflections

4.3.1.1 Propelling the Sphere Striker

The same pneumatic system (gas–gun) used for the C–MCHB–3 was used for this apparatus; however the system was designed to accelerate 25.4 mm diameter cylindrical striker bars as opposed to spherical strikers. For all tests performed with the metallic sphere striker, the sphere striker was placed ~673 mm away from the incident bar striker–end. The sphere striker was propelled by the use of an acrylic precursory striker with a length of 236 mm and diameter of 25.4 mm. This precursory striker was placed into the piston of the gas–gun and launched towards the sphere striker. The precursory striker would then impact with the sphere striker, propelling it towards the incident bar (Figure 55). This method of propelling the sphere striker and corresponding travel distance of ~673 mm proved effective in that no secondary impacts were observed within the timeframe of the tests.

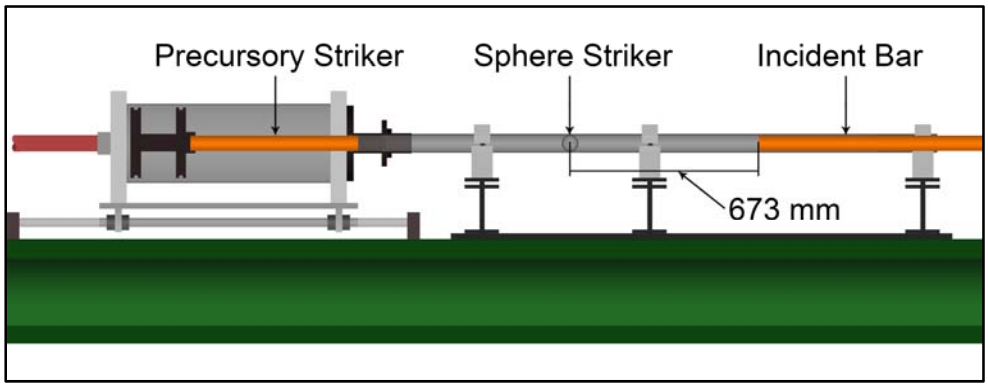

Figure 55. See–through schematic of gas–gun, precursory striker, sphere striker, and travel distance

4.3.2 Cavitation Chamber Design

It was previously discussed that the combination of the surface roughness of the chamber cavity and the motion of the chamber relative to the incident bar resulted in diffuse cavitation using the C–MCHB–3. The final iteration of the chamber was redesigned as an independent, fully enclosed component (Figure 56). The redesign emulates the head, but at a smaller size conducive to testing small amounts of fluid, by surrounding the fluid with a single high impedance material analogous to the cranial bones, which fulfills the fourth requirement of the apparatus development. The redesign also removes the constraint on the chamber as a result of friction between the incident bar and rubber o–rings, enabling greater movement after wave transmission that better replicates the boundary conditions of the head during blast exposure compared with the previous designs.

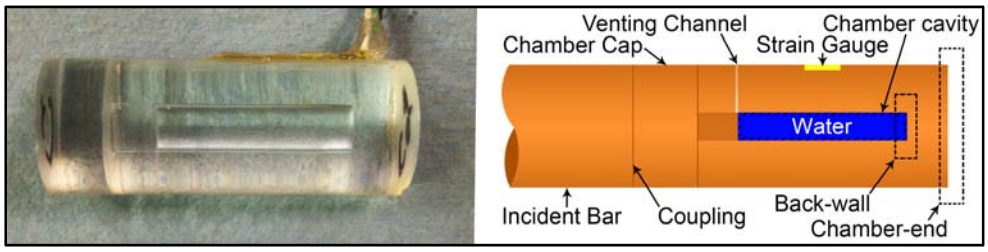

Figure 56. Acrylic confinement chamber for the C^{3}HB apparatus indicating important features

The dimensions of the new acrylic cylindrical chamber were chosen to provide comparable thickness to that of the skull and to further reduce the fluid volume required for each test. The thickness of the skull varies from ~7.4 – 11.3 mm from the parietal to the occipital bone of the sagittal head model developed by Singh [39, 173] that used head geometry derived from the Visible

Human Project male data set [177] (Figure 57); similar thicknesses were reported in [178, 179]. The diameter of the chamber was set at 25.4 mm, corresponding to the diameter of the incident bar. A chamber cavity diameter of 6 mm was selected to produce a wall thickness within the median of the range (9.7 mm), and a thickness of 11.3 mm was selected for the acrylic forming the back–wall. The length of the chamber cavity was determined using a simplified fully elastic numerical model of the C^3HB. A parametric study of varying chamber cavity lengths resulted in a minimum length of 35 mm that provided distinct negative fluid pressures occurring at the distal region of the chamber (region adjacent to the back–wall), which resulted in a cavity volume of ~1 ml that fulfills the third requirement of the apparatus development. Sanding the inner surface of the chamber with 800, 1200, and 2400 grit sandpaper and then polishing with 0.3, 0.1, and finally 0.05-micron alumina powder, successively, resolved the surface roughness issue of the chamber cavity.

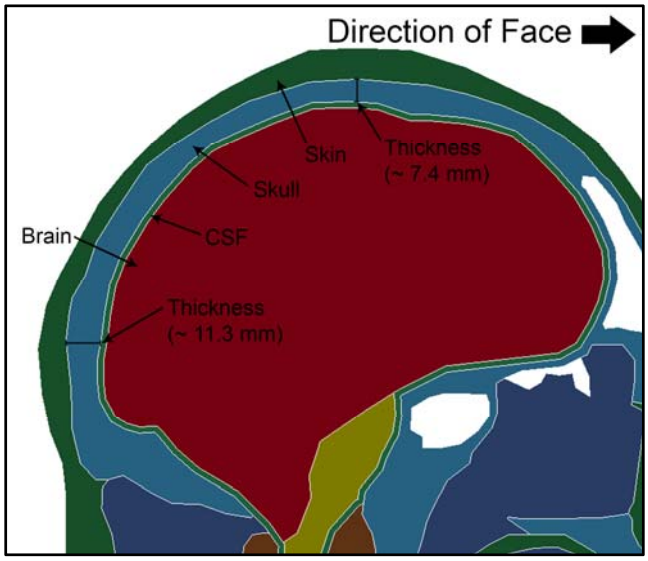

Figure 57. Thickness at the upper region of the occipital bone from sagittal head model developed by Singh et al. [39, 173]

The dimensions of the chamber cap were determined with the goals to simplify wave transmission and sealing of the fluid. The head of the cap was given a diameter equal to the chamber body and a thickness equal to the back–wall (Figure 58). The stem of the cap was given a diameter that produced a transition fit with the body providing fast and simple sample preparation

using light physical force. Features such as threads were avoided since they would produce stress concentrations and increase the complexity of wave transmission. Adhesives were considered but provided challenges in producing consistent nuclei–free samples. A cap stem length of ~8 mm was determined to provide the adequate amount of friction for the transition fit and to minimize stresses at the stem's base during its fabrication (lathing). A 0.5 mm diameter venting channel was cross–drilled at the side–wall of the chamber body at the open–end to allow excess fluid to vent from the chamber when installing the cap (Figure 58). It was positioned such that the cap stem, when fully inserted into the body, covers the channel. This ensured that the fluid was not compressed and its pressure remained atmospheric when the chamber was fully inserted. The chamber was suspended from the chamber mount at the end of the incident bar by 0.2 mm diameter fishing line looped around its circumference to minimize friction and its effect on wave propagation.

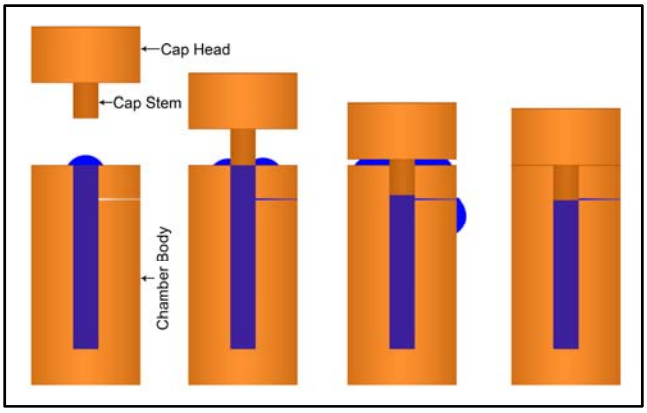

Figure 58. Process of capping the chamber and pressure relief of the water through the venting channel

4.3.3 Determining Fluid Pressure

The following sections discuss how the fluid pressure in the new acrylic confinement chamber was determined through analytical (§ 4.3.3.1) and numerical (§ 4.5) methods. Issues with measuring the negative fluid pressures were recognized with the piezoelectric pressure transducer used in the previous iterations of the apparatus. The initial positive fluid pressure phase (compressive) in the C–MCHB–3 were validated in good agreement with its numerical model giving confidence in the fluid pressure traces simulated, and it was suggested that the peak negative pressure obtained in the simulation was the upper bound negative pressure that could be

experienced with the experiment conditions. Additionally, it was recognized through the high–speed imaging that the roughness of the pressure transducer diaphragm and geometric changes of the port provided nuclei for cavitation, and entrapped air from the port threads were drawn into the water during high impact velocities, creating challenges in distinguishing cavitation as a result of unwanted seeding or negative pressures exceeding the cavitation threshold.

4.3.3.1 One–Dimensional Approximation of Fluid Pressure

The fluid pressure at the back–wall can be approximated with an analytical process having the following assumptions: (1) the fluid is distilled water; (2) the wave propagation in the chamber between the water and acrylic is one–dimensional; (3) the back–wall acrylic surface has the same velocity as the chamber–end; and (4) waves do not reflect back towards the back–wall upon reaching the cap. A single water element located at the back–wall was analyzed having a water boundary to its left and an acrylic boundary to its right (Figure 59). The pressure in the element changes as a result of the boundary velocity difference caused by the transmission of force from the acrylic to the water.

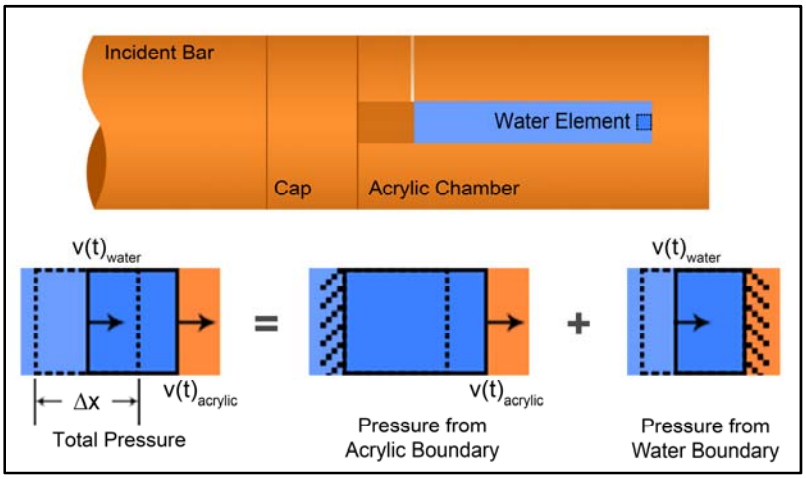

Figure 59 One–Dimensional approximation of the fluid pressure at the back–wall

An approximation of the total element pressure can be calculated by adding the effects of the left water boundary and the right acrylic boundary. The mass of the element is given by:

$$\rho = \frac{m}{V} \qquad \text{Equation 65}$$

where ρ is the density of water and V is the volume of the element. Since the chamber cavity was cylindrical, and the element was located at its center, the element was given a cylindrical volume with a length of Δx:

$$m = \rho(\pi r^2 \Delta x) \qquad \text{Equation 66}$$

The pressure acting on either side of the element can be calculated by:

$$P = \frac{F}{A} = \frac{am}{A} = \frac{\left(\frac{\Delta v}{\Delta t}\right)\rho(\pi r^2 \Delta x)}{\pi r^2} = \left(\frac{\Delta v}{\Delta t}\right)\rho \Delta x \qquad \text{Equation 67}$$

where Δv is the change in velocity of the side, and Δx is the element length given by:

$$\Delta x = C_o \Delta t \qquad \text{Equation 68}$$

where C_o is the acoustic wave speed at the boundaries. Since the acrylic boundary was the driver (assumption 2), the velocity trace of the water boundary was equal to that of the acrylic boundary but behind a time–step; however, the transmitted velocity must be scaled due to the acoustic impedance difference of the water and acrylic (§ 3.2.1) using Equation 10:

$$\eta = \frac{\sigma_{transmitted}}{\sigma_{incident}} = \frac{2\rho_{water} C_{o_{water}}}{\rho_{water} C_{o_{water}} + \rho_{acrylic} C_{o_{acrylic}}} \qquad \text{Equation 69}$$

With the assumption that the water boundary was fixed, the pressure applied by the acrylic boundary can be calculated as:

$$P_{acrylic}(t) = -\left(\frac{\Delta v}{\Delta t}\right)\rho \Delta x = -\rho_{water} \Delta x \left(\frac{v(t) - v(t-1)}{\Delta t}\right) = -\rho_{water} C_{o_{acrylic}}\big(v(t) - v(t-1)\big) \qquad \text{Equation 70}$$

where the negative indicates a tensile force and $v(t)$ is the velocity measured by the PDV. Likewise, if the acrylic boundary was fixed, the pressure applied by the water boundary is:

$$P_{acrylic}(t) = -\rho_{water}\Delta x\left(\frac{v(t-1)-v(t-2)}{\Delta t}\right) \quad \text{Equation 71}$$
$$= -\rho_{water}C_{o_{water}}\big(v(t-1)-v(t-2)\big)\eta$$

Lastly, both effects can be summed to determine the pressure of the element resulting in:

$$P_{backwall}(t) = -\rho_{water}\left[\Big(\big(v(t)-v(t-1)\big)\Big)C_{o_{acrylic}} + \Big(\big(v(t-1)-v(t-2)\big)\Big)C_{o_{water}}\eta\right] \quad \text{Equation 72}$$

4.3.3.2 Pressure Transducers

The piezoelectric probe–style pressure transducer (PCB Piezotronics Model 113B21, sampling rate of 2 MHz) used in the previous iterations (T–MCHB–2 and C–MCHB–3) was not included in the new chamber design because the small dimensions of the chamber could not accommodate the transducer, and due to the limitations previously discussed (§ 4.2). A small diameter catheter–style (piezoresistive sensor) pressure transducer (SPR–524 Mikro–Tip Catheter Transducers, Millar Inc., sampling rate of 2 MHz) cross–mounted at the back–wall was also investigated; however, three issues were identified: (1) the presence of the catheter introduced nucleation sites and reduced the cavitation pressure thresholds measured similar to the probe transducer; (2) the catheter could not be used over the striker impact velocity range because pressures generated in the water were too great resulting in one transducer being permanently damaged at negative pressures required to generate cavitation; and lastly, (3) the transducer provided inaccurate measurements due to the impedance difference between the water and sensing element. It was previously concluded from the C–MCHB–3 that a numerical model was able to predict the compressive water pressure in the chamber, in good agreement with transducer measurements (the initial positive or compressive pressure phase). Therefore, in addition to an analytical method (§ 4.3.3.1), a numerical model of the C^3HB was also created, developed, and validated to predict the negative fluid pressures occurring during tests (§ 4.5).

4.3.4 Instrumentation: Strain Gauge, PDV, High–speed Imaging

Strain gauges (CEA–13–250UW–120, Micro–Measurements) with a 120 Ω resistance were mounted on the surface of the acrylic incident bar at 1137 mm from the striker–end in a Wheatstone bridge configuration (§ 3.3.1.1). A biaxial strain gauge (WA–09–120WR–120, Micro–Measurements) with a 120 Ω resistance was also mounted on the surface of the acrylic confinement chamber at the center of the chamber cavity in a quarter–bridge configuration. The strain gauges were amplified (2210B Signal Conditioning Amplifier, Vishay) and data was recorded at a frequency of 2 MHz using a high–speed data acquisition system (BNC–2110, National Instruments) (Figure 60). The PDV (1550 nm wavelength, Ohio Manufacturing Institute) was used to measure the velocity of the chamber–end (§ 3.3.4) [163, 164]. Reflective tape was placed on the chamber–end to increase its reflectivity ensuring a high signal–to–noise ratio. A high–speed camera (FASTCAM SA5 Model 1300K–M1, Photron) with a lens (105 mm 1:2.8 DG Macro HSM, Sigma) focused at the back–wall of the chamber was used to identify if cavitation occurred during tests. The camera was set to capture video at 100,000 frames per second with a 320x192 resolution and was processed (Photron FASTCAM Viewer Version 3.50, Photron). An LED light (JAB Bullet, AAdynTech) was placed behind the chamber to provide backlighting for the high–speed imaging. The pneumatic system with compressed nitrogen gas was used to launch the precursory striker towards the sphere striker (§ 4.3.1.1).

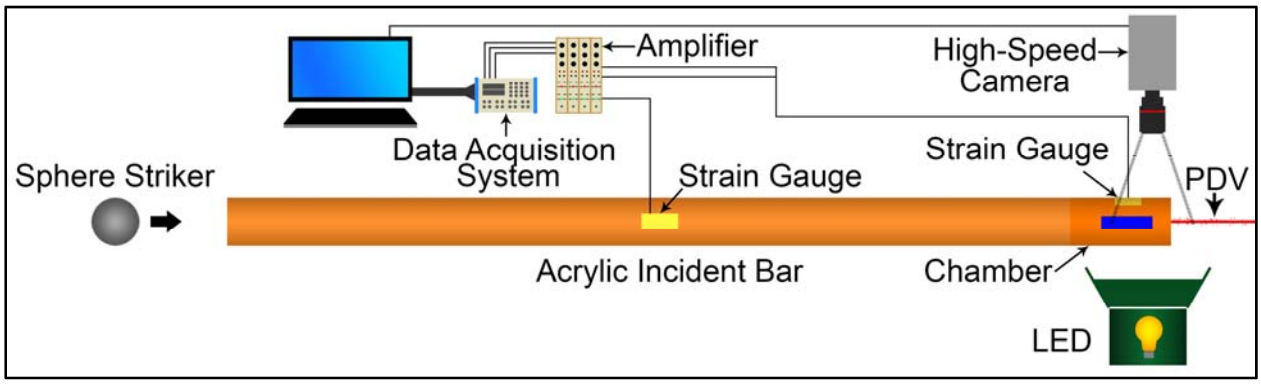

Figure 60. Schematic of instrumentation used for C^{3}HB cavitation tests

4.4 Verification of Methods

This section describes the calibration process for the strain gauges mounted on the incident bar and chamber (§ 3.3.1). The agreement of the spectral analysis program (§ 3.3.5) and PDV (§ 3.3.4) in generating and measuring surface velocities are verified, respectively; and the uniformity of the generated incident wave throughout the cross–section of the bar is verified (§ 3.2.2).

4.4.1 Strain Gauge Calibrations and Validation

The strain gauges were calibrated by fixing one end of the bar and chamber and applying a known load (Figure 61). The chamber was filled with distilled water during the calibration process to represent the test condition. A strain–to–voltage relationship was obtained for the range of loading expected during cavitation tests (Table 7). The incident bar was radially constrained throughout its length with supports to minimize buckling, and when buckling was observed, the calibration process was ended. The chamber was not supported since it was not expected to bend due to its low length–to–diameter ratio. Calibration was performed in a short duration to circumvent viscoelastic properties of the acrylic such as relaxation and was performed multiple times to ensure repeatable results.

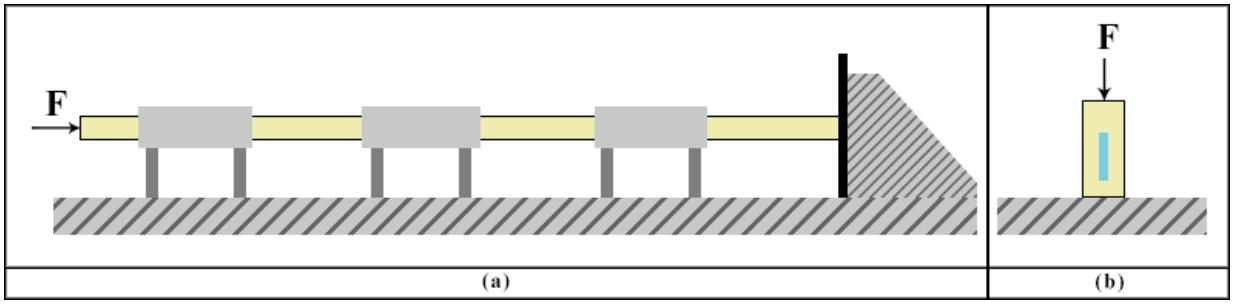

Figure 61. (a) Incident bar strain gauge calibration with supports; (b) Chamber strain gauge calibration

Table 7. Strain gauge strain–to–voltage output relationships

	Strain Gauge (mε/V)
Incident Bar	1.55
Transmitter Bar	1.52
Chamber 1 (C1)	2.60
Chamber 2 (C2)	2.67
Chamber 3 (C3)	2.80

The chamber was also calibrated under dynamic compression using a traditional SHPB apparatus with acrylic incident and transmitter bars. The chamber was placed between the bars, and a compressive pulse was propagated throughout the entire length. Since the chamber was the same material as the bars, it was expected that the compressive pulse would fully transmit through the chamber and into the transmitter bar without producing a reflected wave. This method assumed that the distilled water had minimal effect on the propagating pulse; therefore, the strain measured at the transmitted bar (output wave) should be the strain measured at the incident bar (input wave) after the effects of attenuation and dispersion are considered. To verify this assumption, the input wave was propagated using the spectral analysis program to the location of the transmitter bar strain gauges. After verifying the propagated input wave was equal to the output wave, the output wave was propagated to the chamber strain gauge, and a strain–to–voltage relationship of the chamber was determined using known incident and transmitter bar strain–to–voltage relationships from static calibrations. As expected the relationship obtained for the chamber using dynamic calibration was comparable to that obtained from static calibration.

An important advantage of calibrating a strain gauge after mounting is that the error that can result from the resistance increase by temperature changes and use of lead wires (§ 3.3.1.1) are integrated into the strain–to–voltage relationship. Therefore, as long as the system setup remains the same throughout testing, the effect of temperature and lead wires on the strain gauge voltage output can be neglected.

4.4.2 Incident Bar Repeatability/Benchmark Tests

Tests using the incident bar with free–end conditions (free–end tests) and a cylindrical acrylic striker bar were performed to measure the effects of attenuation and dispersion of the propagating strain pulses for varying striker conditions using known existing conditions (Figure 62). These tests were considered as benchmark tests since the full incident and reflected waves were measured without wave transmission and was used for validation purposes for numerical modeling (§ 4.5). The striker conditions included 3 varying striker types at 3 varying gas–gun firing–pressures. The strikers used were an acrylic cylindrical bar of 452 mm length and 25.4 mm diameter (short), an acrylic cylindrical bar of 712 mm length and 25.4 mm diameter (long), and a steel sphere of 25.4 mm diameter. The gas–gun firing–pressures used were 97, 124, and 152 kPa,

and were obtained through preliminary tests corresponding to the low, medium, and high striker impact velocities. The striker impact was filmed using high–speed imaging (Photron SA5 model 1300K–M1, 50,000 frames per second with a 512x272 resolution) and its velocity was obtained using tracking software (Tracker, Douglas Brown, http://physlets.org/tracker/) (§ 3.3.2). The free–end surface velocity of the incident bar was also measured using the PDV. Each set of tests had 3 repeats resulting in 9 individual tests per striker, and 27 total tests performed. The strain and free–end velocity data of the 27 individual tests are presented in Appendix C.

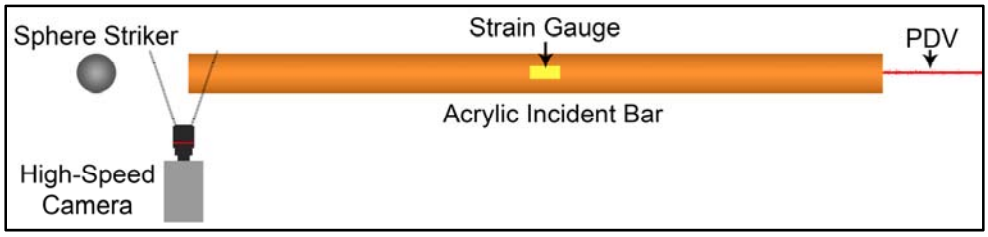

Figure 62. Schematic of incident bar free–end tests with high–speed imaging and PDV

4.4.3 Spectral Analysis and PDV Verification

The spectral analysis program (§ 3.3.5) and PDV (§ 3.3.4) were verified to ensure that the calculated and measured surface velocities were in agreement, respectively. Firstly, the spectral program was verified in its efficacy to propagate viscoelastic waves using the 27-benchmark tests (§ 4.4.2). For each test, the incident wave was propagated the distance from the strain gauges location to the free–end and back to generate a reflected wave, resulting in excellent agreement with the measured reflected wave (Figure 63). Cross–correlation analysis (§ 3.3.6) was performed comparing the calculated and measured reflected waves for all 27 tests resulting in a rating of 0.994, verifying the efficacy of the wave propagation method and program in propagating waves in the acrylic incident bar for varying striker conditions. Then the incident bar free–end velocity traces were calculated using the spectral analysis program and was used to verify PDV measurements. Cross–correlation analysis was performed comparing the calculated and measured free–end velocities resulting in a rating of 0.967, verifying excellent agreement between the diagnostics. The slopes of calculated versus measured peak values are comparable to unity (ideal case) with 0.995 and 1.042 for the reflected wave and incident bar free–end velocity, respectively (Figure 64). The spectral analysis program was verified with reflected wave measurements

independent from the PDV, therefore verification of the PDV using the spectral analysis program was justified, and was concluded that the spectral analysis program and PDV are in agreement.

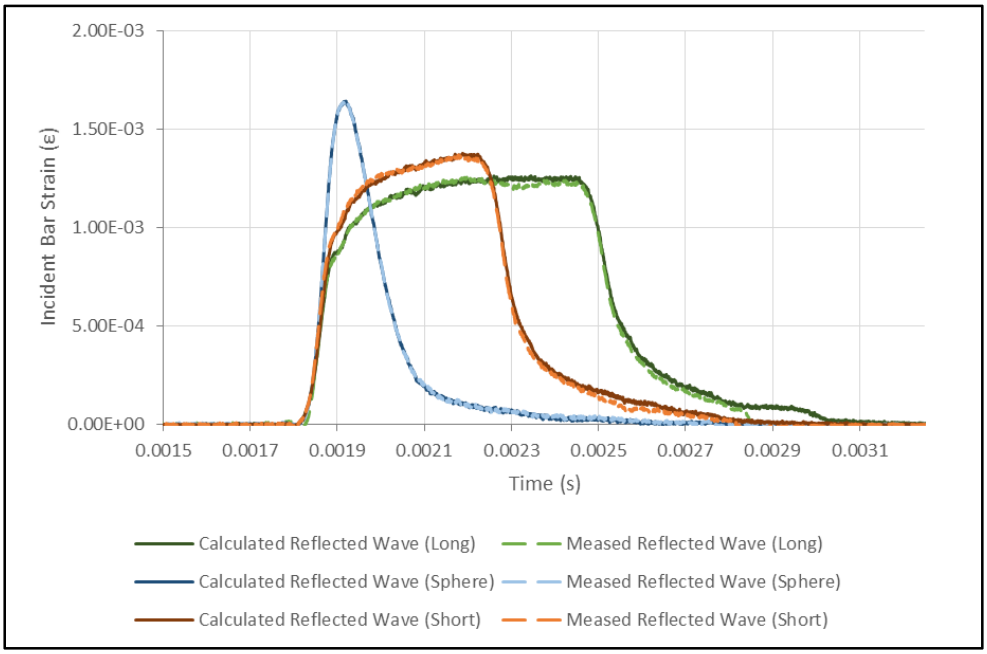

Figure 63. Calculated and measured reflected waves for 124 kPa firing–pressure with varying strikers

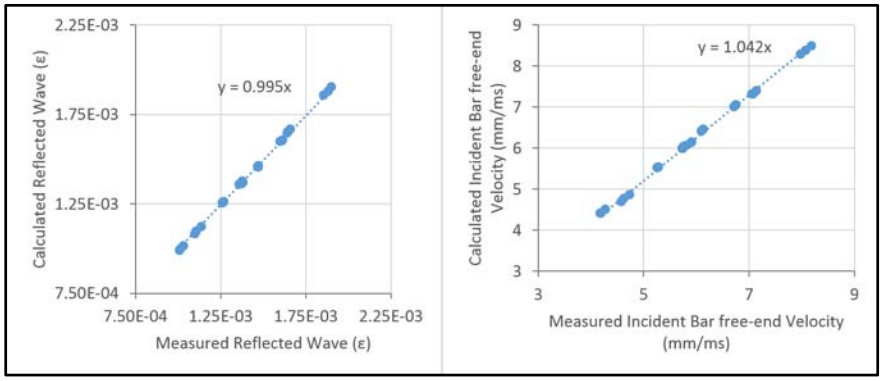

Figure 64. Slope of the calculated values with respect to measured values demonstrating comparability to unity

4.4.4 Uniform Incident Wave Validation

Davies suggests that the propagating incident wave must be uniform throughout the cross section of the incident bar such that one–dimensional analysis can be performed on the SHPB bars

[152]. Six free–end tests were performed with the incident bar and sphere striker at the same gas–gun firing–pressure. The PDV was used to measure the incident bar–end velocity for 3 tests with the probe pointed at the center of the surface and 3 with it pointed near the edge of the surface (Figure 65). The maximum standard deviations for both cases (based on population) were calculated for the incident bar strains and free–end velocities demonstrating low variability and repeatability (Table 8). As expected, the mean values for the edge and center cases showed negligible differences of 0.2% for the incident bar strain and 0.3% for the free–end velocity. This was also supported by a two–tailed T–test resulting in no significant difference between the set of values for each case at $p < 0.01$. Therefore it was concluded that the incident wave was uniform throughout the cross section of the bar upon reaching its free–end and the chamber.

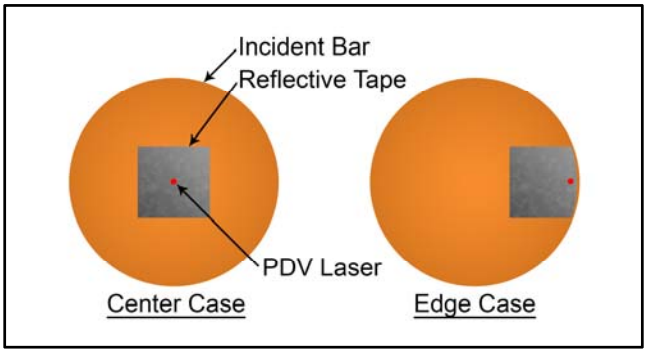

Figure 65. Schematic of PDV laser location on the incident bar free–end for the center and edge cases

Table 8. Mean peak incident strain and free–end velocity and their maximum standard deviation

Cases	Incident Bar Strain		Free–end Velocity	
	Mean Peak Value (mε)	Maximum Standard Deviation	Mean Peak Value (mm/ms)	Maximum Standard Deviation
3x Center	1.927	1.7%	7.253	2.1%
3x Edge	1.923	0.0259 1.3%	7.228	1.4%

4.5 Numerical Modelling

4.5.1 Finite element model development

An axisymmetric numerical model of the apparatus was developed for the purpose of predicting the fluid pressure changes within the chamber, since the intrusive nature of a pressure gauge provided potential cavitation sites effectively reducing the cavitation pressure threshold. It should first be noted that the numerical model provides the theoretical pressure in non–cavitating fluid, since the fluid was treated as a continuum and a cavitating event was not defined. The apparatus geometry, loading, and boundary conditions were axisymmetric; therefore axisymmetric elements were used to discretize the geometry (Figure 66). This allowed for a very refined and computationally efficient model. The numerical model was analyzed using an explicit multi–physics finite element solver (LS–DYNA, Version 971 Revision 6.1.1, LSTC, Livermore CA). Following a mesh refinement study (§ 4.5.4), a mesh with 203,008 axisymmetric quadrilateral elements (~0.39 mm element size) was used with the acrylic material modelled as an Ogden hyperelastic material (§ 4.5.2) for both the incident bar and chamber. The fluid (distilled water) was modelled as a fluid–elastic material, and the spherical steel striker as a linear elastic solid. The water density used was 1000 kg/m^3 [102, 103, 133] with a bulk modulus of 2.19 GPa [41, 102, 103]. For the steel sphere, a density of 7840 kg/m^3, a Poisson's ratio of 0.29, and a Young's modulus of 207 GPa were used [180, 181]. The interface of the chamber cap and body perpendicular to the propagating compressive pulse was modelled as two separate surfaces and contact was addressed using a penalty–based contact algorithm. The interface between the inner–walls of the chamber and water was modeled using shared nodes, since these surfaces were not expected to separate during the simulation time considered. Lastly, since the cavitation event itself was not implemented in the numerical model, the model was limited to predicting the fluid dynamics for non–cavitating conditions and before the initiation of cavitation during cavitating conditions.

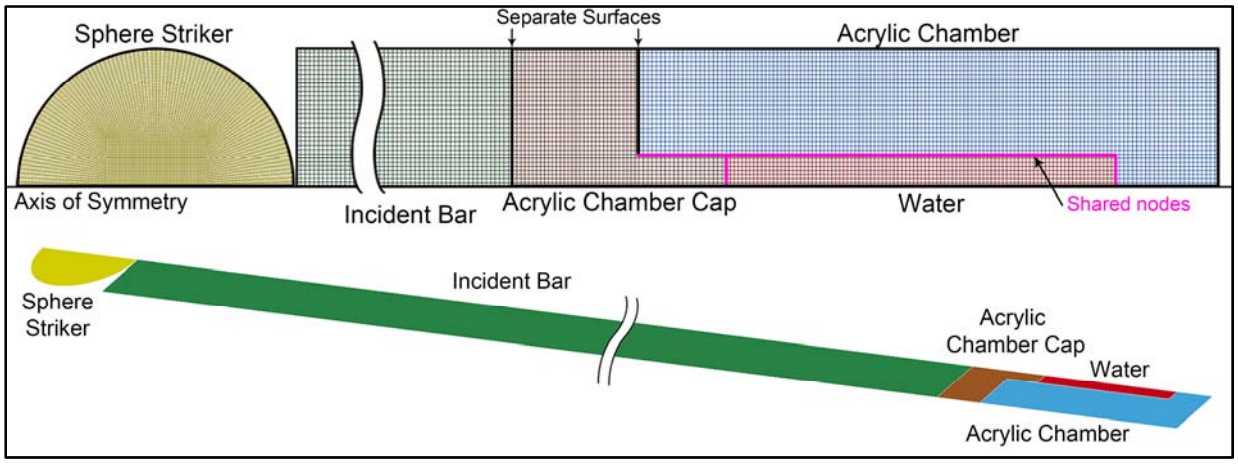

Figure 66. Axisymmetric finite element model of C³HB indicating axis of symmetry and discretization of geometry

4.5.2 Ogden Constitutive Model Parametric Study

The acrylic (PMMA) constitutive model parameters were determined through optimization analysis using the 9.168 mm/ms sphere striker free–end benchmark test (§ 4.4.2). The axisymmetric numerical model of the apparatus without the chamber was used with the incident bar modelled using an Ogden hyperelastic material model (Figure 67). The Ogden constitutive model used incorporated a multi–term strain energy function [182]:

$$W^* = \sum_{i=1}^{3} \frac{\mu_1}{a_1}\left(\lambda_i^{*a_1} - 1\right) + K(J - 1 - lnJ) \qquad \text{Equation 1}$$

where μ_1 was the shear modulus, λ_i^* was the principal stretch with the volumetric effects removed, K was the bulk modulus, and J was the relative volume. The rate effects were taken into account with a viscoelastic term:

$$\sigma_{ij} = \int_0^t g_{ijkl}(t-\tau)\frac{\partial \sigma_{kl}^E}{\partial \tau}\, d\tau \qquad \text{Equation 2}$$

where σ_{ij} was a linear viscoelastic term, σ_{kl}^E is the instantaneous stress, and the relaxation function $g(t)$ is the 4–term function:

$$g(t) = \sum_{i=1}^{4} G_i e^{-\beta_i t} \qquad \text{Equation 3}$$

where G_i is the shear relaxation modulus for the i[th] term, and β_i is the decay constant of the i[th] term.

The optimization analysis was performed to determine the material model constants for the single 9.168 mm/ms impact scenario. The optimization was preceded by several initial analyses to identify the sensitivity and appropriate limits for the Ogden model parameters. After identifying appropriate limits, an optimization study was performed using a response surface methodology (LS–OPT Version 5.2, LSTC, Livermore, CA). The optimization used a polynomial sampling and D–optimal methodology with a space–filling algorithm. Convergence was evaluated using a tolerance criterion using multi–objective function of Mean Squared Error, Curve Matching, and Peak Values [183], with all metrics equally weighted. All cases of the optimization analysis converged to relatively the same parameter values (Table 9) with the final optimization analysis converging after approximately 8 iterations (Figure 68).

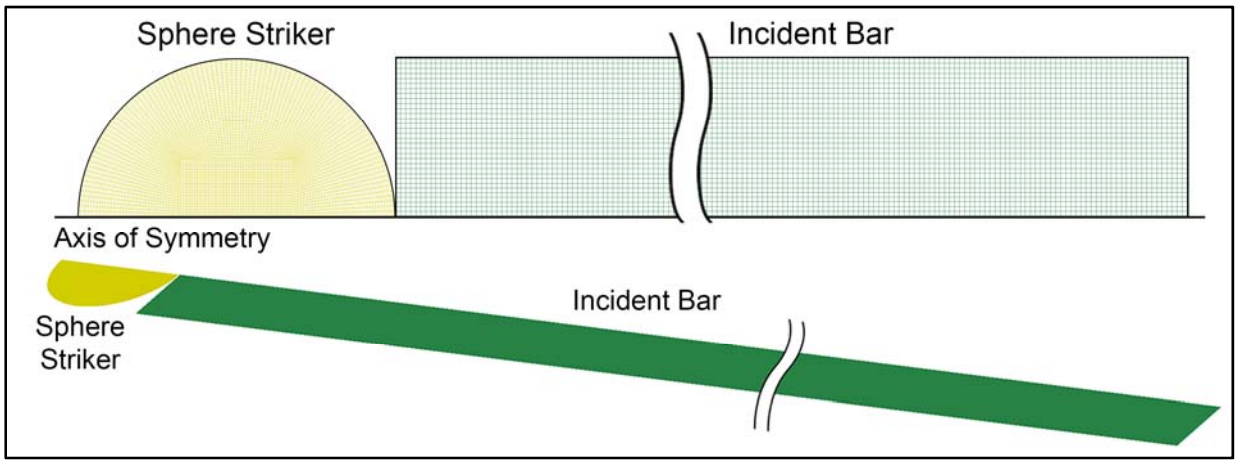

Figure 67. Axisymmetric finite element model of C[3]HB sphere striker and incident bar indicating axis of symmetry and discretization of geometry

Table 9. Optimized PMMA constitutive model parameters

μ_1 (GPa)	3.776	
α_1	1	

G_1 (GPa)	0.0065	**β_1**	0.001
G_2 (GPa)	0.0492	**β_2**	4.79
G_3 (GPa)	0.0418	**β_3**	29.0
G_4 (GPa)	0.1353	**β_4**	12840

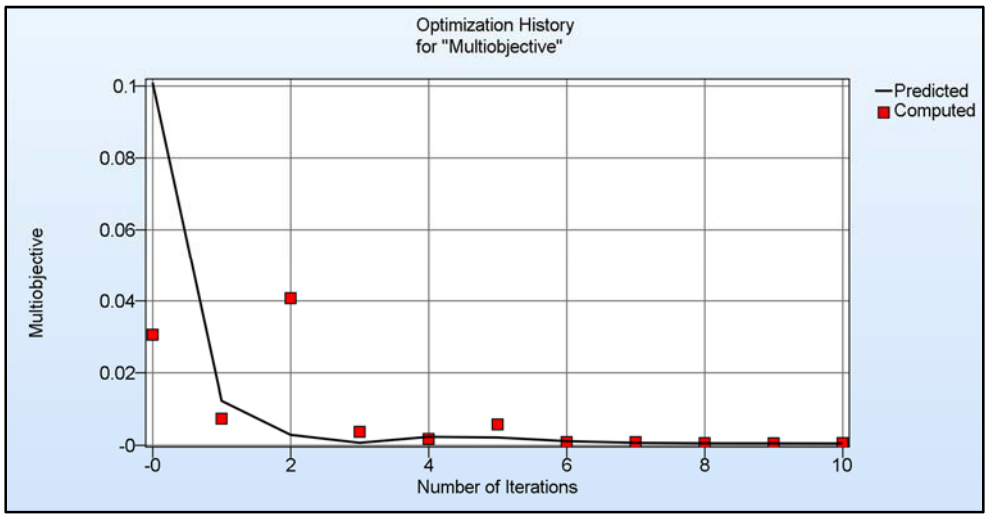

Figure 68. Convergence of the PMMA material optimization

The PMMA properties from Table 9 were validated with the remaining benchmark tests (§ 4.4.2). The average striker velocities of the remaining benchmark test repeats were calculated resulting in 8 striker conditions and were simulated (Table 10). The simulated incident bar strain and free–end velocity were compared to the average incident bar strain and free–end velocity for each condition showing good agreement (Figure 69). Cross–correlation analysis was performed between the simulated and measured incident bar strain and free–end velocity data of the 8 striker conditions resulting in excellent agreement with ratings ranging from 0.970–0.997 (Table 11). The excellent agreement of the results indicates that the numerical model can effectively predict the wave propagation in the C^3HB acrylic incident bar at varying striker velocities and types.

Table 10. Striker impact velocity of the benchmark tests performed in section 4.4.2

Striker Type	Striker Velocity (m/s)	Averaged Velocity (m/s)
Short	4.770	4.82**
	4.791	

	4.898	
	6.235	6.24**
	6.220	
	6.269	
	7.091	7.07**
	7.043	
	7.063	
Long	4.609	4.58**
	4.585	
	4.551	
	5.563	5.55**
	5.553	
	5.535	
	6.686	6.64**
	6.598	
	6.645	
Sphere	7.554	7.57**
	7.578	
	9.168*	9.13
	9.119	
	9.110	
	10.330	10.36**
	10.380	
	10.380	
* Experimental test used for optimization model ** Experimental tests used for model validation		

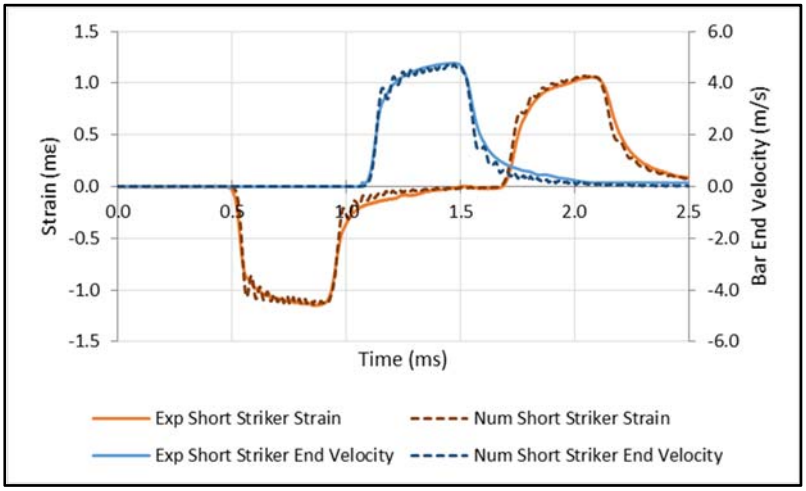

Figure 69. Numerical results compared to averaged experimental results for incident bar strain and free–end velocity with the long striker average impact velocity of 4.58 mm/ms

Table 11. Cross–correlation ratings of numerical versus experimental results for incident bar strain and free–end velocity

Measurement Data	Striker Type	Cross–correlation rating
Strain Data	Short	0.988
	Long	0.970
	Sphere	0.997
Free–End Velocity	Short	0.984
	Long	0.990
	Sphere	0.993

4.5.3 C^{3}HB Numerical model Validation

The developed PMMA material model was used for both the incident bar and chamber acrylic materials, and a validation process was performed for the full apparatus model. Twenty–seven new experimental tests were undertaken using the sphere striker, incident bar, and chamber filled with distilled water (chamber tests). The chamber tests were performed at varying firing–pressures with differing chambers (3 repeats of 3 firing–pressures for 3 chambers). Cross–correlation was performed on the initial compressive (negative strain) phase of the measured and simulated chamber strain data for the 27 chamber tests. The initial compressive phase, occurring between ~1.1–1.25 ms in simulation time (Figure 70), was chosen because it was the principal feature in the chamber strain data. The cross–correlation resulted in a good agreement with an average rating of 0.921. Cavitation of the distilled water was observed in most of the 27 chamber tests at high firing–pressures; however, the strain data measured showed no significant differences between cavitating and non–cavitating tests. Therefore it was concluded that the numerical model was effective in predicting the dynamics of the incident bar and chamber throughout a test until after the initial compressive phase of chamber strain at 1.25 ms (Figure 70).

Full experimental strain and chamber–end velocity data of a non–cavitating test was simulated with the numerical model (Figure 70). There was excellent agreement between the arrival times, rise, and peak values between the experiment and simulation for the incident bar strain, chamber strain, and chamber–end velocity traces. The differences in the chamber strains observed after the initial compressive phase at 1.25 ms could be attributed to the complex wave

reflections. The slight differences in the timing and rise of the reflected wave can be attributed to the use of a coupling agent in the experiment that was not implemented in the model transferring a small amount of tension resulting in a delay of separation between the incident bar and chamber, effectively increasing its magnitude and decreasing its rise–time.

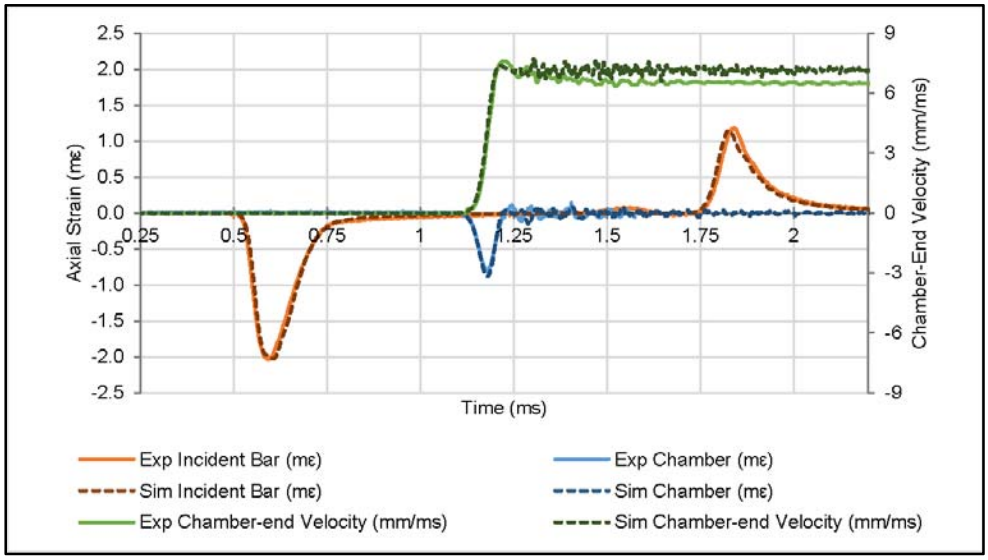

Figure 70. Experiment (Exp) and numerical (Sim) incident bar strain and chamber–end velocity traces for a single non–cavitating chamber test with a sphere striker impact velocity of 9.35 mm/ms

High–speed images of a cavitating test was compared to the water pressure contours predicted in a simulation. It was predicted that the largest negative pressure occurs uniformly within the entire region adjacent to the back–wall surface (thickness of ~2 mm) without large variations in the radial direction (Figure 71). Therefore, cavitation was expected to occur locally within the back–wall region fulfilling the fifth requirement of the apparatus development, and bubbles initiating at multiple locations within this region were considered within the criterion of a cavitating event.

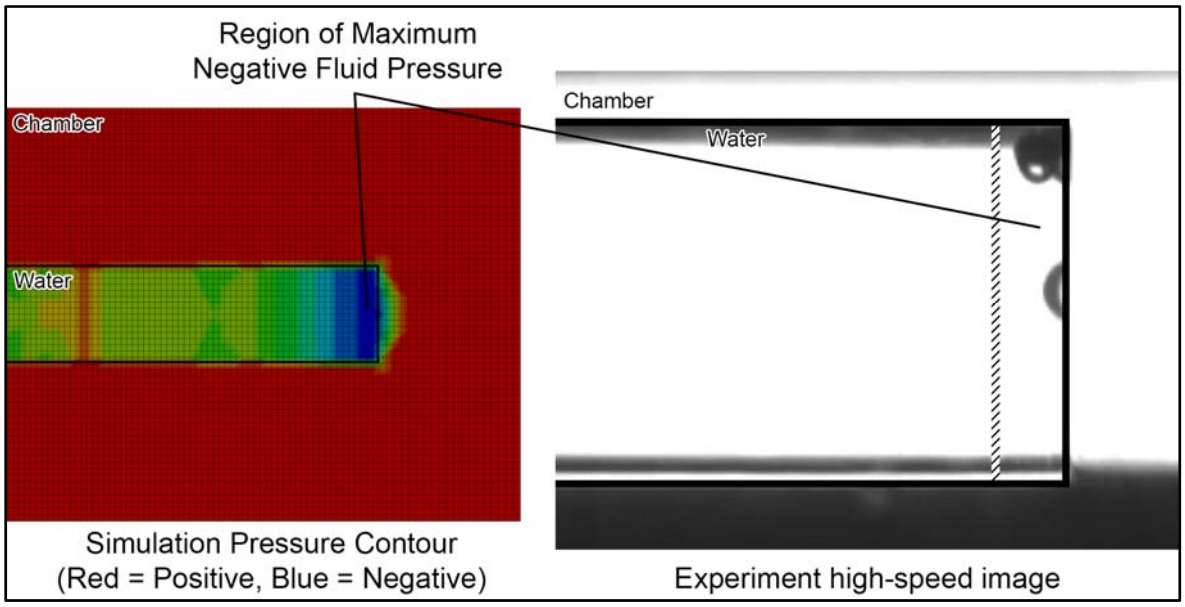

Figure 71. Region of maximum negative fluid pressure identified from the simulation compared to location of cavitation

Timing of cavitation was investigated using high–speed imaging coupled with simulated back–wall pressure. Analysis of the high–speed images showed that the start of the bubble growth occurred at time ~t1 (Figure 72). The bubble continued its growth until ~t2 where it reached its maximum volume, and then finally collapsing at ~t3. The initiation corresponded to the onset of the negative pressure. Likewise, maximum volume corresponded to the time of the peak negative pressure and collapse corresponded to the time of the following peak compressive pressure; however, it should be noted that the inertial effects of the bubble growth and collapse may have an effect on the timing in specific cases. Overall, it has been demonstrated that the timing of the bubble growth and collapse agreed with the pressure traces predicted by the numerical model with cavitation initiating just after 1.1 ms and collapsing just before 1.25 ms. The differences between the experimental and simulated results previously discussed in the reflected wave strain, and chamber strain, were all observed occurring after ~1.25 ms. Therefore the differences was justified as negligible to the generation of cavitation, and it was concluded that the numerical model can predict the dynamics of the full C^3HB apparatus with excellent agreement before 1.25 ms corresponding to the time after initial cavitation bubble collapse.

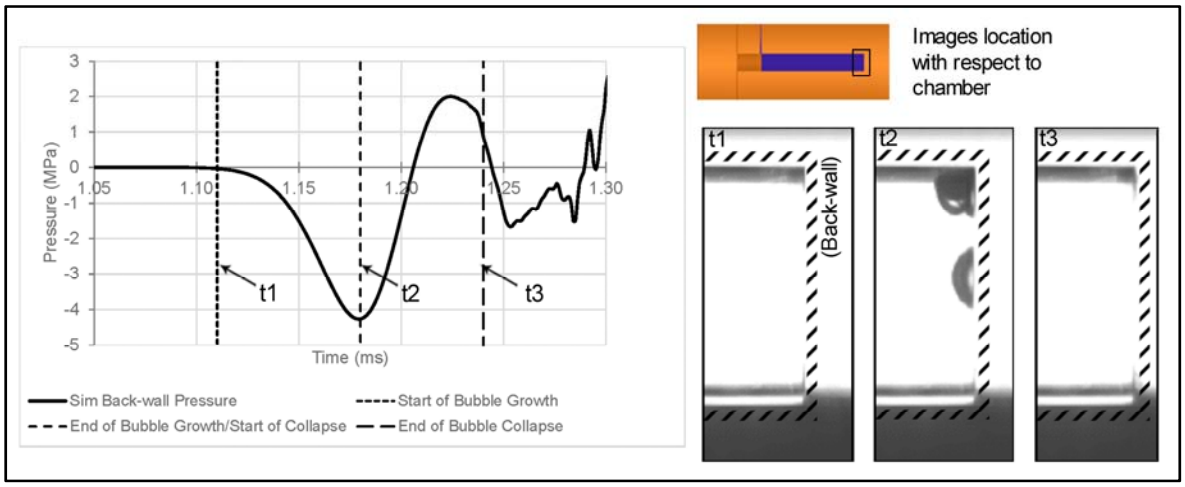

Figure 72 Timing of bubble (circled) growth and collapse using high–speed video coupled with simulated back–wall pressure

To verify the ability of the apparatus to reproduce negative pressures observed in the head during blast exposure, the back–wall pressure trace simulated from the C^3HB–4 and the occipital region CSF ICP from the sagittal blast head model [39] was compared (Figure 73). The peak negative ICP of CSF from a 3 m stand–off, 5 kg C4 explosive charge at a 1.5 m height burst was matched using the C^3HB numerical model for verification of the pressure traces. The negative pressure at the back–wall of the C^3HB model showed good agreement with the negative ICP of CSF from the head model; fulfilling the first requirement of the apparatus development. Similarly, the rate (rise) of the incident pressure wave in the incident bar showed good agreement with the rate of the primary pressure wave at the frontal region of the head (§ 4.3.1).

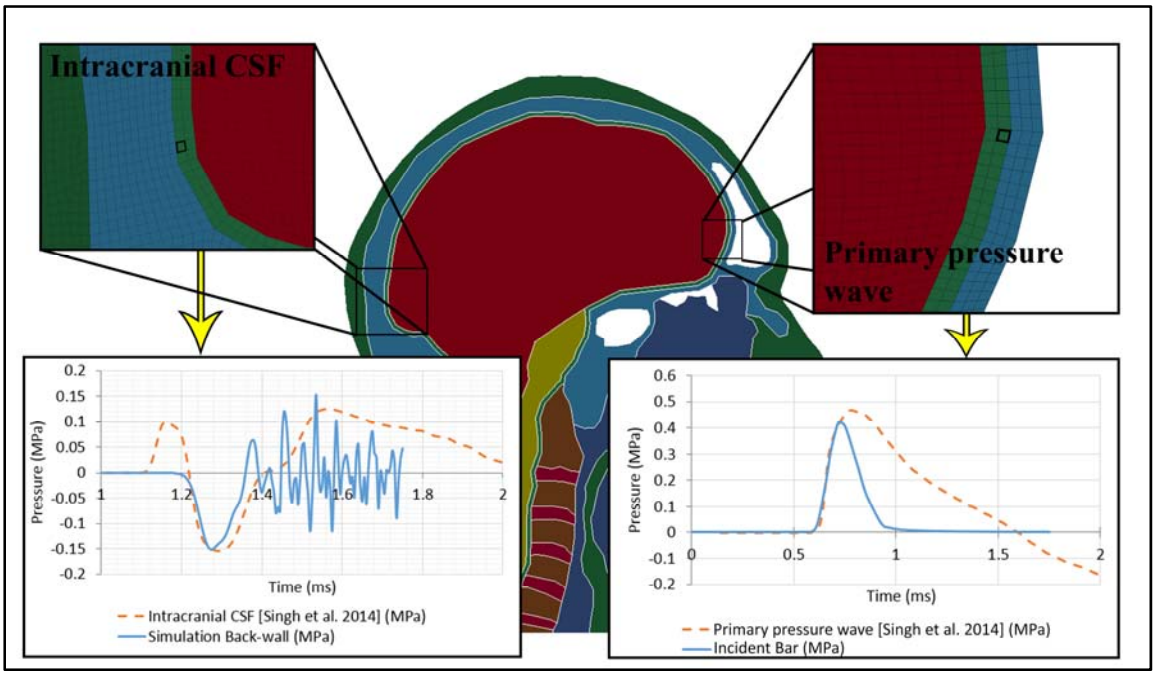

Figure 73. Intracranial pressure comparison with predicted pressures from the apparatus for 3m stand–off blast exposure of 5kg C4; Simulation performed using sagittal head model developed by Singh et al. [39]

4.5.4 Mesh Refinement Study

A mesh refinement study was performed using 4 different mesh sizes with increasing grid size by halving the previous mesh size (Table 12). The meshes were compared by performing simulations with a striker impact velocity of 9.0 mm/ms. Five metrics were obtained from the simulations for the refinement study: the peak incident strain wave, the chamber strain, the incident and back–wall fluid pressure, and the chamber–end velocity (Figure 74).

Table 12. Mesh refinement average grid sizes and simulation runtimes

Mesh Description	Average Grid Spacing (mm)	Runtime (min)
Coarser (f_4)	1.604	1.5
Coarse (f_3)	0.791	12.5
Medium (f_2)	0.396	97
Fine (f_1)	0.198	825

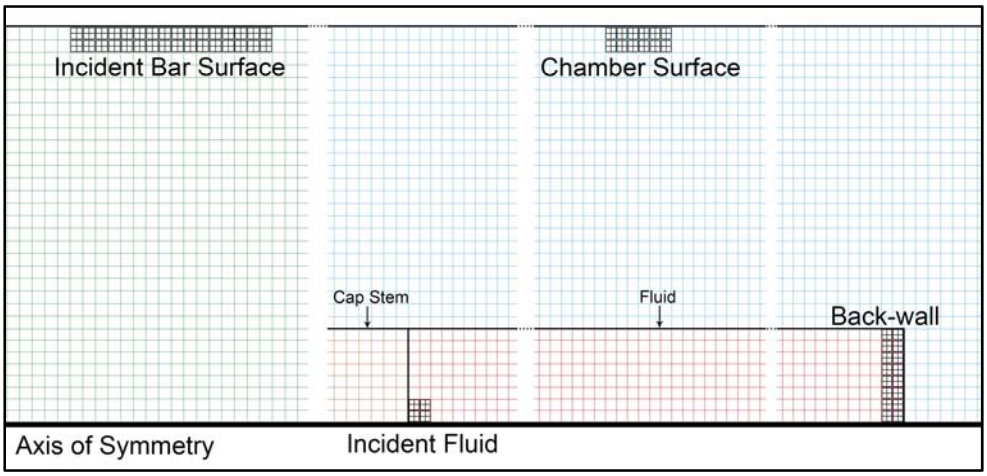

Figure 74. Metrics (elements) chosen in the incident bar, chamber, and fluid for the mesh refinement study

The metric values for each mesh size are shown in Figure 75, Figure 76, and Figure 77, with their f_0 values indicated with square markers. The f_0 values for the peak incident strain wave and chamber–end velocity could not be calculated due to their non–convergence. An explanation for their non–convergence could be that the peak value was already in the convergence zone and was over–converging due to round–off errors. Another explanation could be that the high frequency oscillations induced by the radial inertia oscillations produced complex interaction with the peak of the signal affecting its convergence [184]. As a secondary metric for the incident strain wave, the leading values at the end of the incident strain wave rise were used and resulted in converging values (Figure 75). The leading values were chosen as a second metric because the two issues noted above are less prominent in the rise versus the peak of the signal. As a secondary metric for the chamber–end velocity, the slopes of their linear rise were used and resulted in converging values (Figure 78). The slopes were chosen as a second metric because the acceleration of the chamber–end was significant to the determination of the back–wall pressure (§ 4.3.3.1).

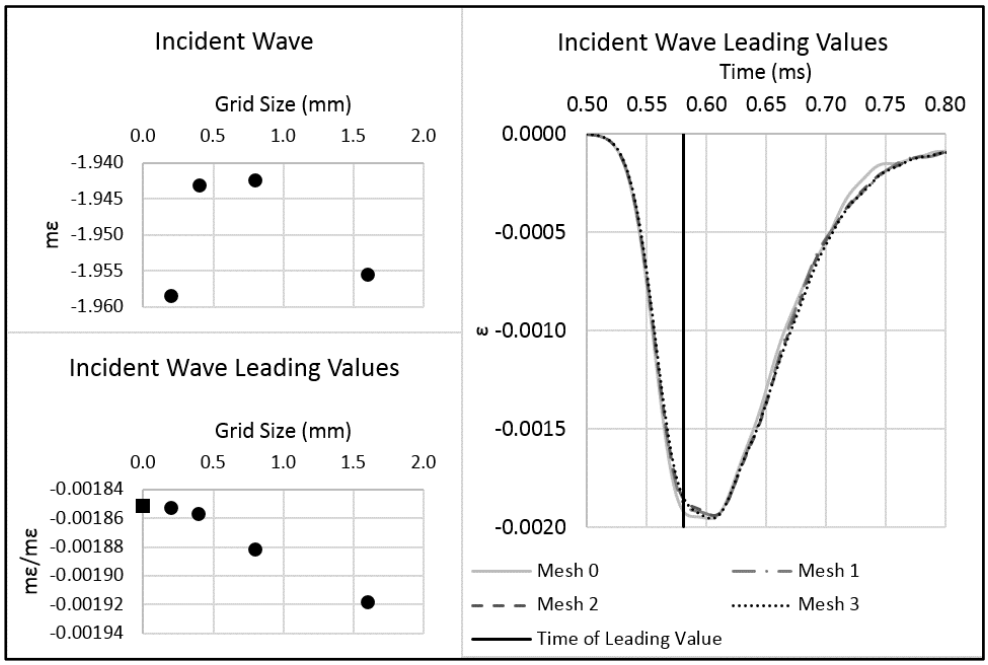

Figure 75. Richardson Extrapolation f_0 value for incident wave and its leading values

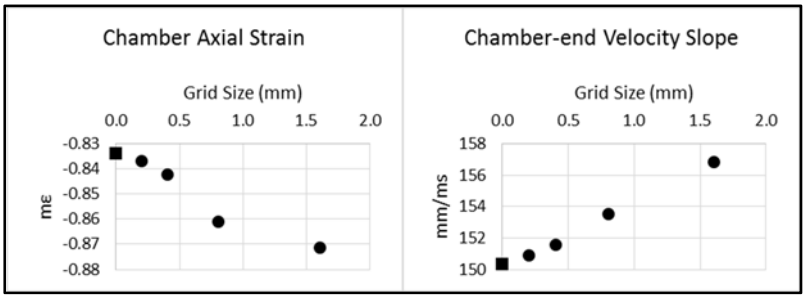

Figure 76. Richardson Extrapolation f_0 value for chamber axial strain and chamber–end velocity

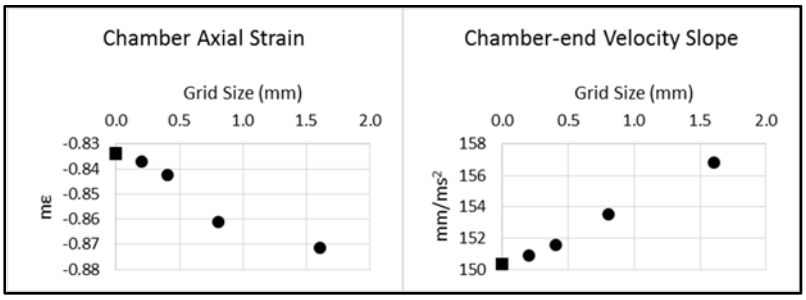

Figure 77. Richardson Extrapolation f_0 value for the back–wall and incident fluid pressure

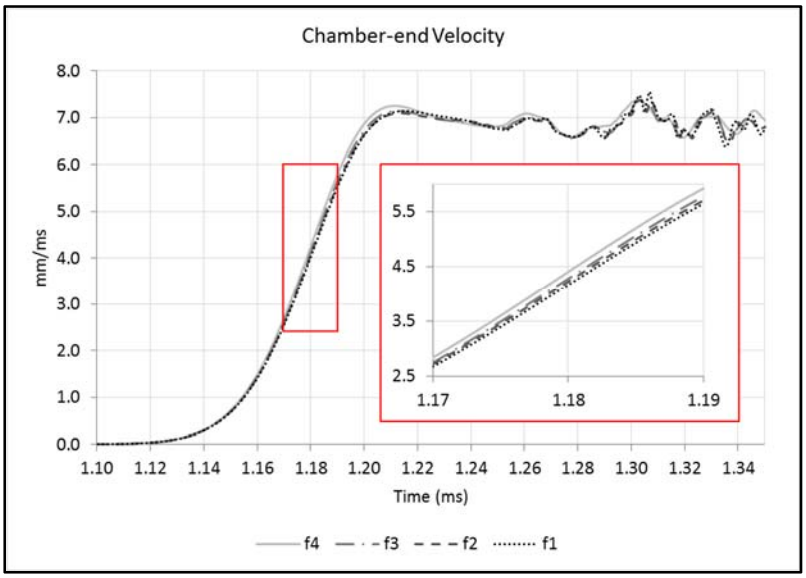

Figure 78. Rise slopes chosen for mesh refinement study of the chamber–end velocity

The converging metrics suggested that the medium mesh was the most desirable having errors less than 2%, compared to their f_0 values, and a runtime significantly less than the fine mesh (Table 13). The standard deviations of the metric values for the simulated mesh sizes (based on population) were also calculated resulting in deviations less than 2% and orders of magnitude less than their f_0 values demonstrating closeness. To further confirm the closeness of the medium mesh, an asymptotic zone–check was also performed (Table 13). As expected, all the metrics result in values relatively close to 0 demonstrating that they are within the asymptotic zone. Therefore it was concluded that the medium mesh was the best mesh size for the apparatus numerical model.

Table 13. Summary of error analysis of metrics used in mesh refinement study

	Incident Strain	**Incident Strain Leading Values**	**Chamber Strain**
Actual Error of f_2	–	0.3%	0.97%
Standard Deviation	0.4%	1.4%	1.6%
Asymptotic zone	–	2.80E–03	6.10E–03
	Back–wall Fluid Pressure	**Incident Fluid Pressure**	**Chamber–end Velocity Slope**
Actual Error of f_2	1.21%	0.61%	0.83%
Standard Deviation	3%	1.5%	1.5%
Asymptotic zone	4.01E–03	7.78E–03	4.029E–03

4.6 Testing Protocol

The following section discusses the process of preparing fluid samples and the dynamics that occurred in the apparatus during cavitation tests. Data processing of the recorded measurements is also discussed demonstrating the generation of a probability sigmoid curve for cavitation used to determine the cavitation pressure threshold.

4.6.1 Chamber and Sample Preparation

Cavitation tests were performed using distilled water (Distilled Water 4 L, Compliments). Agitation of the water produced excessive air bubbles providing unwanted cavitation nuclei, which was also observed by Kenner [102], therefore avoidance of bulk movement of the water was maximized by keeping the water in its original container at all times until the test was undertaken. To further avoid air bubble contamination of the water and ensure uniform temperature, it was allowed to settle for several days at a lab temperature of approximately 21 °C before testing. The water was extracted from its container using a syringe dedicated for transferring the water into the chamber. A syringe was chosen because it allowed precise filling of the chamber with little to no agitation of the water.

Preparation of the chamber and cap began with a thorough cleaning using regular hand soap to remove any grease from handling and previous tests. The inside of the chamber was then thoroughly dried and swabbed with a cotton swab lightly soaked in a dilute isopropyl alcohol and distilled water solution to remove any grease that may have entered the chamber. It was very important that the chamber was completely cleaned of grease and contamination particles, such as dust or cotton fibers, ensuring cavitation nuclei were not introduced. The last step required swabbing the inside of the chamber with a piece of lint–free gauze pad carefully removing any visible contamination as a result of the cleaning process.

Before filling the chamber with distilled water, the inside chamber walls were coated with a very thin film of a wetting agent solution using lint–free gauze. Harvey et al. [185] showed that the addition of a wetting agent to the water did not have an effect of preventing cavitation on hydrophobic surfaces. The thin film was used to reduce the surface tension between the water and walls to ensure complete wetting of the distilled water. The wetting agent solution was made using

25 ml of distilled water mixed with 5–6 drops of the wetting agent (Jet–Dry Rinse Agent, Finish) resulting in a ~1.1 % concentration. The solution was carefully mixed ensuring that the formation of soap bubbles, which could act as cavitation nuclei, was avoided.

The chamber was then carefully filled with distilled water, taking care that there were no bubbles in the chamber. A thin line of Petroleum Jelly (Vaseline) was used as coupling around the base of the cap stem to provide full surface contact between the cap and chamber for wave transmission (Figure 79). During capping, the excess water in the chamber was expelled through the venting channel. Care was taken to ensure that the cap covered the venting channel without compressing the water inside, thus preserving atmospheric pressure. Monitoring a strain gauge (WA–09–120WR–120, Micro–Measurements) installed on the chamber confirmed that there was no appreciable pressure induced in the chamber during installation of the cap. The cap was pressed firmly onto the chamber to ensure that the coupling on the cap squeezed out from the interface, and a thin and evenly spaced film remained. Lastly, the chamber was fully wiped clean to increase visibility of the fluid for high–speed imaging.

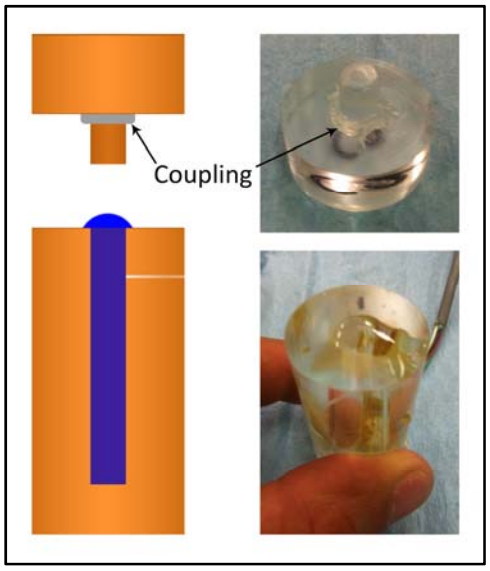

Figure 79. Placement of coupling on the cap stem and water overfill

4.6.2 Wave Propagation and Cavitation Occurrence

The wave propagation of the compressive pulse (incident wave) for the C^3HB apparatus was as follows. After impact of the sphere striker with the incident bar, a compressive pulse (incident wave) was generated in the bar and propagated towards the chamber (Figure 80). This compressive pulse transmitted into the chamber cap ($\sigma_{I(1)}$), through the water ($\sigma_{I(2)}$), and into the chamber end all (σ_T) (Figure 81). Upon reaching the chamber–end, a tensile pulse (chamber reflected wave, σ_R) was produced and transmitted back into the water. The negative pressure at the back–wall region (Figure 71) resulted from the chamber reflected wave superimposing with the trailing–end of the compressive pulse ($\sigma_{I(2)}$). When the superposition of the pulses at the incident bar–chamber cap interface became negative, the bar and chamber separated preventing further wave transmission. The compressive pulse remaining in the incident bar then reflected at its newly–exposed surface as a tensile pulse (incident bar reflected wave). The remaining tensile pulse in the chamber, which caused the separation, also reflects at its newly–exposed surface in compression and continued to reflect back–and–forth within the chamber.

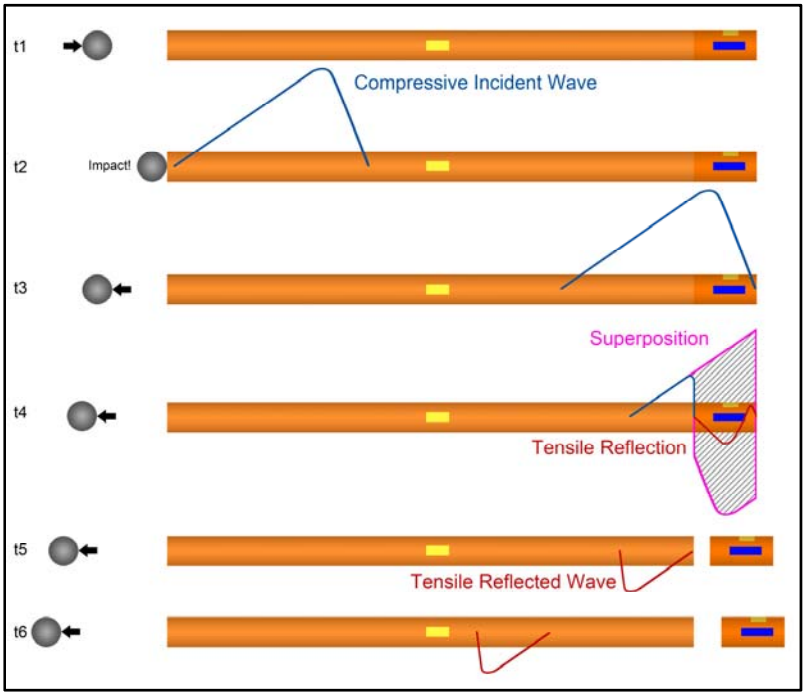

Figure 80. Simplified wave propagation of compressive pulse resulting in the separation of the incident bar and chamber with increasing time (Note that wave propagation in chamber is not shown after time t5)

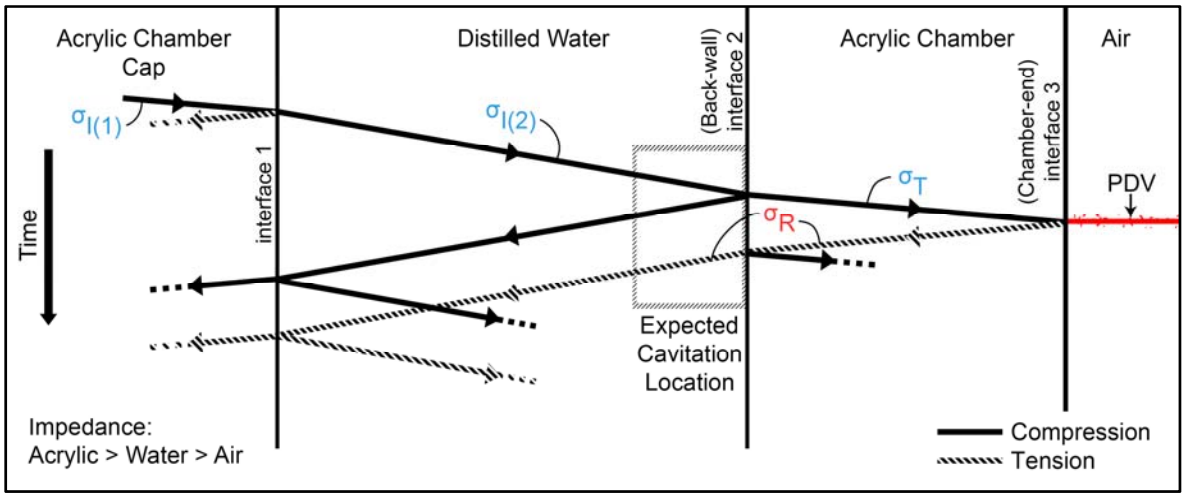

Figure 81. Wave diagram showing propagation through the chamber to produce negative pressure in the distilled water as a result of the impedance differences between acrylic and air

4.6.3 Identification of Cavitation Pressure Threshold

To determine the simulated back–wall pressure in the cavitation tests, simulations were performed with increasing severity to obtain simulated trends of the incident bar strain wave, chamber strain, back–wall pressure, and chamber–end velocity; and as expected all the trends obtained were linear. The linear relationship between the peak simulated incident bar strain wave and peak back–wall pressure was then used with the measured peak incident bar strain wave to obtain the back–wall pressure for each test.

Cavitation is a binary event that does or does not occur. Weaknesses in the fluid demonstrate the probabilistic nature of cavitation in experimental testing (§ 2.3). A large number of test results were required to determine a cavitation pressure threshold that was resilient to errors relating to induced cavitation as a result of unwanted heterogeneous nucleation [98, 108, 109]. Using these back–wall pressures and the occurrence of cavitation as data points, a sigmoid probability curve (ISO/TS 18506) was generated [186]. The sigmoid curve is a theoretical probability curve fit over the cavitation data points demonstrating the probability of cavitation with respect to the back–wall pressure. The pressure corresponding to the 50% probability of cavitation was then considered as the measured cavitation pressure threshold for the set of cavitation tests.

4.7 Chapter Summary

In summary the development of the second and third iteration of the final apparatus were presented to provide full context of issues recognized for generating localized fluid cavitation and measuring fluid pressures. Challenges with generating localized cavitation was observed with the generation of diffuse cavitation in the second and third iterations as a result of unwanted nuclei and inertial–induced fluid volume increase. Challenges with measuring negative fluid pressures were also observed for probe–style (piezoelectric sensor) and catheter–style (piezoresistive sensor) pressure transducers and resulting in the conclusion that the gauges were unable to measure pressures in the negative range with accuracy, and the presence of the gauges introduced cavitation nuclei effectively reducing the cavitation pressure thresholds.

A final apparatus (C^3HB) was developed that could produce localized fluid cavitation through high–rate dynamic loading comparable to head blast exposure. This final apparatus consisted of a steel sphere striker, an acrylic incident bar, and an acrylic confinement chamber. The sphere striker and incident bar combination generated a compressive pulse comparable to that observed transmitted into the head in computational and experimental studies of blast exposure. The chamber was designed with special consideration of testing small fluid volumes, dimensions, and pulse propagation. The back–wall of the chamber was given a thickness comparable to that of the skull, and the cap used to seal the chamber was given a simple design to simplify wave propagation.

A compressive pulse was generated by the sphere striker impact and propagated down the incident bar, transmitted into the chamber and fluid, and reflected in tension at the chamber–end exposed to the atmosphere. This tensile reflection pulse then transmitted back into the water producing negative pressures at the back–wall necessary for cavitation. To verify the dynamics of the final apparatus, strain gauges were used to measure strains in the incident bar and chamber; a PDV was used, in separate occasions, to measure the surface velocity of the incident bar and chamber–end surfaces; a spectral analysis program was used to check wave propagation using measured strain signals; and high–speed imaging and tracking software was used to determine striker impact velocities.

In parallel with the development of the final apparatus, a numerical model was developed to predict the dynamics of the incident bar and chamber. The numerical model was validated using strain and surface velocity measurements of both free–end tests and cavitation tests. Free–end tests were performed with the incident bar at free–end conditions and varying striker types with varying impact velocities. Cavitation tests were performed with the incident bar, three chambers filled with distilled water, and a sphere striker with varying striker velocities. Cross–correlation analysis was performed with the results of both the free–end and cavitation test results demonstrating good agreement between the apparatus and numerical model for varying conditions. Since cavitation was not implemented in the numerical model, the simulations only predicted dynamics before the occurrence of cavitation. Pressure gages were not used in the final apparatus due to their contamination of the water with cavitation nuclei and inability to measure accurate negative pressures. The back–wall pressures, where cavitation was observed, was obtained through simulations and verified with PDV measurements of the chamber–end using one–dimensional approximation that resulted in a good agreement.

Chapter 5. Experimental Cavitation Tests

In this chapter the results of cavitation tests will be presented for distilled water at 21 °C and 37 °C. Cavitation pressure thresholds obtained from generated probability curves for both temperatures are presented, and an investigation on the effect of the chamber back–wall thickness on the back–wall pressure is discussed.

5.1 Distilled Water Results

A series of experimental tests (Table 14) were performed with the C^3HB apparatus using three chambers of the same design (identified as C1, C2, and C3), and localized cavitation was successfully generated for distilled water at 21 °C (Figure 82).

Table 14 Range of peak compressive axial strains measured in the incident bar and chamber for all tests performed

Chamber	Number of Tests Performed	Incident Bar Strain (mε)	Chamber Strain (mε)
C1	28	1.353 – 2.796	0.521 – 1.309
C2	26	1.621 – 2.577	0.679 – 1.326
C3	23	1.455 – 2.781	0.614 – 1.447

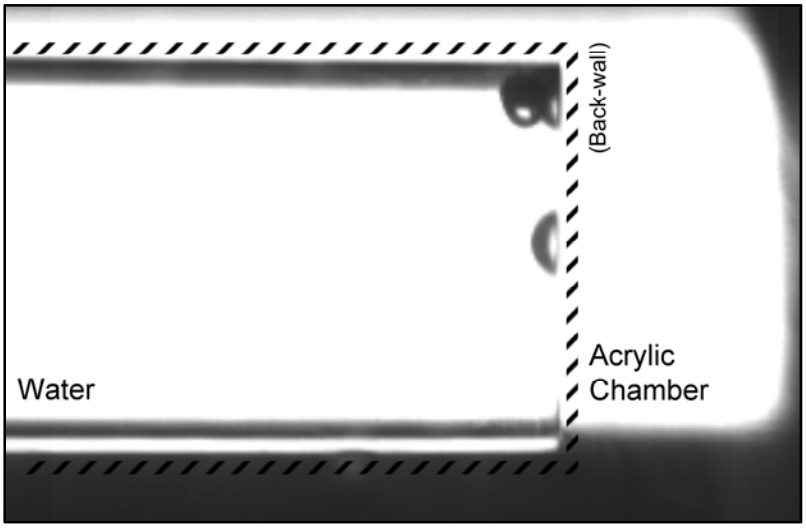

Figure 82. High–speed image of localized cavitation observed at the back–wall region of the chamber

The numerical model was used to simulate each test by matching the simulated and measured incident strain waves. Trends of the experimental and simulated peak chamber strain and chamber–end velocity with respect to the peak incident strain wave were generated to verify agreement between the apparatus and model (Figure 83). Both the experimental and numerical trends showed good agreement with R^2 values of 0.875 and 0.992, respectively. As expected the experimental trends showed linearity below 50% probability of cavitation, since without cavitation, the water in the chamber behaves as a fluid–elastic material. Similarly, the numerical trends showed linearity since the occurrence of cavitation was not implemented in the model (§ 4.5.1).

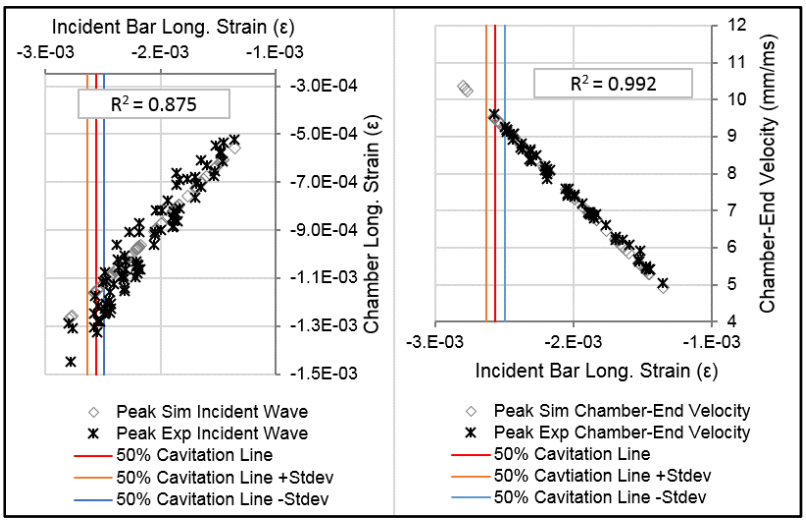

Figure 83. Experimental (Exp) and numerical (Sim) trends of the peak chamber strain and chamber–end velocity with respect to peak incident bar strain.

A trend of the simulated peak negative back–wall pressure with respect to the peak incident strain wave was also generated and verified using the one–dimensional approximation (Equation 72). The calculated and numerical trends showed good agreement with an R^2 value of 0.892 (Figure 84). The calculated trend also shows linearity below the 50% probability line, in agreement with the chamber strain and chamber–end velocity trends (Figure 83).

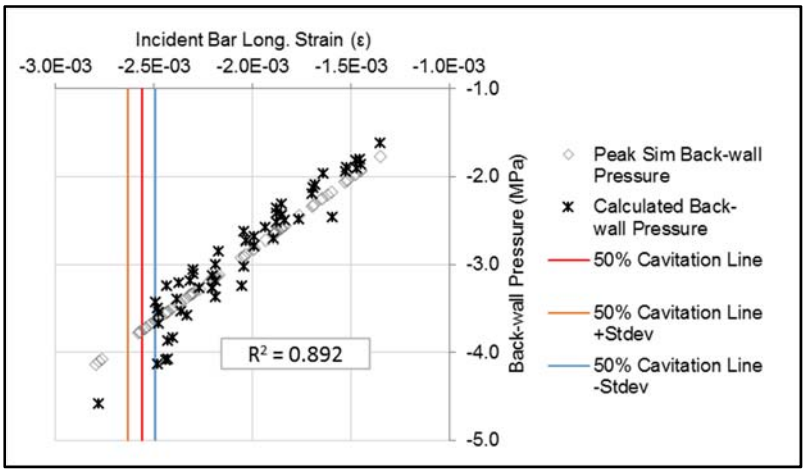

Figure 84. Calculated and numerical (Sim) trends of the peak negative back–wall pressure with respect to peak incident bar strain

Sigmoid probability curves were generated for the three chambers relating the simulated peak negative back–wall pressure with the occurrence of cavitation observed through high–speed imaging (Figure 85). The probability curves showed that for chambers C1, C2, and C3, the cavitation negative pressure threshold (50% probability) was 3.36 MPa ±4%, 3.52 MPa ±6%, and 3.04 MPa ±4%, respectively. The probabilistic nature of the cavitation (§ 2.2) near the threshold may explain the differences between the slope of the curves and more data points are required. Overall, the generated thresholds are in good agreement with each other. Pooling all the chamber data points resulted in a cavitation negative pressure threshold of 3.32 MPa ±3%.

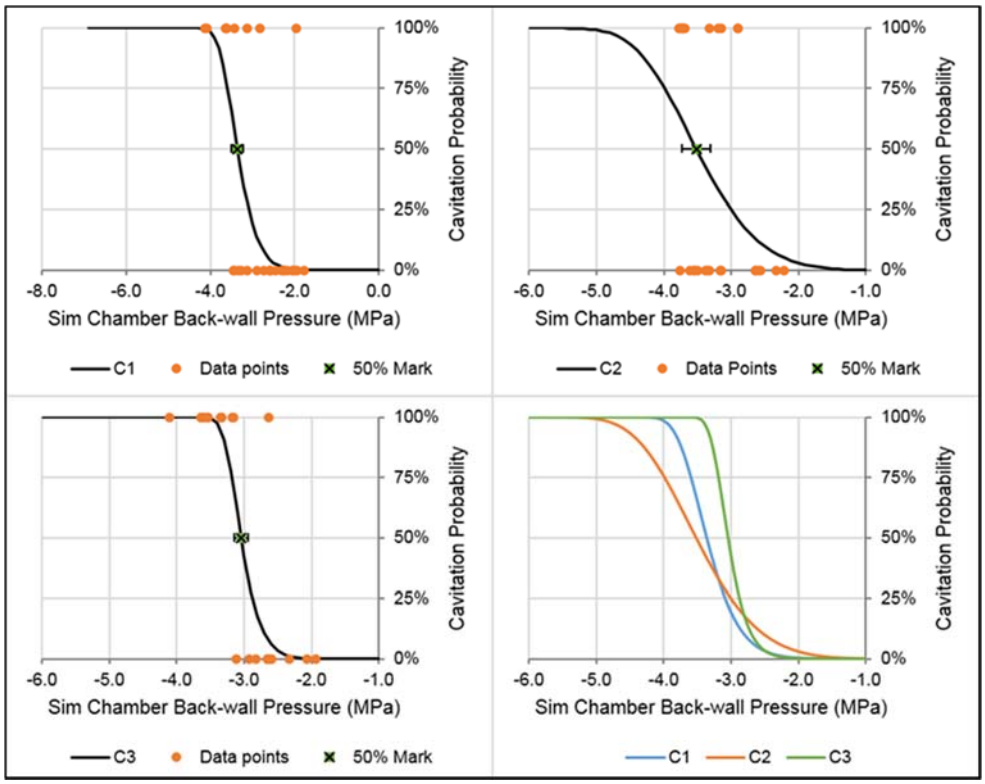

Figure 85. Cavitation probability curves at the back–wall. Top–left: Chamber 1, Top–right: Chamber 2, Bottom–left: Chamber 3, and Bottom–right: Chamber 1 – 3 together

5.1.1 Back–wall thickness Effect

Two other chambers were created with back–wall thicknesses of 7.8 mm (C4) and 8.7 mm (C5), with their other dimensions similar to C1, C2, and C3, which have back–wall thicknesses of 11.3 mm. The trends of peak negative back–wall pressure with respect to incident strain wave were obtained for the different thicknesses within the observed non–cavitating and cavitating pressure range (negative pressures ranging from 2–5 MPa). As expected the trends showed linearity and increasing slope with decreasing thickness; however, the trends showed negligible differences in slope for the three thicknesses considered (Figure 86). This can be explained due to the much larger length of the incident wave compared to the back–wall thicknesses considered, which dominated the propagation and inertial effects of the thicknesses on the fluid pressure. Therefore it was concluded that changes in the back–wall thickness did have an effect on the back–wall fluid pressures, but was negligible due to the dominating of the propagating incident wave. Lastly, it

was also concluded that the change in back–wall thickness did not have a direct effect on the occurrence of cavitation, and therefore did not affect the cavitation probability curves.

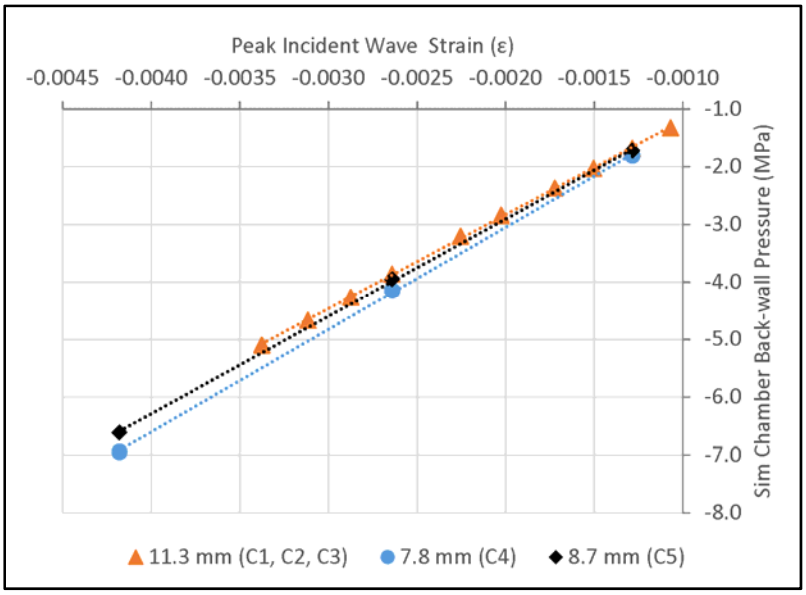

Figure 86. Simulated back–wall pressure with increasing incident strain wave for varying back–wall thickness

Cavitation tests were performed (n=20) with distilled water at 21 °C using chamber C4, resulting in a comparable probability curve to C1, and a cavitation negative pressure threshold of 3.57 MPa ±3% (Figure 87). Since the thresholds for chambers C1, C2, and C3 were also from distilled water at 21°C, and it was concluded that back–wall thickness did not affect the probability curve, the measured threshold for distilled water at 21 °C was updated by pooling all the data points from C1–4 (C1, C2, C3, and C4) resulting in a negative threshold of 3.39 MPa ±2%. This threshold is comparable with the values reported by Kenner (2.96 MPa and 3.09 MPa [102]) for distilled water, and the lower bound reported by Williams (4.5 MPa [140]) for 'nuclear–grade' deionized water; which is expected due to the greater purity of 'nuclear–grade' deionized water compared with distilled water. The variability of other reported dynamic techniques (§ 3.1) varied between 5–10% [112, 113, 134, 140]. Further, of the dynamic methods discussed, only the Tube–Arrest method by Williams et al. [134] visually identified cavitating events. The cavitating events reported by Williams also occurred initiating from a solid surface, with a single test initiating within the body of the liquid. However, cavitation within the body of the liquid may have been a

particular occurrence due to the reported uncertainty of 10%. The proposed C^3HB apparatus provides an important contribution for studying fluid cavitation under controlled and repeatable conditions since this apparatus was able to generate negative fluid pressures similar to that observed in the head during blast exposure, demonstrated visual identification of cavitation, and measured cavitation pressure threshold with a standard deviation of 2%.

Recall Equation 3 used to estimate the critical nucleus radius that would result in fluid rupture (§ 2.2). Using the negative threshold of 3.39 MPa (ΔP) and the typical surface tension of 0.0726 N/m for water at 21 °C, results in a critical radius (R_{CR}) of 0.043 µm. This estimated critical radius is comparable to the 0.05-micron (µm) alumina powder that was used to polish the chamber cavity surfaces (§ 4.3.2). Since the typical surface tension of water was used for the calculations, the critical radius of 0.043 µm is an upper bound estimate for the experimental tests performed, whereas if the lesser surface tension of the wetting agent solution was used, the critical radius would be expected to decrease.

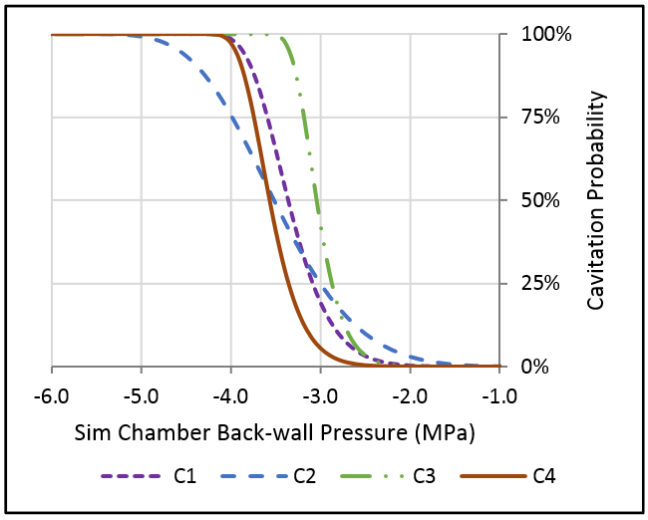

Figure 87. Cavitation probability curve of distilled water at 21 °C with chambers C1, C2, C3 (11.3 mm thickness), and C4 (7.8 mm thickness)

5.1.2 Temperature Effect

It was previously discussed that the cavitation pressure threshold would decrease as a result of an increase in fluid temperature (§ 2.2). With the prospect of testing CSF cavitation, it was

desirable to determine thresholds at body temperature (37 °C) and observe the effects of temperature increase on the threshold. Cavitation tests were performed (n=15) with distilled water at 37 °C using chamber C5 resulting in a probability curve comparable to C1 and C3 and a negative threshold of 3.20 MPa ±5% (Figure 88). A one–tailed T–test was performed between the threshold for C5 (–3.2 MPa) and the 4 thresholds for C1–4 (–3.36, –3.52, –3.04, –3.57 MPa), resulting in the C5 threshold being significantly less than the C1–4 thresholds at a significance level of 12%. However, a significance level of 12% was considered too high, and the hypothesis was rejected. The lack of evidence could be attributed to the lack of threshold measurements at 37 °C, the variability of the thresholds at 21 °C dominating the effect, or the small reduction of the surface tension ($\Delta\gamma$ = –0.0025 N/m) of water at 21°C (0.0726 N/m) to 37 °C (0.0701 N/m) [105].

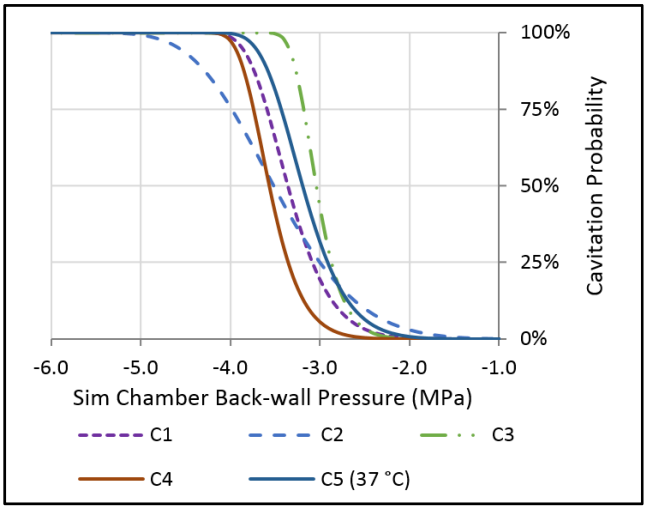

Figure 88. Cavitation probability curve comparison of C5 at 37 °C with chambers C1, C2, C3, and C4 at 21 °C

5.1.3 C^{3}HB Apparatus Limitation

A limitation of the C^{3}HB apparatus was the generation of heterogeneous cavitation. In most of the tests yielding cavitation, bubbles were observed initiating from the back–wall suggesting heterogeneous nucleation; however, some tests showed bubbles initiating adjacent to the back–wall still within the region of maximum negative pressure (Figure 71). Due to the single high–speed camera setup, it could not be concluded whether the bubbles initiating adjacent to the back–wall was the result of heterogeneous or homogeneous nucleation. The low variability of the

cavitation pressure thresholds measured suggests that all cavitating events observed occurred as a result of heterogeneous cavitation, and the fluid tensile strength of distilled water was not exceeded. However, this limitation is considered minor since the *in vivo* conditions of cavitation within the head during blast exposure is currently unknown in the literature.

5.2 Chapter Summary

In summary, cavitation negative pressure thresholds of 3.39 MPa ±2% was obtained for distilled water at 21 °C using combined data points from chambers C1, C2, C3, and C4, and 3.20 MPa ±5% for distilled water at 37 °C using chamber C5. It was concluded that the back–wall thicknesses considered (7.8, 8.7, 11.3 mm) did have an effect on the back–wall fluid pressure, but was considered negligible due to the much larger length of the incident wave (compared to the thicknesses) dominating this effect. Additionally, the back–wall thickness did not affect the occurrence of cavitation with respect to back–wall pressure, concluding that the back–wall thickness did not affect the cavitation probability curve. Lastly, a one–tailed T–test performed between the thresholds measured for distilled water at 21 °C and 37 °C concluded that the 37 °C threshold was significantly lesser than the 21 °C thresholds at a significance level of 12%. However, a significance level of 12% was considered too high, and the hypothesis was rejected.

Chapter 6. Conclusions

This section presents conclusions made within the scope of the thesis and limitations of the C^3HB apparatus and numerical model developed. Dynamic techniques developed for generating fluid cavitation with the aim of determining fluid tensile strengths and investigating cavitation dynamics exist, but none developed with the aim to studying cavitation pressure thresholds of fluids within conditions of head blast exposure. This thesis demonstrates primary contributions to the knowledge of blast–related cavitation through:

1. The development of an apparatus (C^3HB) that can generate localized fluid cavitation as a result of dynamic loading with a tensile pulse produced from the reflection of a compressive pulse (§ 4.5.3) having a comparable shape and rate to the primary pressure wave transmitted into the brain during head blast exposure (§ 4.3.1)
2. Verification of the inability to measure fluid pressures in the negative (tensile) range of a piezoelectric probe–style pressure transducer (PCB Piezotronics Model 113B21, sampling rate of 2 MHz). This challenge was addressed using a numerical model that could predict the positive pressure ranges in good agreement with measured fluid pressures (§ 4.2.2).
3. The observation of fluid cavitation occurring as a result of nuclei from the presence of a pressure transducer and the geometric discontinuities associated with transducer implementation, which effectively reduced the cavitation pressure thresholds observed (§ 4.2.2). Nuclei contamination was observed using both probe–style (piezoelectric sensor) and catheter–style (piezoresistive sensor) transducers, at both the surfaces of the transducers, and geometric changes to the chamber because of their mounting (§ 4.3.3.2).
4. Development, verification, and validation of a numerical model that predicts the response of the apparatus, such that the fluid pressure changes can be obtained without the use of intrusive measurement gages, which was demonstrated to reduce the cavitation pressure thresholds observed (§ 4.5).
5. Investigation of the effect of chamber back–wall thicknesses of 11.3, 8.7, and 7.8 mm on the back–wall fluid pressure, concluding negligible effect compared to the compressive pulse severity (§ 5.1.1). Consequently, the sigmoid curve generated for C4 (thickness of

7.8 mm at 21 °C) was comparable to the three sigmoid curves generated for C1, C2, and C3 (thickness of 11.3 mm at 21 °C).

6. Measurement of the cavitation negative pressure threshold of 3.39 MPa ±2% for distilled water at 21 °C (§ 5.1.1) by generating a sigmoid curve with the combined data points from tests using C1, C2, C3, and C4.
7. Measurement of the cavitation negative pressure threshold of 3.20 MPa ±5% for distilled water at 37 °C (body temperature), which was significantly less than the 21 °C thresholds at a significance level of 12% (§ 5.1.2).

6.1 Recommendations

The recommendations for further work corresponding to the motivations of the study and potential for the apparatus are as follows:

1. Heterogeneous cavitation was observed occurring at the back–wall of the chamber for all tests performed. Investigation of the chamber cavity surface roughness should be performed to determine its effect on the measure cavitation pressure threshold.
2. The effects of fluid temperature and chamber back–wall thickness were investigated with only a single cavitation probability curve each case. Additional cavitation tests should be performed to generate more pressure threshold for each case to produce a full understanding on their effects.
3. The inability of the probe–style and catheter–style pressure transducers to measure pressures in the negative range was observed and verified using a numerical model. The potential of the apparatus as a technique for verifying pressure gauge capabilities within a specific negative pressure domain should be further explored.
4. The nuclei contamination of the fluid sample from the presence of pressure gauges and the geometric discontinuities from their implementation resulted in a decrease in the cavitation pressure thresholds observed. Methods to avoiding or minimizing the effect of pressure gauges and their implementation should be further explored.
5. The goal of the final apparatus was to generate fluid cavitation as a result of loading similar to that observed in head blast exposure. It has been observed that large localized

pressures occur as a result of cavitation bubble collapse (§ 2.4). Therefore, a method to use the apparatus as a way to investigate the effects (stresses and strains) produced on solid samples as a result of cavitation bubble collapse should be further explored. Such a method could lead to knowledge that directly links cavitation as an injury mechanism for mTBI.

References

1. Hoge CW, McGurk D, Thomas JL, et al (2008) Mild Traumatic Brain Injury in U.S. Soldiers Returning from Iraq. N Engl J Med 358:453–463. doi: 10.1056/NEJMoa1109400
2. iCasualties. http://www.icasualties.org. Accessed 1 Jan 2016
3. Owens BD, Kragh JF, Wenke JC, et al (2008) Combat wounds in operation Iraqi Freedom and operation Enduring Freedom. J Trauma 64:295–9. doi: 10.1097/TA.0b013e318163b875
4. Wojcik BE, Stein CR, Bagg K, et al (2010) Traumatic brain injury hospitalizations of U.S. army soldiers deployed to Afghanistan and Iraq. Am J Prev Med 38:S108–S116. doi: 10.1016/j.amepre.2009.10.006
5. Connolly TJM, Clutter JK (2010) Criteria to determine likelihood of brain injury during explosive events. Saf Sci 48:1387–1392. doi: 10.1016/j.ssci.2010.05.013
6. Scherer MR, Weightman MM, Radomski M V, et al (2013) Returning service members to duty following mild traumatic brain injury: exploring the use of dual-task and multitask assessment methods. Phys Ther 93:1254–67. doi: 10.2522/ptj.20120143
7. Dretsch MN, Silverberg ND, Iverson GL (2015) Multiple past concussions are associated with ongoing post-concussive symptoms but not cognitive impairment in active-duty Army soldiers. J Neurotrauma 6:1–6. doi: 10.1089/neu.2014.3810
8. Bryant R (2011) Post-traumatic stress disorder vs traumatic brain injury. Dialogues Clin Neurosci 13:251–262.
9. Rosenfeld J V., McFarlane AC, Bragge P, et al (2013) Blast-related traumatic brain injury. Lancet Neurol 12:882–893. doi: 10.1016/S1474-4422(13)70161-3
10. Vasterling JJ, Verfaellie M, Sullivan KD (2009) Mild traumatic brain injury and posttraumatic stress disorder in returning veterans: Perspectives from cognitive neuroscience. Clin Psychol Rev 29:674–684. doi: 10.1016/j.cpr.2009.08.004
11. Harrigan TP, Roberts JC, Ward EE, Merkle AC (2010) Correlating tissue response with anatomical location of mTBI using a human head finite element model under simulated blast conditions. IFMBE Proc 32 IFMBE:18–21. doi: 10.1007/978-3-642-14998-6_5

12. Songer T (2001) Measuring Injury Severity A brief introduction. 1–38.
13. Carroll CP, Cochran J a, Price JP, et al (2010) The AIS-2005 Revision in Severe Traumatic Brain Injury: Mission Accomplished or Problems for Future Research? Ann Adv Automot Med 54:233–8.
14. Grujicic M, Arakere G, He T (2010) Material-modeling and structural-mechanics aspects of the traumatic brain injury problem. Multidiscip Model Mater Struct 6:335–363. doi: 10.1108/15736101011080097
15. Meaney DF, Smith DH (2014) Concussion in Sports Biomechanics of Concussion. Clin Sports Med 30:19–31. doi: 10.1016/j.csm.2010.08.009
16. Schmitt K-U, Niederer PF, Cronin DS, et al (2014) Trauma and Biomechanics, 4th ed. doi: 10.1007/978-3-662-05448-2
17. Fournier E, Sullivan D, Bayne T, et al (2007) Blast headform development - Literature review.
18. Ouellet S, Bir C, Bouamoul A (2014) Direct comparison of the primary blast response of a physical head model with post-mortem human subjects.
19. Ouellet S, Bouamoul A (2012) A Blast Headform Surrogate for the Assessment of Blast-Induced Traumatic Brain Injury. CTTSO/TSWG/PPE Symp.
20. Grujicic M, Bell WC, Pandurangan B, Glomski PS (2011) Fluid/Structure interaction computational investigation of blast-wave mitigation efficacy of the advanced combat helmet. J Mater Eng Perform 20:877–893. doi: 10.1007/s11665-010-9724-z
21. Nyein MK, Jason AM, Yu L, et al (2011) Correction for Nyein et al., In silico investigation of intracranial blast mitigation with relevance to military traumatic brain injury. Proc Natl Acad Sci U S A 108:433. doi: 1018365108 [pii]\r10.1073/pnas.1018365108
22. Zhang L, Makwana R, Sharma S (2013) Brain response to primary blast wave using validated finite element models of human head and advanced combat helmet. Front Neurol 4 AUG:88. doi: 10.3389/fneur.2013.00088
23. Sarvghad-Moghaddam H, Jazi MS, Rezaei A, et al (2015) Examination of the protective roles of helmet/faceshield and directionality for human head under blast waves. Comput Methods Biomech Biomed Engin 18:1846–55. doi: 10.1080/10255842.2014.977878

24. Moss WC, King MJ, Blackman EG (2009) Skull flexure from blast waves: A mechanism for brain injury with implications for helmet design. Phys Rev Lett 103:4–7. doi: 10.1103/PhysRevLett.103.108702
25. Ganpule S, Gu L, Alai a., Chandra N (2011) Role of helmet in the mechanics of shock wave propagation under blast loading conditions. Comput Methods Biomech Biomed Engin 5842:1–12. doi: 10.1080/10255842.2011.597353
26. Mac Donald CL, Johnson AM, Cooper D, et al (2011) Detection of Blast-Related Traumatic Brain Injury in U.S. Military Personnel. N Engl J Med 364:2091–2100.
27. Ryu J, Horkayne-Szakaly I, Xu L, et al (2014) The problem of axonal injury in the brains of veterans with histories of blast exposure. Acta Neuropathol Commun 2:153. doi: 10.1186/s40478-014-0153-3
28. G.B. E, T. O, S. N, et al (2016) Primary Blast Exposure Increases Hippocampal Vulnerability to Subsequent Exposure: Reducing Long-Term Potentiation. J Neurotrauma 33:1901–1912. doi: 10.1089/neu.2015.4327
29. Iii EV, Villacorta J, Bass CR, et al (2014) Primary blast injury erases long term potentiation in rat brain organotypic hippocampal slices. 821–822.
30. Pham N, Sawyer TW, Wang Y, et al (2015) Primary blast-induced traumatic brain injury in rats leads to increased prion protein in plasma: a potential biomarker for blast-induced traumatic brain injury. J Neurotrauma 32:58–65. doi: 10.1089/neu.2014.3471
31. Gupta RK, Przekwas A (2013) Mathematical models of blast-induced TBI: Current status, challenges, and prospects. Front Neurol 4 MAY:1–21. doi: 10.3389/fneur.2013.00059
32. Bir C (2011) Measuring Blast-Related Intracranial Pressure Within the Human Head. 1–24.
33. Ganpule S, Alai A, Plougonven E, Chandra N (2013) Mechanics of blast loading on the head models in the study of traumatic brain injury using experimental and computational approaches. Biomech Model Mechanobiol 12:511–531. doi: 10.1007/s10237-012-0421-8
34. Goeller J, Wardlaw A, Treichler D, et al (2012) Investigation of Cavitation as a Possible Damage Mechanism in Blast-Induced Traumatic Brain Injury. J Neurotrauma 29:1970–

1981. doi: 10.1089/neu.2011.2224

35. Hua Y, Kumar Akula P, Gu L, et al (2014) Experimental and Numerical Investigation of the Mechanism of Blast Wave Transmission Through a Surrogate Head. J Comput Nonlinear Dyn 9:31010. doi: 10.1115/1.4026156
36. Panzer MB, Bass CR, Myers BS (2010) Numerical Study on the Role of Helmet Protection in Blast Brain Injury. Pass
37. Sayed T El, Mota A, Fraternali F, Ortiz M (2008) Biomechanics of traumatic brain injury. Comput Methods Appl Mech Eng 197:4692–4701. doi: 10.1016/j.cma.2008.06.006
38. Zhu F, Mao H, Dal Cengio Leonardi A, et al (2010) Development of an FE model of the rat head subjected to air shock loading. Stapp Car Crash J 54:211–225. doi: 2010-22-0011 [pii]
39. Singh D, Cronin DS, Haladuick TN (2014) Head and brain response to blast using sagittal and transverse finite element models. Int j numer method biomed eng 30:470–489. doi: 10.1002/cnm.2612
40. Alley MD, Schimizze BR, Son SF (2011) Experimental modeling of explosive blast-related traumatic brain injuries. Neuroimage 54:S45–S54. doi: 10.1016/j.neuroimage.2010.05.030
41. Ganpule S, Cao G, Gu L, Chandra N (2009) The effect of shock wave on a human head. ASME 2009 Int Mech Eng Congr Expo 1–8. doi: 10.1115/IMECE2009-12875
42. Roberts JC, Harrigan TP, Ward EE, et al (2012) Human head-neck computational model for assessing blast injury. J Biomech 45:2899–2906. doi: 10.1016/j.jbiomech.2012.07.027
43. Panzer MB, Myers BS, Capehart BP, Bass CR (2012) Development of a finite element model for blast brain injury and the effects of CSF cavitation. Ann Biomed Eng 40:1530–1544. doi: 10.1007/s10439-012-0519-2
44. Wardlaw A, Goeller J (2010) Cavitation as a possible Traumatic Brain Injury (TBI) damage mechanism. IFMBE Proc 32 IFMBE:34–37. doi: 10.1007/978-3-642-14998-6_9
45. Subhash G, Hong Y, Canchi S, et al (2013) Cavitation Induced Structural and Neoronal

Damage in Brain Tissue : Relevance to TBI. SEM Annu Conf 1–2.

46. Subhash G, Canchi S, Hong Y, et al (2016) Damage in brain tissue due to single bubble cavitation shock. Conf Proc Soc Exp Mech Ser 6:1–5. doi: 10.1007/978-3-319-21455-9_1
47. Welker JR (2016) Explosions. http://www.chemistryexplained.com/Di-Fa/Explosions.html. Accessed 1 Jan 2015
48. Akhavan J (2004) Classification of Explosive Materials. Chem Explos 21–47. doi: 10.1039/9781847552020
49. Smith PD, Hetherington JG (1994) Blast and Ballistic Loading of Structures. CRC Press
50. Granger RA (1995) Fluid Mechanics, 1st ed. Dover Publications
51. Needham CE (2010) Blast Waves.
52. Marieb ENE, Hoehn K (2010) Human Anatomy & Physiology, 8th ed. Physiology. doi: 10.1038/nnano.2011.234
53. Edoarado (2012) Human skull scheme highlighting the cranial bones in a lateral view. In: Wikimedia. https://commons.wikimedia.org/wiki/File:Cranial_bones_en.svg. Accessed 14 Feb 2016
54. Mysid (2016) Meninges of the central nervous parts. In: Wikimedia. https://commons.wikimedia.org/wiki/File:Meninges-en.svg. Accessed 14 Feb 2016
55. McElhaney JH, Fogle JL, Melvin JW, et al (1970) Mechanical properties of cranial bone. J Biomech 3:495–511. doi: 10.1016/0021-9290(70)90059-X
56. Wood J (1971) Dynamic response of human cranial bone. J Biomech 4:1–12. doi: 10.1016/0021-9290(71)90010-8
57. Peterson J, Dechow PC (2002) Material properties of the inner and outer cortical tables of the human parietal bone. Anat Rec 268:7–15. doi: 10.1002/ar.10131
58. Singh D, Haladuick TN, Lockhart P, et al (2011) Physical Properties of Brain Tissue and Brain Simulants. Blood
59. Moore DF, Jérusalem A, Nyein M, et al (2009) Computational biology - Modeling of primary blast effects on the central nervous system. Neuroimage. doi: 10.1016/j.neuroimage.2009.02.019
60. Chafi MS, Karami G, Ziejewski M (2010) Biomechanical assessment of brain dynamic

responses due to blast pressure waves. Ann Biomed Eng 38:490–504. doi: 10.1007/s10439-009-9813-z

61. CHAFI MS, GANPULE S, GU L, CHANDRA N (2011) Dynamic Response of Brain Subjected To Blast Loadings: Influence of Frequency Ranges. Int J Appl Mech 3:803–823. doi: 10.1142/S175882511100124X
62. Mao H, Zhang L, Jiang B, et al (2013) Development of a Finite Element Human Head Model Partially Validated With Thirty Five Experimental Cases. J Biomech Eng 135:111002. doi: 10.1115/1.4025101
63. Kandel ER, Kandel ER, Schwartz JH, et al (2000) Principles of Neural Science, fourth Edition, 5th ed. McGraw-Hill Medical, New York
64. Mandal R, Guo AC, Chaudhary KK, et al (2012) Multi-platform characterization of the human cerebrospinal fluid metabolome: a comprehensive and quantitative update. Genome Med 4:38. doi: 10.1186/gm337
65. Chafi MS, Dirisala V, Karami G, Ziejewski M (2009) A finite element method parametric study of the dynamic response of the human brain with different cerebrospinal fluid constitutive properties. Proc Inst Mech Eng H 223:1003–1019. doi: 10.1243/09544119JEIM631
66. Kandel E, Schwartz J, Jessell T, et al (2012) Principles of Neural Science, 5th ed. McGraw-Hill Education / Medical
67. Conn PM (2003) Neuroscience in Medicine, 2nd ed. Humana Press
68. Conn PM (2008) Neuroscience in medicine: Third edition. Neurosci Med Third Ed. doi: 10.1007/978-1-60327-455-5
69. Altman PL, Dittmer DS (1961) Blood and other body fluids : analysis and compilation. Federation of American Societies for Experimental Biology
70. Iyengar GV, Kollmer WE, Bowen HJM (1978) The elemental composition of human tissues and body fluids: a complication of values for adults, [Rev. ed.]. Verlag Chemie, Weinheim ; New York
71. Sofronescu AG (2015) Cerebrospinal Fluid Analysis. In: Medscape. http://emedicine.medscape.com/article/2093316-overview%0A. Accessed 1 Jan 2015
72. Moore DF, Radovitzky R a, Shupenko L, et al (2008) Blast physics and central nervous

system injury. Future Neurol 3:243–250. doi: 10.2217/14796708.3.3.243

73. Saatman KE, Duhaime A-C, Bullock R, et al (2008) Classification of Traumatic Brain Injury for Targeted Therapies. J Neurotrauma 25:719–738. doi: 10.1089/neu.2008.0586
74. Ling G, Bandak F, Armonda R, et al (2009) Explosive blast neurotrauma. J Neurotrauma 26:815–825. doi: 10.1089/neu.2007.0484
75. Risdall JE, Menon DK (2011) Traumatic brain injury. Philos Trans R Soc Lond B Biol Sci 366:241–50. doi: 10.1098/rstb.2010.0230
76. Hutchinson J, Kaiser MJ, Lankarani HM (1998) The Head Injury Criterion (HIC) functional. Appl Math Comput 96:1–16. doi: 10.1016/S0096-3003(97)10106-0
77. Dionne JP, Nerenberg J, Makris A (1997) Reduction of Blast-Induced Concussive Injury Potential and Correlation With Predicted Blast Impulse. 1–16.
78. Makris a, Nerenberg J, Dionne JP, et al (2006) Reduction of blast induced head acceleration in the field of anti-personnel mine clearance. 453–464.
79. Sarntinoranont M, Lee SJ, Hong Y, et al (2012) High-Strain-Rate Brain Injury Model Using Submerged Acute Rat Brain Tissue Slices. J Neurotrauma 29:418–429. doi: 10.1089/neu.2011.1772
80. Nie X, Sanborn B, Weerasooriya T, Chen W (2013) High-rate bulk and shear responses of bovine brain tissue. Int J Impact Eng 53:56–61. doi: 10.1016/j.ijimpeng.2012.07.012
81. Sosa M a G, De Gasperi R, Paulino AJ, et al (2013) Blast overpressure induces shear-related injuries in the brain of rats exposed to a mild traumatic brain injury. Acta Neuropathol Commun 1:51. doi: 10.1186/2051-5960-1-51
82. Bo C, Balzer J, Brown K a., et al (2011) Development of a chamber to investigate high-intensity compression waves upon live cell cultures. Eur Phys J Appl Phys 55:31201. doi: 10.1051/epjap/2011110052
83. Risling M, Plantman S, Angeria M, et al (2011) Mechanisms of blast induced brain injuries, experimental studies in rats. Neuroimage 54:S89-97. doi: 10.1016/j.neuroimage.2010.05.031
84. Bolander R, Mathie B, Bir C, et al (2011) Skull flexure as a contributing factor in the mechanism of injury in the rat when exposed to a shock wave. Ann Biomed Eng 39:2550–2559. doi: 10.1007/s10439-011-0343-0

85. Heldt SA, Elberger AJ, Deng Y, et al (2014) A novel closed-head model of mild traumatic brain injury caused by primary overpressure blast to the cranium produces sustained emotional deficits in mice. Front Neurol 5 JAN:1–14. doi: 10.3389/fneur.2014.00002
86. Kamnaksh A, Budde MD, Kovesdi E, et al (2014) Diffusion tensor imaging reveals acute subcortical changes after mild blast-induced traumatic brain injury. Sci Rep 4:4809. doi: 10.1038/srep04809
87. Lee CS, Frizzell LA (1988) Exposure levels for ultrasonic cavitation in the mouse neonate. Ultrasound Med Biol 14:735–742. doi: 10.1016/0301-5629(88)90029-4
88. Hong Y, Sarntinoranont M, Subhash G, et al (2015) Localized Tissue Surrogate Deformation due to Controlled Single Bubble Cavitation. Exp Mech 97–109. doi: 10.1007/s11340-015-0024-2
89. Bass CR, Panzer MB, Rafaels KA, et al (2012) Brain injuries from blast. Ann Biomed Eng 40:185–202. doi: 10.1007/s10439-011-0424-0
90. Sundaramurthy A, Alai A, Ganpule S, et al (2012) Blast-Induced Biomechanical Loading of the Rat: An Experimental and Anatomically Accurate Computational Blast Injury Model. J Neurotrauma 29:2352–2364. doi: 10.1089/neu.2012.2413
91. Giordano C, Cloots RJH, van Dommelen JAW, Kleiven S (2014) The influence of anisotropy on brain injury prediction. J Biomech 47:1052–1059. doi: 10.1016/j.jbiomech.2013.12.036
92. Gu L, Chafi MS, Ganpule S, Chandra N (2012) The influence of heterogeneous meninges on the brain mechanics under primary blast loading. Compos Part B Eng 43:3160–3166. doi: 10.1016/j.compositesb.2012.04.014
93. Ortega JM (2011) Non-lethal blast wave interactions with a human head. Comput Fluids 52:92–103. doi: 10.1016/j.compfluid.2011.09.002
94. Zhang L (2009) Computational Modeling of Causal Mechanisms of Blast Wave Induced Traumatic Brain Injury – A Potential Tool for Injury Prevention. 1–17.
95. Singh D, Cronin DS (2015) Investigation of Cavitation Using a Modified Hopkinson Apparatus. Conf Proc Soc Exp Mech Ser 65:177–183. doi: 10.1007/978-3-319-06995-1_27

96. Shively SB, Horkayne-Szakaly I, Jones R V., et al (2016) Characterisation of interface astroglial scarring in the human brain after blast exposure: a post-mortem case series. Lancet Neurol 15:944–953. doi: 10.1016/S1474-4422(16)30057-6
97. Robertson JM, Wislicenus GF (1969) Cavitation State of Knowledge. American Society of Mechanical Engineers
98. Brennen CE (1995) Cavitation and bubble dynamics. Annu Rev Fluid Mech. doi: 10.1017/CBO9781107338760
99. Chahine KKG (2014) Advanced Experimental and Numerical Techniques for Cavitation Erosion Prediction. 106:3–35, 71–95. doi: 10.1007/978-94-017-8539-6
100. Knapp RT, Daily JW, Hammitt FG (2012) Cavitation. McGraw-Hill
101. Thiruvengadam A (1974) Handbook of Cavitation Erosion., Rev. ed. Laurel, Md. : Hydronautics
102. Kenner VH, Wieczorek DC (1980) The Response of Blood to Transient Tensile Loading. J Biomech Eng 102:151–154.
103. Kenner VH (1980) The fluid Hopkinson bar. Exp Mech 20:226–232. doi: 10.1007/BF02327705
104. Skripov VP (1974) Metastable liquids. Wiley
105. Vargaftik NB, Volkov BN, Voljak LD (1983) International Tables of the Surface Tension of Water. J Phys Chem Ref Data 12:817–820. doi: 10.1063/1.555688
106. Tucker AS, Ward CA (1975) Critical state of bubbles in liquid-gas solutions. J Appl Phys 46:4801–4808. doi: 10.1063/1.321506
107. Gibbs JW (1961) The Scientific Papers of J. Willard Gibbs. 1:237.
108. Caupin F, Herbert E (2006) Cavitation in water: a review. Comptes Rendus Phys 7:1000–1017. doi: 10.1016/j.crhy.2006.10.015
109. Williams PR, Williams RL (2004) Cavitation and the tensile strength of liquids under dynamic stressing. Mol Phys 102:2091–2102. doi: 10.1080/00268970412331292786
110. Ward JW, Montgomery LH, Clark SL (1948) A mechanism of concussion: A theory. Science (80-) 107:349–353. doi: 10.1126/science.107.2779.349
111. Overton GDN, Williams PR, Trevena DH (1984) The influence of cavitation history and entrained gas on liquid tensile strength. J Phys D Appl Phys 17:979–987. doi:

10.1088/0022-3727/17/5/012

112. Sedgewick SA, Trevena DH (1976) Limiting negative pressure of water under dynamic stressing. J Phys D Appl Phys 9:1983–1190. doi: 10.1088/0022-3727/9/14/008

113. Couzens DCF, Trevena DH (1969) Critical Tension in a Liquid under Dynamic Conditions of Stressing. Nature 222:473–474. doi: 10.1038/222473a0

114. Zang L (2015) Lecture 12 : Heterogeneous Nucleation : a surface catalyzed process. 1–5.

115. Mitropoulos AC, Stefanopoulos KL, Favvas EP, et al (2015) On the Formation of Nanobubbles in Vycor Porous Glass during the Desorption of Halogenated Hydrocarbons. Sci Rep 5:10943. doi: 10.1038/srep10943

116. Miller DL (1987) A review of the ultrasonic bioeffects of microsonation, gas-body activation, and related cavitation-like phenomena. Ultrasound Med Biol 13:443–470. doi: 10.1016/0301-5629(87)90110-4

117. Fry FJ, Sanghvi NT, Foster RS, et al (1995) Ultrasound and microbubbles: Their generation, detection and potential utilization in tissue and organ therapy-Experimental. Ultrasound Med Biol 21:1227–1237. doi: 10.1016/0301-5629(96)89519-6

118. Ginsberg HJ, Drakeiv JM, Cobbold RSC (2001) Unblocking cerebrospinal fluid shunts using low frequency ultrasonic cavitation. 1381–1384.

119. Zhang C, Huang P, Zhang Y, et al (2014) Anti-tumor efficacy of ultrasonic cavitation is potentiated by concurrent delivery of anti-angiogenic drug in colon cancer. Cancer Lett 347:105–113. doi: 10.1016/j.canlet.2014.01.022

120. Tsaklis P (2010) Presentation of Acoustic Waves Propagation and Their Effects Through Human Body Tissues. Hum Mov 11:91–95. doi: 10.2478/v10038-009-0025-z

121. Miller DL (2007) Overview of experimental studies of biological effects of medical ultrasound caused by gas body activation and inertial cavitation. Prog Biophys Mol Biol 93:314–330. doi: 10.1016/j.pbiomolbio.2006.07.027

122. Herbert E, Balibar S, Caupin F (2006) Cavitation pressure in water. Phys Rev E - Stat Nonlinear, Soft Matter Phys 74:1–22. doi: 10.1103/PhysRevE.74.041603

123. Caupin F, Balibar S, Maris HJ (2003) Limits of metastability of liquid helium. Phys B Condens Matter 329–333:356–359. doi: 10.1016/S0921-4526(02)02103-8

124. Trevena DH (1984) Cavitation and the generation of tension in liquids. J Phys D Appl Phys 17:2139–2164.
125. Temperley HN V., Trevena DH (1977) Metastability of Phase Transitions and the Tensile Strength of Liquids. Proc R Soc A Math Phys Eng Sci 357:395–402. doi: 10.1098/rspa.1977.0175
126. Temperley HN V., Treverna DH (1987) Why is the tensile strength of water measured dynamically less than that measured statically? J Phys D Appl Phys 20:1080–1081.
127. Plesset milton s. (1970) Effect of dissolved of gases on cavitation in liquids.
128. Chesterman WD (1952) The Dynamics of Small Transient Cavities. Proc Phys Soc 65:846–858. doi: 10.1088/0370-1301/65/11/302
129. Hansson I, Kedrinskii V, Morch KA (1982) On the dynamics of cavity clusters. J Phys D Appl Phys 15:1725–1734. doi: 10.1088/0022-3727/15/9/017
130. Williams PR, Williams PM (1996) Pressure – tension cycles induced by dynamic stressing and cavitation in liquids. J Phys D Appl Phys 29:1904–1909. doi: 10.1088/0022-3727/29/7/026
131. Williams PR, Williams PM, Brown SWJ (1997) Pressure waves arising from the oscillation of cavitation bubbles under dynamic stressing. J Phys D Appl Phys 30:1197–1206. doi: 10.1088/0022-3727/30/8/007
132. Williams PR, Williams PM, Brown SWJ (1998) An instrument for studying cavitation phenomena in liquids subjected to tension generated and by free-surface reflection of ab initio compressional waves. Meas Sci Technol 9:976–982. doi: 10.1088/0957-0233/9/6/015
133. Williams PR, Williams PM, Brown SW (1998) Cavitation phenomena in water involving the reflection of ultrasound pulses from a free surface, or from flexible membranes. Phys Med Biol 43:3101–3111. doi: 10.1088/0031-9155/43/10/028
134. Williams PR, Williams PM, Brown SWJ, Temperley HN V. (1999) On the tensile strength of water under pulsed dynamic stressing. Proc R Soc A Math Phys Eng Sci 455:3311–3323. doi: 10.1098/rspa.1999.0452
135. Couzens DCF, Trevena DH (1974) Tensile failure of liquids under dynamic stressing. J Phys D Appl Phys 7:2277–2287. doi: 10.1088/0022-3727/7/16/315

136. Bull TH (1956) The tensile strengths of viscous liquids under dynamic loading This. Br J Appl Phys 7:416–418.
137. Sedgewick SA, Trevena DH (1978) Breaking tensions of dilute polyacrylamide solutions. J Phys D Appl Phys 11:2517–2526.
138. Overton GDN, Trevena DH (1981) Cavitation phenomena and the occurrence of pressure- tension cycles under dynamic stressing. J Phys D Appl Phys 14:241–250. doi: 10.1088/0022-3727/14/2/016
139. Overton GDN, Treverna DH (1982) Some factors which influence the observed dynamic breaking tensions of a liquid. J Phys D Appl Phys 15:3–6. doi: 10.1088/0022-3727/15/2/001
140. Williams PR, Williams RL (2000) On anomalously low values of the tensile strength of water. Proc R Soc London A Math Phys Eng Sci 456:1321–1332. doi: 10.1098/rspa.2000.0564
141. Williams PR, Williams RL (2002) Cavitation of liquids under dynamic stressing by pulses of tension. J Phys D Appl Phys 35:2222–2230.
142. Kenner VH (1978) The propagation of compressive and tensile waves in a fluid column. Int J Mech Sci 20:373–383.
143. Chen WW, Song B (2013) Split Hopkinson (Kolsky) Bar: Design, Testing and Applications. Springer New York Dordr Heidelb London. doi: 10.1007/978-1-4419-7982-7
144. Pervin F, Chen WW (2009) Dynamic mechanical response of bovine gray matter and white matter brain tissues under compression. J Biomech 42:731–735. doi: 10.1016/j.jbiomech.2009.01.023
145. Trexler MM, Lennon AM, Wickwire AC, et al (2011) Verification and implementation of a modified split Hopkinson pressure bar technique for characterizing biological tissue and soft biosimulant materials under dynamic shear loading. J Mech Behav Biomed Mater 4:1920–1928. doi: 10.1016/j.jmbbm.2011.06.008
146. Lim AS, Lopatnikov SL, Gillespie JW (2009) Development of the split-Hopkinson pressure bar technique for viscous fluid characterization. Polym Test 28:891–900. doi: 10.1016/j.polymertesting.2009.08.002

147. Frew DJ (2005) Pulse Shaping Techniques for Testing Elastic-plastic Materials with a Split Hopkinson Pressure Bar. Exp Mech 45:186–195. doi: 10.1177/0014485105052111
148. Chen X, Ge L, Zhou J, Wu S (2016) Experimental Study on Split Hopkinson Pressure Bar Pulse-Shaping Techniques for Concrete. J Mater Civ Eng 28:4015196. doi: 10.1061/(ASCE)MT.1943-5533.0001494
149. Kolsky H (1949) An Investigation of the mechanical properties of materials at very high rates of Loading. Proc Phys Soc B 62:676–700.
150. Gray GI, Blumenthal W (2000) Split Hopkinson pressure bar testing of soft materials. ASM Handb Mech Test Eval 8:488–496.
151. Meyers MA (1994) Dynamic Behavior of Materials. doi: 10.1002/9780470172278
152. Davies RM (1947) A critical study of the hopkinson pressure bar. Eng. Labratory 240:
153. Chapra SC, Canale RP (2015) Numerical methods for engineers. Math Comput Simul 33:260. doi: 10.1016/0378-4754(91)90127-O
154. Doyle JF (1989) Methodology, Wave Propagation in Structures: An FFT-Based Spectral Analysis. Springer-Verlag New York, West Lafayette
155. Salisbury C (2001) Spectral Analysis of Wave Propagation Through a Polymeric Hopkinson Bar. University of Waterloo
156. Van Sligtenhorst C, Cronin DS, Wayne Brodland G (2006) High strain rate compressive properties of bovine muscle tissue determined using a split Hopkinson bar apparatus. J Biomech 39:1852–1858. doi: 10.1016/j.jbiomech.2005.05.015
157. Sligtenhorst C Van, Cronin DS, Brodland GW (2004) Supplement to: HIGH STRAIN RATE COMPRESSIVE PROPERTIES OF BOVINE MUSCLE TISSUE FOUND USING A SPLIT HOPKINSON BAR APPARATUS. 1–13.
158. Salisbury C, Cronin D, Lien F-S (2015) Deformation Mechanics of a Non-Linear Hyper-Viscoelastic Porous Material, Part II: Porous Material Micro-Scale Model. J Dyn Behav Mater 1:249–258. doi: 10.1007/s40870-015-0027-1
159. Salisbury C, Cronin D, Lien F-S (2015) Deformation Mechanics of a Non-linear Hyper-viscoelastic Porous Material, Part I: Testing and Constitutive Modeling of Non-porous Polychloroprene. J Dyn Behav Mater 1:237–248. doi: 10.1007/s40870-015-0026-2

160. Acromag Incorporated (2001) Introduction to strain & strain measurement. Wixom
161. Kaiser M a, Dr. Alfred Wicks, Leonard Wilson, Dr. William Saunders (1998) Advancements in the Split Hopkinson Bar Test.
162. Brown D (2017) AutoTracker. http://physlets.org/tracker/. Accessed 15 Jul 2016
163. Strand OT, Berzins L V, Goosman DR, et al (2004) Velocitimetry using heterodyne techniques. SPIE Proc 5580:593–599. doi: 10.1117/12.567579
164. Strand OT, Goosman DR, Martinez C, et al (2005) A Novel System for High- Speed Velocimetry Using Heterodyne Techniques.
165. Thunert C (2012) CORA Release 3.6 User 's Manual.
166. Gehre C, Gades H, Wernicke P (2009) OBJECTIVE RATING OF SIGNALS USING TEST AND SIMULATION RESPONSES Christian Gehre. Enhanc Saf Veh. doi: 09-0407
167. (1999) ISO/TR 9790: Road Vehicles – Anthropomorphic side impact dummy – lateral impact response requirements to assess the biofidelity of the dummy. Geneva
168. Sasso M, Antonelli MG, Mancini E, et al (2016) Experimental and numerical analysis of pressure waves propagation in a viscoelastic Hopkinson Bar. 6–13.
169. Song B, Nishida E, Corona E, Laboratories SN (2015) Data-Reduction Uncertainties in Kolsky Bar Experiments on Metals. SEM
170. Prabhu R, Horstemeyer MF, Tucker MT, et al (2011) Coupled experiment/finite element analysis on the mechanical response of porcine brain under high strain rates. J Mech Behav Biomed Mater 4:1067–1080. doi: 10.1016/j.jmbbm.2011.03.015
171. Roache PJ (1994) Perspective: A Method for Uniform Reporting of Grid Refinement Studies. J Fluids Eng 116:405–413. doi: 10.1115/1.2910291
172. Özkaya N, Nordin M, Goldsheyder D, Leger D (2012) Fundamentals of Biomechanics, 3rd ed. doi: 10.1007/978-1-4614-1150-5
173. Singh D (2015) Investigation of Primary Blast Injury and Protection using Sagittal and Transverse Finite Element Head Models. University of Waterloo
174. D'Onofrio A (2016) Biology-Textbook. http://www.alyvea.com/biology-textbook/. Accessed 1 Feb 2016
175. Bustamante M, Singh D, Cronin DS (2016) Modified hopkinson apparatus to investigate

fluid cavitation as a potential source of injury. Conf Proc Soc Exp Mech Ser 85:43–51. doi: 10.1007/978-3-319-22452-7_8

176. Hong Y, Canchi S, King M, et al (2014) Development of a test system to study brain tissue damage due to cavitation. p 2
177. Visible Human Project. U.S. National Library of Medicine, NIH
178. Ebraheim NA, Lu J, Biyani A, et al (1996) An Anatomic Study of the Thickness of the Occipital Bone. Spine (Phila Pa 1976) 21:1725–1729. doi: 10.1097/00007632-199608010-00002
179. Zarghooni K, Boese CK, Siewe J, et al (2016) Occipital bone thickness: Implications on occipital-cervical fusion. A cadaveric study. Acta Orthop Traumatol Turc 50:606–609. doi: 10.1016/j.aott.2016.04.003
180. AZoM (2012) AISI 1010 Carbon Steel. http://www.azom.com/article.aspx?ArticleID=6539. Accessed 20 Jun 2006
181. Collins JA, Busby HR, Staab GH (2009) Mechanical Design of Machine Elements and Machines: A Failure Prevention Perspective, 2nd ed. Wiley
182. LSDYNA (2013) LS-DYNA Keyword User's Manual Volume II: Material Models.
183. Stander N, Roux W, Basudhar A, et al (2015) LS-OPT ® User's Manual - A Design Optimization and Probabilistic Analysis Tool for the engineering analyst.
184. Zhao H, Gary G, Klepaczko JR (1997) On the use of a viscoelastic split hopkinson pressure bar. Int J Impact Eng 19:319–330. doi: 10.1016/S0734-743X(96)00038-3
185. Harvey EN, McElroy WD, Whiteley AH (1947) On cavity formation in water. J Appl Phys 18:162–172. doi: 10.1063/1.1697598
186. (2014) Procedure to construct injury risk curves for the evaluation of road user protection in crash tests (ISO/TS 18506).

APPENDIX A: PDV MatLab Processing Code

```
%(MatLab R2015a, MathWorks)
%Made in-house at University of Waterloo
% By: Jose Imbert
%Test for finding and storing max P for each frequency
%Uses pdv data for long rod hit by a hammer

wavelength = 1550E–9; %wavelength of laser
namename='C1et100050';
xlsx='.xlsx';
dat='.dat';
filename=strcat(namename,xlsx);
imp_data=strcat(namename,dat);
%load PDV data
data = importdata (imp_data);
time = data(:,1);
v = data(:,2);


window = 256; %number of samples in window (window width.
overlap = window/2; %window overlap one half
bins = 1024; %number of frequency bins
samp_freq = 25.0E6;  %sampling rate per second

%v_min=0.062; %min velocity used to cut off lower freqs in m/s
v_min=0.2; %min velocity used to cut off lower freqs in m/s
v_max=samp_freq*(0.5)*(0.5)*wavelength; %velocity used to cut off greater freqs in m/s

%for cleaning v data
outlier_filter=1.01;

%produce and plot spectrogram and P matrix
[S,F,T,P]=spectrogram(v,window,overlap,bins,samp_freq,'yaxis');
spectrogram(v,window,overlap,bins,samp_freq,'yaxis');
                        %displays spectrogram
                        %'yaxis' specifies freq in y axis
%time from spectrogram. Used with current_time_plot for plotting
T_tran = transpose (T);

t_len=length(T);
f_len=length(F);
%display(t_len)
max_freqs = zeros(length(T),1);%creates max_freqs vector of length l and sets it to zero
%Get maximum frequs from P matrix
%Need to eliminate first two bins since zero freq has greatest magnitude
%Get indices for max of full P for comparisson with Pshort
f_per_row = (samp_freq*0.5)/f_len;
f_v_min = v_min/(wavelength*0.5);
f_v_max = v_max/(wavelength*0.5);
low_row =  int16(f_v_min/f_per_row);
%high_row =4.5e8;
high_row =int16((f_v_max/f_per_row));
%get max frequencies from P for velocity calculation, between low_row and
%high row
[c,i]= max(P(low_row:high_row,1:t_len),[],1);
%make a vector with the max freqs using the indexes from the P matrix max
%values
```

```
for u=1:(t_len)
  max_freqs(u,1) = F((i(1,u)+low_row),1);
end;

%make indices column for plotting
for u=1:t_len
   indices (u,1)=u;
end
%calculate velocity from max freqs ans make vel vector. Only good with PDV
%data
velocity = zeros(t_len,1);
% first half of data points zeroed

%for m=int16(t_len/2):t_len
for m=1:t_len
   velocity (m,1)= wavelength*0.5*max_freqs(m,1);
end;

%*********************************************************************
%Export to excel
%*********************************************************************

exp_v_= table(T_tran,velocity);
%file name at begining
writetable(exp_v_,filename,'Sheet',1,'Range','A1');
plot(velocity);
```

APPENDIX B: CORA Global Parameters

```
###############################################################################
#
#   CORA v3.0.0
#
###############################################################################
#
###############################################################################
#
#   Global Parameters
#
###############################################################################
BEGIN GLOBAL_PARAMETERS
  DES_MOD           CSHB VALIDATION with PSHPB Free–end CORA            ; Header of the evaluation
  DES_GLO           3 striker cases (short, long, sphere). Checks the rating of CSHB.exe to experimental data. (1) Attenuated
Reflected Wave to Incident Wave. (2) Compares CSHB EndVel output to PDV EndVel output  ; Sub–header of the evaluation
#
# Global settings to define the interval of evaluation
  A_THRES           0.000               ; Threshold to set the start of the interval of evaluation [0,...,1]
  B_THRES           0.000               ; Threshold to set the end of the interval of evaluation [0,...,1]
  A_EVAL            0.000               ; Extension of the interval of evaluation [0,...,1]
  B_DELTA_END       0.000               ; Additional parameter to shorten the interval of evaluation (width of the corridor:
A_DELTA_END*Y_NORM) 0 = disabled
  T_MIN/T_MAX       1.7 automatic               ; Manually defined start (time) and end (time) of the interval of evaluation
(automatic = calculated for each channel)
  T_UNIT                        ms
#
# Global settings of the corridor method
  K                 1                   ; Transition between ratings of 1 and 0 of the corridor method [–] (1 = linear, 2 = quadratic ...)
  G_1               0.00                ; Weighting factor of the corridor method [–]
  a_0/b_0           0.00    0.00        ; Width of the inner and outer corridor [–]
  a_sigma/b_sigma   0       0           ; Multiples of the standard deviation to widen the inner and outer corridor [–]
# Global settings of the cross–correlation method
  D_MIN             0.01                ; delta_min as share of the interval of evaluation [0,...,1]
  D_MAX             0.10                ; delta_max as share of the interval of evaluation [0,...,1]
  INT_MIN           .95                 ; Minimum overlap of the interval [0,...,1] (MB– changed to remove Warnings)
  K_V               1                   ; Transition between ratings of 1 and 0 of the progression rating [–] (1 = linear, 2 = quadratic
...)
  K_G               1                   ; Transition between ratings of 1 and 0 of the size rating [–] (1 = linear, 2 = quadratic ...)
  K_P               1                   ; Transition between ratings of 1 and 0 of the phase shift rating [–] (1 = linear, 2 = quadratic ...)
  G_V               0.33                ; Weighting factors of the progression rating [–]
  G_G               0.33                ; Weighting factors of the size rating [–]
  G_P               0.33                ; Weighting factors of the phase shift rating [–]
  G_2               1.0                 ; Weighting factors of the cross–correlation method [–]
# Normalisation of the weighting factors
  WF_NORM           YES                 ; Normalisation of the weighting factors [YES/NO]?
# Signal settings
  ISONAME_1–2/11–12    YES              ; Consideration of the position 1/2 (test object, seating position) and 11/12 (fine
location 3 – dummy) of the ISO code [YES/NO]
  MIN_NORM          0.00                ; Threshold (as fraction of the global absolute maximum amplitude) to start special
treatment of secondary axis [0,...,1]
  Y_NORM            value               ; Type of calculation of Y_NORM (extremum or value)
#
# Format settings of the html report
  OUTPUT_FORMAT     LSPOST              ; Export format (LSPOST, PAMVIEW or Hypergraph)
#OUTPUT_UNIT        mm–kg–ms            ; Unit system
#OUTPUT_g           NO                  ; Use [g] [YES/NO]?
```

```
# Layout of the html report
  FONT_SMALL          12              ; Size of the small font
  FONT_LARGE          14              ; Size of the large font
  PreT_LC/PostT_LC    –1  –1            ; Expansion of the plotted interval of the curves (–1: complete curve)
END GLOBAL_PARAMETERS
#
```

APPENDIX C: Incident Bar Repeatability/Benchmark Tests

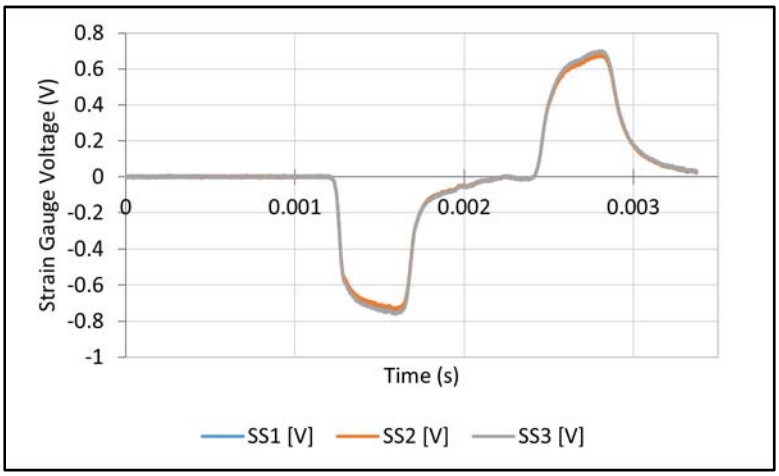

Figure 89. Strain gauge voltage output of the short striker at 97 kPa firing–pressure (3 repeats)

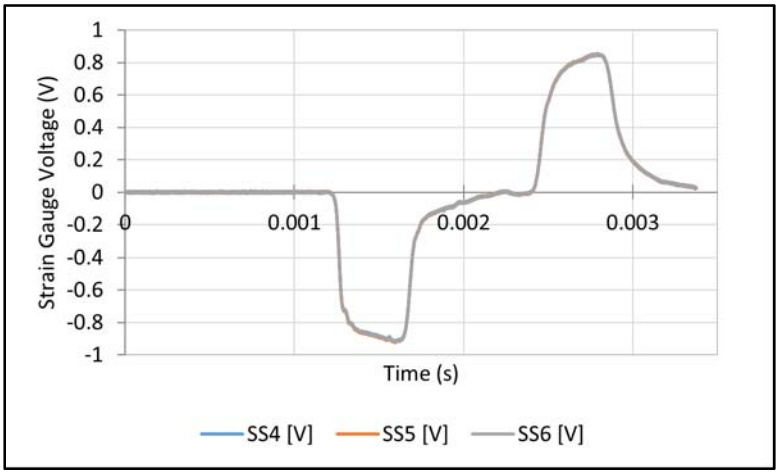

Figure 90. Strain gauge voltage output of the short striker at 124 kPa firing–pressure (3 repeats)

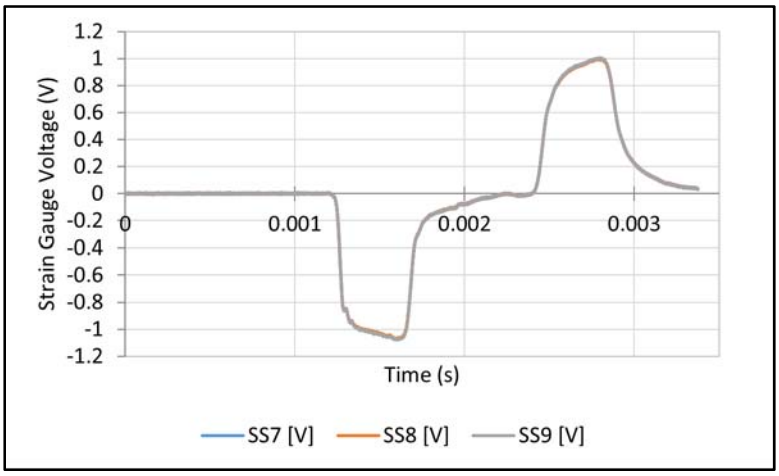

Figure 91. Strain gauge voltage output of the short striker at 152 kPa firing–pressure (3 repeats)

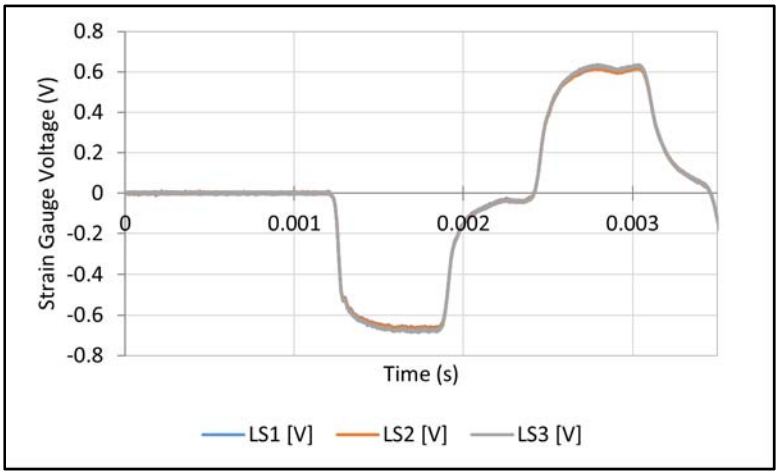

Figure 92. Strain gauge voltage output of the long striker at 97 kPa firing–pressure (3 repeats)

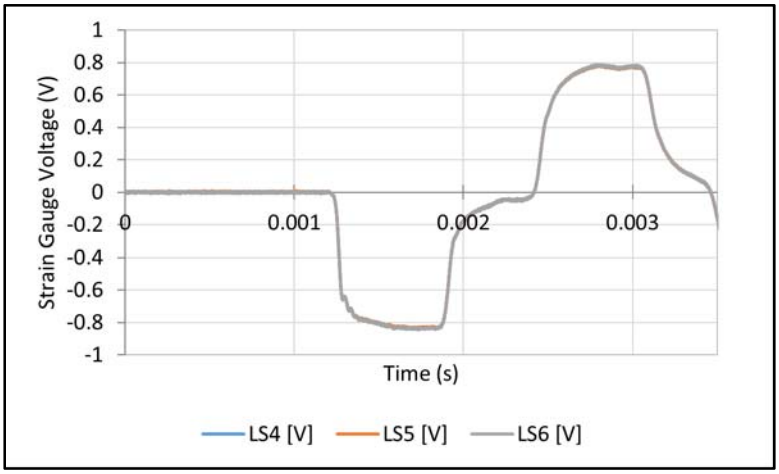

Figure 93. Strain gauge voltage output of the long striker at 124 kPa firing–pressure (3 repeats)

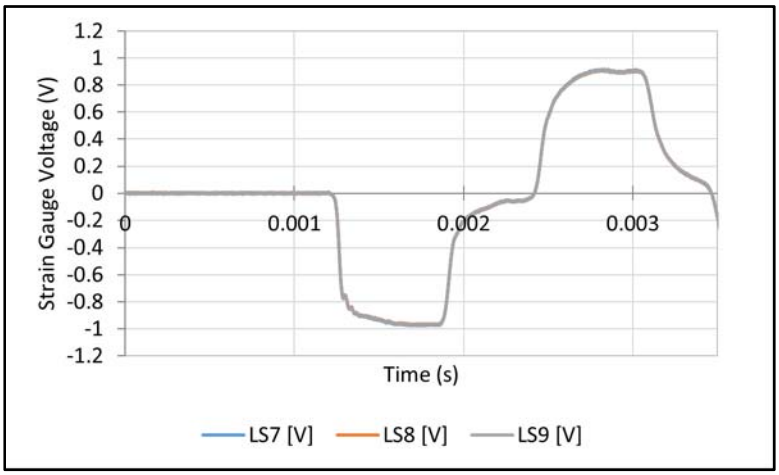

Figure 94. Strain gauge voltage output of the long striker at 152 kPa firing–pressure (3 repeats)

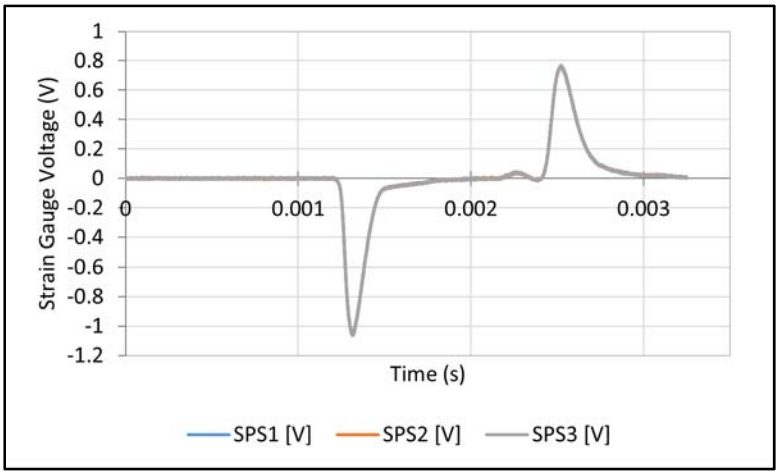

Figure 95. Strain gauge voltage output of the sphere striker at 97 kPa firing–pressure (3 repeats)

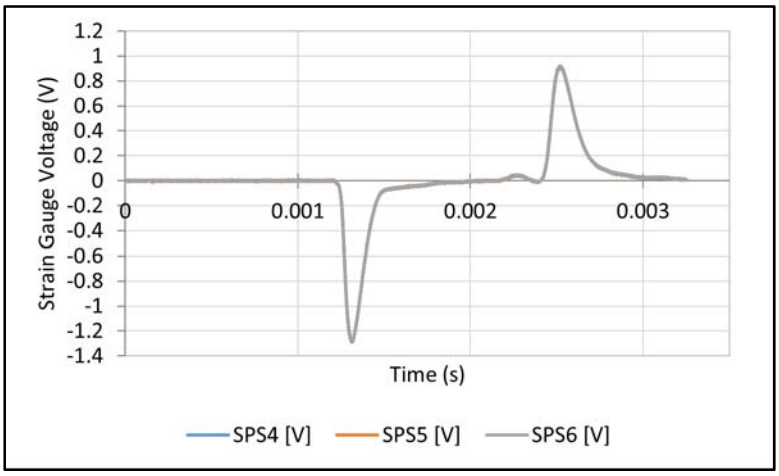

Figure 96. Strain gauge voltage output of the sphere striker at 124 kPa firing–pressure (3 repeats)

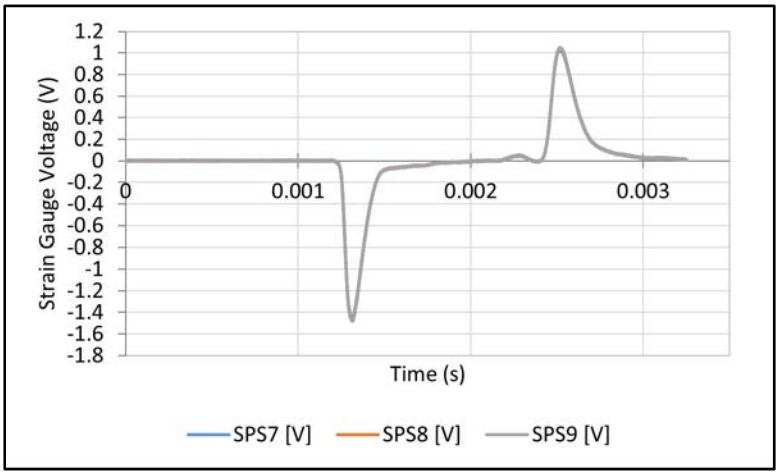

Figure 97. Strain gauge voltage output of the sphere striker at 152 kPa firing–pressure (3 repeats)

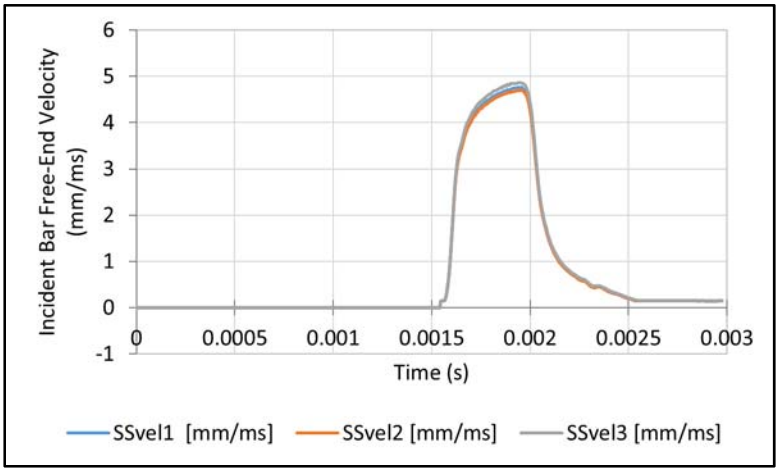

Figure 98. Incident bar free–end velocity of the short striker at 97 kPa firing–pressure (3 repeats)

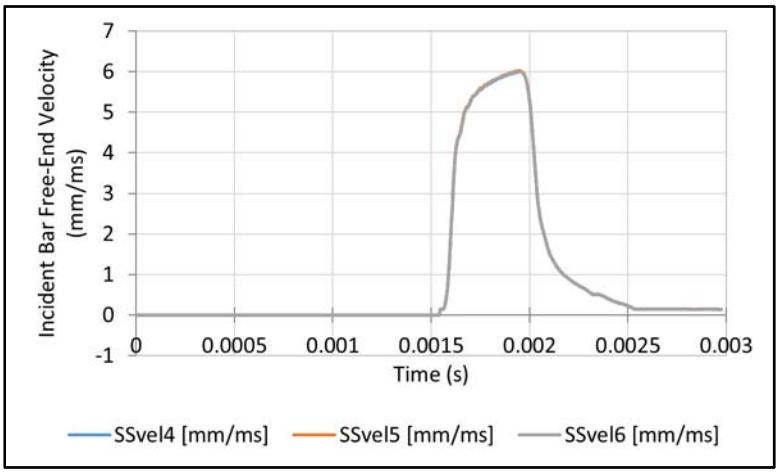

Figure 99. Incident bar free–end velocity of the short striker at 124 kPa firing–pressure (3 repeats)

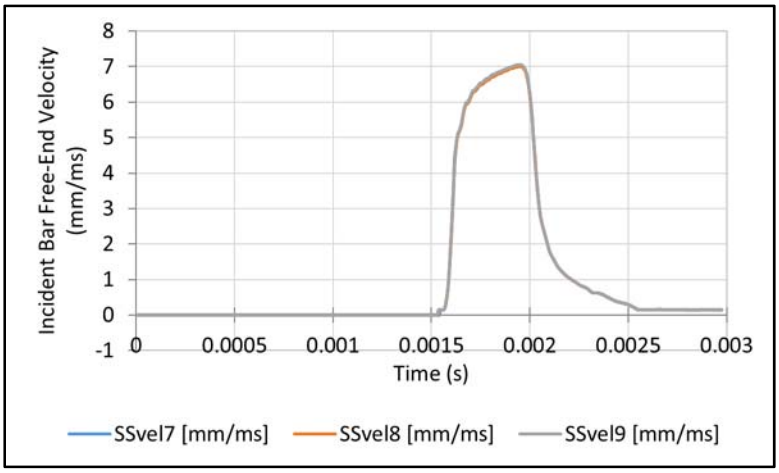

Figure 100. Incident bar free–end velocity of the short striker at 152 kPa firing–pressure (3 repeats)

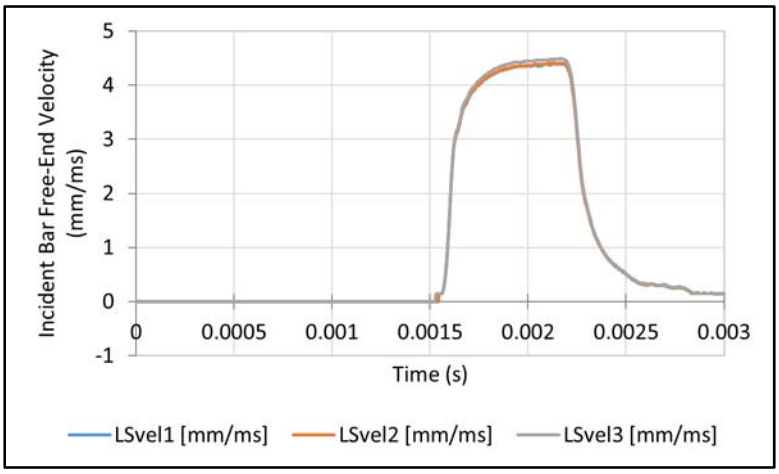

Figure 101. Incident bar free–end velocity of the long striker at 97 kPa firing–pressure (3 repeats)

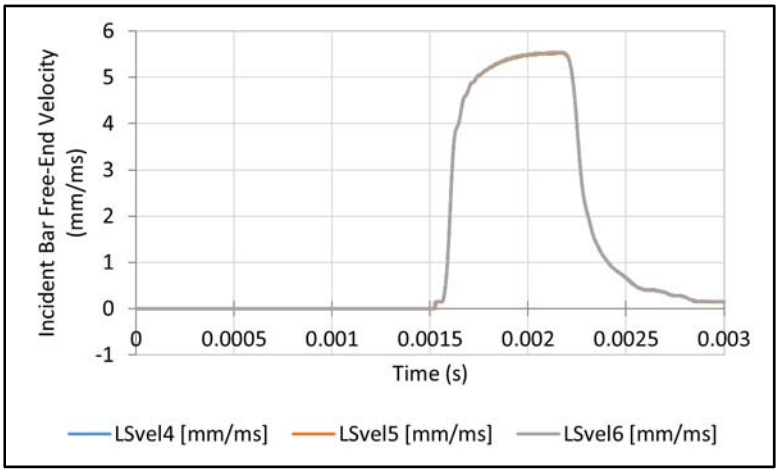

Figure 102. Incident bar free–end velocity of the long striker at 124 kPa firing–pressure (3 repeats)

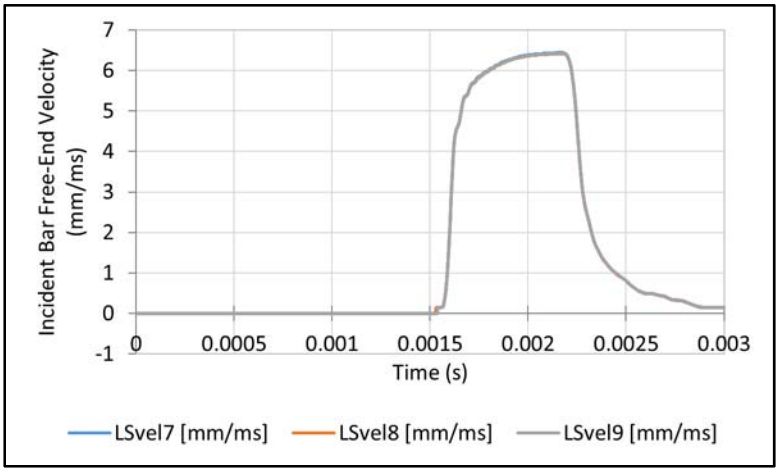

Figure 103. Incident bar free–end velocity of the long striker at 152 kPa firing–pressure (3 repeats)

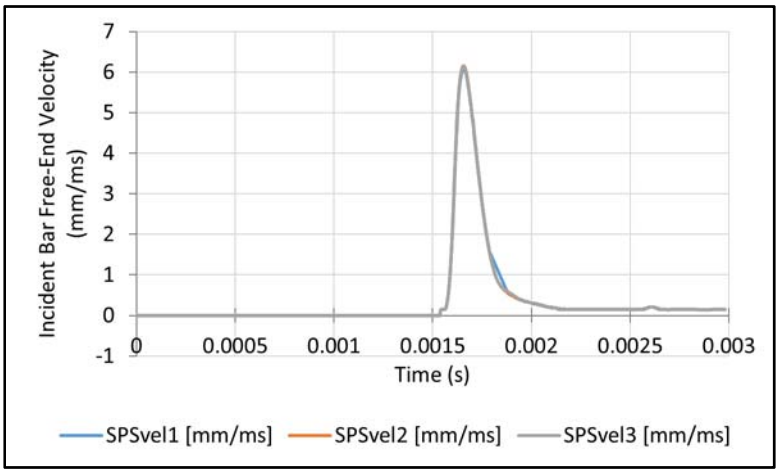

Figure 104. Incident bar free–end velocity of the sphere striker at 97 kPa firing–pressure (3 repeats)

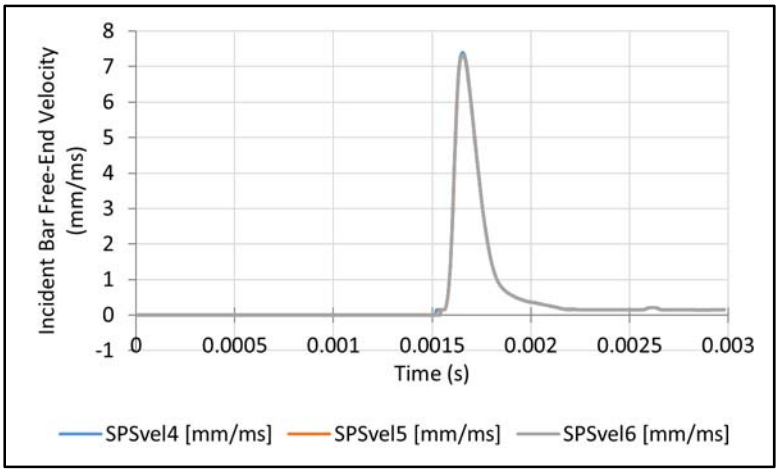

Figure 105. Incident bar free–end velocity of the sphere striker at 124 kPa firing–pressure (3 repeats)

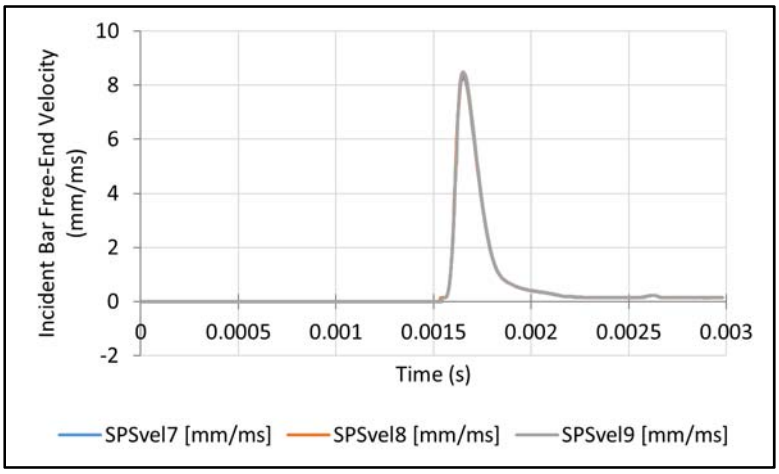

Figure 106. Incident bar free–end velocity of the sphere striker at 152 kPa firing–pressure (3 repeats)